POLITECNICO DI TORINO

Corso di Laurea Magistrale
in Communications and Computer Networks Engineering

Tesi di Laurea Magistrale

Study and Design of GNSS-based Positioning Units Integrating Collaborative Virtual Ranging

Relatore
prof. Fabio Dovis

Andrea Nardin
matricola: 233342

Anno accademico 2017 – 2018

Summary

Global Navigation Satellite Systems (e.g. GPS, GALILEO, GLONASS, BeiDou) provide effective location information to terrestrial users equipped by a receiver. Global Navigation Satellite Systems (GNSS) can support unlimited users since the receivers operates passively, exploiting radionavigation principles. In such a context the position and velocity of a user are determined from the estimation of parameters of a radiofrequency (RF) signal transmitted by a satellite. If Line-of-Sight (LOS) propagation is verified, these are effectively converted to estimated distances from the transmitters (namely pseudorange measurements), to estimate the user position. In order to improve the positioning performance, GNSS measurements are, nowadays, integrated with a variety of additional non-GNSS sensors. Inertial Navigation Systems, Passive Ranging Sensors, and camera-based visual systems are going to characterize the market of high-end vehicles and portable devices to provide high-performance positioning and navigation capabilities.

This thesis investigated an alternative approach based on a cooperative paradigm according to which users share navigation data and cognitive sensing of the surrounding environment. According to this paradigm as a cost-effective alternative to the aforementioned sensors, auxiliary navigation information can be exchanged as external aids to support individual localization.

In this work, GNSS-users that experience reduced sky visibility conditions are supported by members of a swarm of collaborating agents to improve their location and navigation capabilities. The proposed solution guarantees an improved continuity of localization in condition of poor sky visibility or bad satellites geometry.

These GNSS positioning units exploit an auxiliary, cooperative, range, namely the *Inter-Agent Range* (IAR) that is retrieved from a geometrical calculation once a proper amount of collaborative information is exchanged among networked agents. The quantity provided by the IAR method is an estimation of the baseline $\hat{l}^s_{AB}$ between two collaborating agents (contextually an *aided* and an *aiding* agent), as illustrated in Figure 1a. The estimation of the IAR and the successive integration in the positioning algorithm have been the main targets of this analysis, carried out either focusing on a pair of collaborating agents or by a network perspective.

The IAR estimation procedure has been deeply discussed, inspecting impact factors and estimation issues in a dynamic context, with particular attention to communication delays. The adaptation of the IAR paradigm to a dynamic and network constrained context, heavily affects the basic geometry of the IAR retrieval process, resulting in a time-dependent configuration, summarized in Figure 1b.

It has been shown that a critical point is related to the variables associated to the

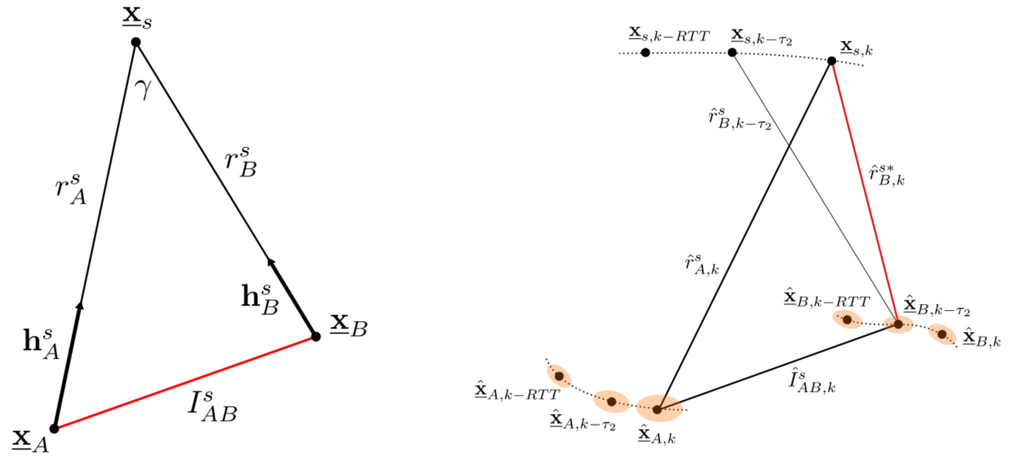

(a) Static scenario (b) Dynamic scenario

Figure 1: IAR computation in static and dynamic frameworks. A is the aided agent, B is the aiding agent and s is a shared satellite.

aided agent, which need to be estimated in a condition of lack of sufficient data. To this purpose two predictive stages has been developed along with correspondent estimation algorithms. After the definition of suitable algorithms, the IAR estimation process has been taken apart in an extensive analysis, where all the impact factors have been isolated and investigated. From the analysis it has been verified that the sole injection of noise in the system is not responsible for instability in the cooperative positioning algorithm. Divergence arises instead with the concurrent presence of feedback between position output and IAR estimation, which is unavoidable in the IAR extrapolation scheme and becomes particularly relevant after long time-span of poor GNSS visibility. However, it has been shown that, even during severe reduction of the GNSS visibility, IAR measurements keep a Gaussian-like distribution, justifying the implementation in an Extended Kalman Filter (EKF) for positioning.

A measurement model for a GNSS/IAR tightly-coupled integration in the EKF has been designed in order to preserve the optimality of the EKF-based positioning algorithm when cooperative data are involved in the solution. The stability issues relative to the choice of the linearization point has been presented as well as the possibility of a Least-Mean Square re-initialization of the EKF, possible thanks to the IAR integration, and useful to mitigate divergent phenomena.

The effectiveness of the solution adopted for the IAR/GNSS tight integration in the positioning algorithm has been investigated by means of a Monte Carlo simulation. The key aspects of this IAR implementation in a multi-agent environment have been discussed and simulation results have been reported. The simulation environment has been exploited to test the limits and performance of the IAR integration model and to retrieve a statistical characterization of positioning outcomes and IAR estimates thanks to the high number of realizations of the experiments.

In this context several scenarios have been analyzed, investigating different motion dynamics of the receivers, either constrained (urban environment) or random, and different environmental conditions (such as sky visibility and measurement noise) and network constraints (i.e. communication delays). A technique to preserve confidentiality in the network has also been tested and consistent improvements have been observed thanks to numerical errors reduction.

Through experimental results, it has been shown that the proper modeling of system dynamics and measurements integration in the EKF is of primary importance in the context of the IAR paradigm, due to the widespread effects that non-modeled effects have in the hybrid positioning routine. In particular a specific measurement model is fundamental to accomplish an efficient integration of the additional cooperative measurements. To this purpose, some parameters of this model have been configured after an empirical optimization procedure. It has to be remarked that the optimization criteria have been based on aggregated network metrics, hence optimized parameters have general validity and can be adopted in the IAR algorithm.

The importance of a fine IAR measurement model is proportional to the number of additional ranges integrated. Therefore, contextually to a model refinement, a wise selection policy has been imposed on the collaborative range contributions retrieved from the swarm of cooperating agents. Selective strategies and aggregation policies have been therefore widely tested. From these results it has been confirmed that the reduction of IAR contributions mitigates the effects of model sub-optimality, but a valuable selective criterion is necessary to target a significant improvement of the positioning performance.

Despite of the challenging tuning of the proposed navigation algorithm, good benefits have been obtained from this collaborative positioning solution that led to an improved GNSS/IAR tight integration in the positioning algorithm. The enhanced algorithm has been eventually tested and compared to an EKF-based non-cooperative PVT solution: the robustness of the IAR method to GNSS visibility limitations has been verified. Despite the limited sky visibility, the IAR method is able to limit the performance deterioration caused by the lack of positioning data (measurements), proving the effectiveness of the information enhancement carried by the inter-agent range.

A valuable measurement model of the inter-agent range has been proved as an essential feature for the IAR integration algorithm to ultimately obtain a reliable position estimation. With this in mind, a further research could be oriented to a finer definition of the GNSS/IAR observation matrix and the measurement covariance matrix. In particular, an adaptive real-time optimization on the measurement covariance matrix or the derivation of closed form equations for IAR covariances that overcome the use of upper bounds, would lead to a measurement covariance matrix that will better describe the IAR measurement from a statistical point of view, significantly reducing the EKF sub-optimality.

The interest in extending this cooperation paradigm to groups of commercial, low-grade GNSS receivers, is nowadays promising especially for urban environment where GNSS satellites visibility is limited, as well as the possibility of having users in LOS. In terms of applications this solution would be of particular interest in the field of Intelligent Transport Systems (ITS), considering the presence of GNSS receivers in any GNSS-Based Positioning Terminals (GBPT). Indeed, the density of GNSS-enabled mobile devices is becoming increasingly significant in crowded locations, making widespread GNSS receivers a sensor network for new positioning and navigation paradigms.

Acknowledgements

I would like to thank Alex Minetto for his enthusiastic help, always precious and often beyond his duties. A special thank goes to my girlfriend Martina for joining me with the same passion in pursuing this objective.

Contents

List of Tables

List of Figures

Le courage!
[Corsican proverb]

Chapter 1

Introduction

In the last decades, innovation in positioning and navigation technologies has been fostered by integrating Global Navigation Satellite System (GNSS) with a variety of additional non-GNSS sensors. Inertial Navigation System (INS), Passive Ranging Sensor (PRS), and camera-based visual systems are going to characterize the market of high-end vehicles and portable devices to provide high-performance positioning and navigation capabilities [1].

In the past years, researchers have investigated cooperative navigation among multi-agent systems to improve the performance of respective individual localization by sharing navigation data and cognitive sensing of the surrounding environment [2]. According to this paradigm as a cost-effective alternative to the aforementioned sensors, auxiliary navigation information can be exchanged as external aids to support individual localization. Such information are typically retrieved by PRS in the form of relative ranges among agents in Line-of-Sight (LOS) [3],[4],[5].

The interest in extending this cooperation paradigm to groups of commercial, low-grade GNSS receivers, is nowadays promising especially for urban environment where GNSS satellites visibility is limited, as well as the possibility of having users in LOS. In terms of applications this solution would be of particular interest in the field of ITS [6], considering the presence of GNSS sensors in any GNSS-Based Positioning Terminals (GBPT). Indeed, the density of GNSS-enabled mobile devices is becoming increasingly significant in crowded locations, making widespread GNSS receivers a sensor network for new positioning and navigation paradigms.

GNSS-based Positioning, Time and Velocity (PVT) solutions rely on the quality of code or phase measurements performed by the receiver [7]. These quantities are independently retrieved by each GNSS receivers w.r.t. the known position of the satellites. Relying on such data, additional relative measurements can be cooperatively computed by exploiting simultaneous visibility of a set of common satellites and respective pseudorange measurements [8][9][10]. Such ranging techniques overcome the limitations of LOS required by PRS at the cost of a supporting telecommunication infrastructure (e.g. Direct Short Range Communication, Vehicular Ad-hoc Network, C-V2X, cellular network). As an alternative approach, this work presents the integration of the Inter Agent Range (IAR) technique proposed in [11] to improve positioning performances as well as continuity of PVT solutions in GNSS-partially-denied conditions.

IAR measurements are obtained through an aided computation between pairs of moving agents whenever a receiver experiences a reduced visibility of the sky and related poor positioning performance. The aiding can be offered by any available member of the network which is able to locate itself with pre-established precision and accuracy. The proposed ranging technique relies on basic geometrical properties and it has been shown that it guarantees better average performance than absolute position difference [12]. Navigation data required for such a collaborative computation are assumed being transmitted over low latency communication within a multi-agent network, that also exploits virtual positioning to preserve confidentiality.

This dissertation is dedicated to the study and the design of GNSS-based positioning units which integrate this cooperative ranging solution (the IAR). By analysing the parameters involved in IAR computation, this work investigates the feasibility and reliability of a tight integration of GNSS and GNSS-collaboratively-derived measurements within a network of moving asynchronous receivers. More in detail, a set of agents in the network that experiences long time spans of partially-denied GNSS visibility is considered, observing the behavior of the collaborative measurement and the estimated trajectory along the time. With respect to previous works [11] [13] [12], timing and communication delays have been introduced and the relative issues have been faced in the definition of new collaborative algorithms for cooperative range estimation.

In correspondence of a GNSS-partially-denied period, the positioning solution of the agent is not sufficiently precise to estimate reliable steering vectors, necessary for the IAR computation. Two predictive stages are hence introduced along with the overall navigation algorithm to forecast such quantities. Multiple Kalman Filters (i.e. Kalman Filter and Extended Kalman Filter) are combined to effectively pursue the GNSS/IAR tight integration. Then, IAR collaborative measurements are tightly-integrated with code measurements pseudoranges in the structure of an EKF-based algorithm for positioning and navigation. IAR collaborative measurements observed at different time instants, still showed a Gaussian-like distribution. This characteristic allows to exploit the measurement as a complementary input to the EKF, while guaranteeing the optimality of the filter output. In this context, a comprehensive simulation environment permits a realistic assessment of performances while supporting an empirical validation of algorithm's enhancements to improve the tight-integration process.

1.1 Overview on GNSS

A Global Navigation Satellite System (e.g. GPS, GALILEO, GLONASS, BeiDou) provides accurate location information to users on Earth equipped by a dedicated receiver. A GNSS can support unlimited users since the receivers operates passively, exploiting radionavigation principles. In such a context the position and speed of a mobile user are determined from the estimation of the parameters of an electromagnetic signal transmitted by a satellite. If Line-of-Sight (LOS) propagation is satisfied, these parameters are effectively converted to estimated distances from the transmitters, which can be exploited to retrieve the positioning information if the locations of the sources are known.

A signal characteristic that is proportional to the user-to-satellite distance is the signal propagation time (in LOS condition). In a GNSS, the concept of one-way Time Of Arrival (TOA) ranging is employed to retrieve the time-of-flight information of the signal [14].

This means that the signal must be timestamped with the transmission time and the transmitters must be synchronized, since the user avoid to measuring by itself the time to reach the satellite and come back (one way). As a consequence, the satellites' payloads include highly accurate atomic clocks that are synchronized to a common coordinated time base of the satellite navigation system (i.e. UTC).

The knowledge of the distance from a referenced point in a three-dimensional space locates the user on the surface of a sphere centered about the satellite. The position can be inferred by the intersection of at least three spheres through a trilateration operation, almost without ambiguity [14].

Basically, a GNSS is composed by three segments: a space segment composed by a constellation of satellite vehicles (SV); a control segment, i.e. a network of stations distributed over the Earth, that monitor the status of satellites and signals, occasionally correcting signal generation; and a user segment made of receivers that determine their own position, velocity and time (PVT). Three functionalities are essentially required to the user segment: the identification of the satellites in view, the estimation of the user-to-satellite distance and the consequent trilateration procedure. The latter is illustrated in the following paragraphs.

1.1.1 Solution of the Trilateration Problem

The pseudorange

The position of a generic user i or satellite s are expressed in a three-dimensional cartesian coordinate system by means of the *position states*

$$\underline{\mathbf{x}}_i = (x_i \; y_i \; z_i)^\top \tag{1.1}$$

$$\underline{\mathbf{x}}_s = (x_s \; y_s \; z_s)^\top \tag{1.2}$$

with respect to a given reference system. In order to obtain an estimate of (1.1), a user needs to retrieve the distance from three reference points (i.e. the satellites). The user-to-satellite range is thus defined as

$$r_i^s = ||\underline{\mathbf{x}}_s - \underline{\mathbf{x}}_i|| \; . \tag{1.3}$$

and it can be easily inferred from a measure of the propagation time τ of the signal, according to

$$r_i^s = c \cdot \tau \; , \tag{1.4}$$

where c is the speed of light (i.e. approximately the phase velocity of the signal from satellite's orbit to Earth) and τ is the propagation time required for a signal to reach the user receiver antenna. Notice that generally subscripted indexes refers to ground users while superscripts indicates satellites when this notation does not generate confusion.

As mentioned, the satellites are equipped with high-precision atomic clocks and synchronized time scales are maintained among all the SV of the constellation. Unfortunately, it is not possible to extend the same features to the receivers and their clocks, at low cost and complexity . Indeed the users' clocks generally experience a non-negligible drift and they are not kept synchronized. As a consequence, the actual propagation time measured by the user i is affected by a time misalignment δt_i with respect to system time. For this reason, the range determined by the receiver after processing the signal from satellite s is denoted with ρ_i^s and called *pseudorange*, because includes a contribution dependent from the user clock misalignment. It is then

$$\begin{aligned}\rho_i^s &= c \cdot \tau + c \cdot \delta t_i \\ &= r_i^s + b_i\end{aligned} \tag{1.5}$$

where

$$b_i = c \cdot \delta t_i \tag{1.6}$$

is a quantity measured in meters and related to the user clock offset, called the *user clock bias*.

Actually, another offset affects the pseudorang and it is related to the difference between system time and satellite clock [14]. Nevertheless, the control segment determines the corrections for the satellite clock offsets, which are then broadcasted to the users. Users apply these corrections within the processing of the pseudoranges to compensate for it.

The measure of (1.5) is possible thanks to correlation with PRN codes that modulate the signal and to the aforementioned time-stamping in GNSS signal architecture [14]. A complete illustration of the determination of ρ_i^s is out of the scope of this work and in the rest of the dissertation a measured pseudorange ρ_i^s is assumed available when the user i experiences an unobstructed view of the signal of satellite s.

Being a measured quantity, the pseudorange is affected by error. Several error contributions [14] are present in the signal received by the user, but many of them are compensated by the receiver thanks to a proper modeling of the systematic part [14], so that the residual error ϵ_i is bias-free. Each ϵ_i is modeled as Gaussian i.i.d. with zero-mean and variance σ^2_{UERE}, where the acronym UERE stands for “User Equivalent Range Error” [14]. The pseudorange considered throughout this dissertation is therefore a random variable, such that

$$\rho_i^s \sim \mathcal{N}(r_i^s + b_i, \sigma^2_{UERE}) \ , \tag{1.7}$$

and (1.5) is updated accordingly to include this uncertainty:

$$\begin{aligned}\rho_i^s &= c \cdot \tau + c \cdot \delta t_i + \epsilon_i \\ &= r_i^s + b_i + \epsilon_i\end{aligned} \tag{1.8}$$

Calculation of user position

Because of the necessity of estimation of the user clock bias, a GNSS receiver has to determine four unknowns, in order to obtain the user position without ambiguity. The unknowns are included for convenience in the *state vector*

$$\mathbf{x}_i = (x_i \; y_i \; z_i \; b_i)^\top \ . \tag{1.9}$$

Each pseudorange ρ_i^s is related to the elements of (1.9) through

$$\rho_i^s = \sqrt{(x_s - x_i)^2 + (y_s - y_i)^2 + (z_s - z_i)^2} - b_i \ , \tag{1.10}$$

therefore, solving a system of four equations like (1.10) will determine $\mathbf{x}_i$. The measure of four different pseudoranges is needed in order to solve the following system of equations

$$\begin{cases} \rho_i^1 = \sqrt{(x_1 - x_i)^2 + (y_1 - y_i)^2 + (z_1 - z_i)^2} - b_i \\ \rho_i^2 = \sqrt{(x_2 - x_i)^2 + (y_2 - y_i)^2 + (z_2 - z_i)^2} - b_i \\ \rho_i^3 = \sqrt{(x_3 - x_i)^2 + (y_3 - y_i)^2 + (z_3 - z_i)^2} - b_i \\ \rho_i^4 = \sqrt{(x_4 - x_i)^2 + (y_4 - y_i)^2 + (z_4 - z_i)^2} - b_i \end{cases} \tag{1.11}$$

where the satellite index s goes from 1 to 4.

This set of non-linear equations can be solved in a closed form [15] [16] with a considerable computational burden. An alternative is represented by iterative techniques based on linearization. The elements of (1.9) can be written using incremental quantities (position offsets) w.r.t. a known reference linearization point, such that

$$\mathbf{x}_i = \mathbf{x}_i^* + \mathbf{\Delta x}_i \tag{1.12}$$

where

$$\mathbf{x}_i^* = (x_i^* \quad y_i^* \quad z_i^* \quad b_i^*)^\top \tag{1.13}$$

is the known linearization point and

$$\mathbf{\Delta x}_i = (\Delta x_i^* \quad \Delta y_i^* \quad \Delta z_i^* \quad \Delta b_i^*)^\top \, . \tag{1.14}$$

is the vector of incremental quantities w.r.t. the linearization point itself. We can then write (1.10) as a function of position offsets, exploiting the equality in (1.12). In this way

$$\begin{aligned} \rho_i^s &= \sqrt{(x_s - x_i)^2 + (y_s - y_i)^2 + (z_s - z_i)^2} - b_i \\ &= f(x_i, y_i, z_i, b_i) \\ &= f(x_i^* + \Delta x_i, y_i^* + \Delta y_i, z_i^* + \Delta z_i, b_i^* + \Delta b_i) \end{aligned} \tag{1.15}$$

Once (1.10) is written as a function of incremental quantities it is possible to expand it in a Taylor series about the linearized position vector $\mathbf{x}_i^*$. After a first order truncation, the pseudorange measurement can be obtained as a linear function of the position offsets and the known elements of (1.13), resulting in

$$\begin{aligned} f(x_i, y_i, z_i, b_i) = f(x_i^*, y_i^*, z_i^*, b_i^*) & \\ + \frac{\partial f(x_i^*, y_i^*, z_i^*, b_i^*)}{\partial x_i^*} \Delta x_i &+ \frac{\partial f(x_i^*, y_i^*, z_i^*, b_i^*)}{\partial y_i^*} \Delta y_i \\ + \frac{\partial f(x_i^*, y_i^*, z_i^*, b_i^*)}{\partial z_i^*} \Delta z_i &+ \frac{\partial f(x_i^*, y_i^*, z_i^*, b_i^*)}{\partial b_i^*} \Delta b_i \end{aligned} \tag{1.16}$$

By explicitly computing the partial derivatives

$$\begin{aligned}
\frac{\partial f(x_i^*, y_i^*, z_i^*, b_i^*)}{\partial x_i^*} &= -\frac{x_s - x_i^*}{r_i^{s*}} = -h_{x_s} \\
\frac{\partial f(x_i^*, y_i^*, z_i^*, b_i^*)}{\partial y_i^*} &= -\frac{y_s - y_i^*}{r_i^{s*}} = -h_{y_s} \\
\frac{\partial f(x_i^*, y_i^*, z_i^*, b_i^*)}{\partial z_i^*} &= -\frac{z_s - z_i^*}{r_i^{s*}} = -h_{z_s} \\
\frac{\partial f(x_i^*, y_i^*, z_i^*, b_i^*)}{\partial b_i^*} &= -1
\end{aligned} \tag{1.17}$$

where

$$r_i^{s*} = \sqrt{(x_s - x_i^*)^2 + (y_s - y_i^*)^2 + (z_s - z_i^*)^2}\ , \tag{1.18}$$

we obtain the coefficients of a linearized equation for the pseudorange ρ_i^s. Hence substituting (1.17) in (1.16) the following linear equation is obtained

$$\Delta\rho_i^s = h_{x_s}\Delta x_i + h_{y_s}\Delta y_i + h_{z_s}\Delta z_i + \Delta b_i\ . \tag{1.19}$$

if we set

$$\Delta\rho_i^s = \rho_i^{s*} - \rho_i^s\ . \tag{1.20}$$

This linear expression in the variables in $\mathbf{\Delta x}_i$, can be exploited as an alternative to the non-linear system (1.11), such that

$$\begin{cases}
\Delta\rho_i^1 = h_{x_1}\Delta x_i + h_{y_1}\Delta y_i + h_{z_1}\Delta z_i + \Delta b_i \\
\Delta\rho_i^2 = h_{x_2}\Delta x_i + h_{y_2}\Delta y_i + h_{z_2}\Delta z_i + \Delta b_i \\
\Delta\rho_i^3 = h_{x_3}\Delta x_i + h_{y_3}\Delta y_i + h_{z_3}\Delta z_i + \Delta b_i \\
\Delta\rho_i^4 = h_{x_4}\Delta x_i + h_{y_4}\Delta y_i + h_{z_4}\Delta z_i + \Delta b_i
\end{cases} \tag{1.21}$$

This operation can be expressed in the matrix form

$$\boldsymbol{\Delta}\rho_i = \mathbf{H}\mathbf{\Delta x}_i \tag{1.22}$$

after the definition of

$$\boldsymbol{\Delta}\rho_i = (\Delta\rho_i^1 \;\; \Delta\rho_i^2 \;\; \Delta\rho_i^3 \;\; \Delta\rho_i^4)^\top \tag{1.23}$$

and

$$\mathbf{H} = \begin{pmatrix} h_{x_1} & h_{y_1} & h_{z_1} & 1 \\ h_{x_2} & h_{y_2} & h_{z_2} & 1 \\ h_{x_3} & h_{y_3} & h_{z_3} & 1 \\ h_{x_4} & h_{y_4} & h_{z_4} & 1 \end{pmatrix} \tag{1.24}$$

Then, by solving for $\mathbf{\Delta x}_i$ it is possible to ultimately compute the state vector $\mathbf{x}_i$ through (1.12) since the linearization point is known. The solution is therefore

$$\mathbf{\Delta x}_i = \mathbf{H}^{-1}\boldsymbol{\Delta}\rho_i\ . \tag{1.25}$$

Since, the pseudorange measurements are corrupted by a residual error (Sec. 1.1.1), this error will be projected to $\mathbf{\Delta x}_i$, according to (1.25). The error contribution to $\mathbf{\Delta x}_i$ can be minimized by including more than four measurements in $\mathbf{\Delta}\rho_i$ [14], i.e. by adding lines to matrix $\mathbf{H}$. To this purpose the alternative form

$$\mathbf{\Delta x}_i = (\mathbf{H}^\top \mathbf{H})^{-1} \mathbf{H}^\top \mathbf{\Delta}\rho_i \tag{1.26}$$

is usually employed in receivers, since it holds also if $\mathbf{H}$ is non-invertible, as a non-square matrix will be (provided that $(\mathbf{H}^\top \mathbf{H})^{-1}$ is non-singular).

This linearization procedure will converge to a solution as long as the linearization point is close to the actual user location. To ensure a convergence, this process is usually iterated updating at each step the linearization point $\mathbf{x}_i^*$ with the last computed unknowns $\mathbf{x}_i$. This process takes place within one *fixing epoch* (or *update interval*), which is the time interval between the moment at which a GNSS receiver provides positioning data to the user and the next position output by that receiver (i.e. the inverse of the receiver update rate [17])

1.2 Inter-Agent Range Fundamentals

Generally in satellite navigation systems, a higher number of available ranges mitigates the error contribution and improve the precision of the positioning process. Obtaining a PVT solution is an estimation problem, thus it is no surprise that more observations provide a better quality of the estimate.

The Inter-agent Range (IAR) proposed in [11] is introduced as an additional range to improve positioning performances as well as continuity of PVT solutions in reduced visibility conditions. This collaborative ranging is based on the combination of independent pseudorange measurements and geometrical positioning data coming from two non-synchronized cooperating GNSS receivers. The cooperating receivers are supposed to be part of a communication network and they are called *agents* or *peers* in this context.

1.2.1 A Collaborative GNSS-based Range

Figure 1.1 is considered to illustrate the geometry of a static scenario. The IAR is retrieved by the *aided agent* A with the cooperation of the *aiding agent* B and they are both able to track the satellite s to obtain the related pseudorange. Notice that A and B will be always used in this work to denote the aided and the aiding agent respectively.

The true *baseline vector* between agent A and B is

$$\mathbf{r}_{AB} \triangleq \underline{\mathbf{x}}_B - \underline{\mathbf{x}}_A \tag{1.27}$$

and the inter-agent range is defined as the norm of (1.27), i.e.

$$I_{AB}^s \triangleq ||\underline{\mathbf{x}}_B - \underline{\mathbf{x}}_A|| \ . \tag{1.28}$$

An estimation of (1.28) is the quantity provided by the IAR method.

From the Carnot theorem, the baseline between $\underline{\mathbf{x}}_A$ and $\underline{\mathbf{x}}_B$ in Figure 1.1 can be obtained knowing the other two edges of the triangle and the angle between them. Hence the IAR can be computed through

$$I_{AB}^s = \sqrt{(r_A^s)^2 + (r_B^s)^2 - 2 r_A^s r_B^s \cos\gamma} \ , \tag{1.29}$$

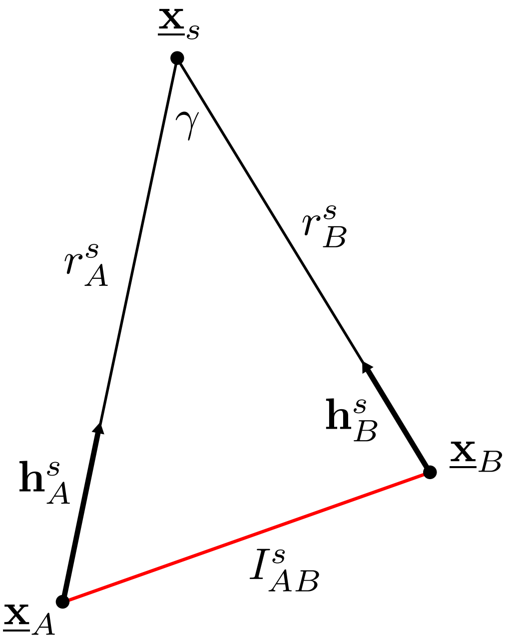

Figure 1.1: IAR computation in a static scenario. A is the aided agent, B is the aiding agent and s is the shared satellite.

where the true user-to-satellite ranges r_A^s and r_B^s are derived from pseudoranges ρ_A^s and ρ_B^s. However these scalar quantities cannot provide information about the angle γ. To this purpose, *unitary steering vectors* define the direction of the vector from the location of an agent i to the position of the satellite s:

$$\mathbf{h}_i^s \triangleq \frac{\underline{\mathbf{x}}_s - \underline{\mathbf{x}}_i}{||\underline{\mathbf{x}}_s - \underline{\mathbf{x}}_i||} \ . \tag{1.30}$$

Their definition is thus exploited in IAR computation to obtain γ:

$$\gamma = \cos^{-1}(\mathbf{h}_A^s \cdot \mathbf{h}_B^s) = \cos^{-1}(\mathbf{h}_A^s {\mathbf{h}_B^s}^\top) \ . \tag{1.31}$$

As a result, (1.29) can be written as

$$I_{AB}^s = \sqrt{(r_A^s)^2 + (r_B^s)^2 - 2r_A^s r_B^s \ \mathbf{h}_A^s {\mathbf{h}_B^s}^\top} \ . \tag{1.32}$$

highlighting all the elements necessary for the baseline length computation through the IAR method: r_A^s, r_B^s, $\mathbf{h}_A^s$, $\mathbf{h}_B^s$. Since all the quantities in (1.32) need to be estimated, the IAR algorithm will provide an estimation of I_{AB}^s, formally referred to as $\hat{I}_{AB}^s$. The symbol "ˆ" denotes the estimator of the underlying variable and this notation will be used throughout all the text. It is worth noticing also, that with this method an estimation of the range between two agents is obtained even with no LOS condition.

1.2.2 IAR Tight Integration

A receiver within a cooperative swarm of agents has the possibility to retrieve the additional ranges as long as it has at least one satellite in LOS. The aiding will be offered by any member of the network which is able to autonomously locate itself with sufficient precision and accuracy. The cooperative ranges retrieved by an aided agent are integrated, extending the PVT algorithm illustrated in Section 1.1. The resulting positioning solution, which merges pseudoranges and collaborative measurements is a *tightly-coupled integration* [18] and will be referred to as GNSS/IAR *hybrid PVT*.

Until now the generic GNSS user has been denoted with the index i. In order to give a clear formalization of the network framework we define also the indexes:

- j for the generic aided agent;
- l for the generic aiding agent;

and moreover:

- the discrete time index k, which denotes the receiver's current fixing epoch;
- the set of visible satellites for the receiver j: $\mathcal{G}_{j,k}$;
- the set of IAR integrated in the PVT algorithm of the receiver j: $\mathcal{I}_{j,k}$;
- the index n which identifies a IAR measurement in the set $\mathcal{I}_{j,k}$.

The non-cooperative PVT algorithm described in Section 1.1 is based on the solution of (1.22) for the incremental vector $\mathbf{\Delta x}_i$. In this context the vector of incremental pseudoranges $\boldsymbol{\Delta\rho}_j$ measured by the aided peer is extended to incorporate also inter-agent ranges, by means of vector composition, resulting in the vector

$$\mathbf{\Delta z}_j = \begin{pmatrix} \boldsymbol{\Delta\rho}_j \\ \hline \mathbf{\Delta I}_j \end{pmatrix} \tag{1.33}$$

where

$$\mathbf{\Delta I}_j = (\Delta I_1 \quad \Delta I_2 \quad \dots \quad \Delta I_{|\mathcal{I}_{j,k}|})^\top \tag{1.34}$$

is a vector of incremental quantities, one for each integrated IAR, similar to $\boldsymbol{\Delta\rho}_j$. Each element ΔI_n of the vector is defined, analogously to (1.20), with respect to the approximation point $\mathbf{x}_j^*$ chosen at each step of the PVT routine of the aided agent j. It is in fact

$$\Delta I_n = I_{jl}^{s*} - I_{jl}^{s} \tag{1.35}$$

where I_{jl}^{s*} is computed according to the baseline definition (1.28), i.e.

$$\begin{aligned} I_{jl}^{s*} &= ||\underline{\mathbf{x}}_l - \underline{\mathbf{x}}_j^*|| \\ &= \sqrt{(x_l - x_j^*)^2 + (y_l - y_j^*)^2 + (z_l - z_j^*)^2}\ . \end{aligned} \tag{1.36}$$

In the end, (1.22) is adapted for the hybrid PVT becoming

$$\mathbf{\Delta z}_j = \bar{\mathbf{H}}\mathbf{\Delta x}_j \tag{1.37}$$

where $\bar{\mathbf{H}}$ is necessarily an extended version of (1.24), that includes the first order derivatives that are the coefficients associated to the elements of $\mathbf{\Delta I}_j$, analogously to (1.21).

Following the same procedure reported in Section 1.1 in order to write (1.28) in a linearized form, the first order partial derivatives are computed after the Taylor expansion:

$$\begin{aligned}
\frac{\partial I_{jl}^{s*}}{\partial x_j^*} &= -\frac{x_l - x_j^*}{I_{jl}^{s*}} = -\hbar_{x_n} \\
\frac{\partial I_{jl}^{s*}}{\partial y_j^*} &= -\frac{y_l - y_j^*}{I_{jl}^{s*}} = -\hbar_{y_n} \\
\frac{\partial I_{jl}^{s*}}{\partial z_j^*} &= -\frac{z_l - z_j^*}{I_{jl}^{s*}} = -\hbar_{z_n} \\
\frac{\partial I_{jl}^{s*}}{\partial b_j^*} &= 0
\end{aligned} \tag{1.38}$$

It should be noticed from (1.38) that the computation of coefficients requires the knowledge of the aiding agent position $\underline{\mathbf{x}}_l$, in analogy with the non-cooperative PVT, where the knowledge of the satellite location is demanded (1.17). The coefficients in (1.38) are then included in the sub-matrix $\mathbf{H}_I$ such that

$$\bar{\mathbf{H}} = \left(\begin{array}{c} \mathbf{H} \\ \hline \mathbf{H}_I \end{array}\right) = \left(\begin{array}{cccc}
h_{x_1} & h_{y_1} & h_{z_1} & 1 \\
h_{x_2} & h_{y_2} & h_{z_2} & 1 \\
\vdots & \vdots & \vdots & \vdots \\
h_{x_{|\mathcal{G}_k|}} & h_{y_{|\mathcal{G}_k|}} & h_{z_{|\mathcal{G}_k|}} & 1 \\
\hline
\hbar_{x_1} & \hbar_{y_1} & \hbar_{z_1} & 0 \\
\hbar_{x_2} & \hbar_{y_2} & \hbar_{z_2} & 0 \\
\vdots & \vdots & \vdots & \vdots \\
\hbar_{x_{|\mathcal{I}_k|}} & \hbar_{y_{|\mathcal{I}_k|}} & \hbar_{z_{|\mathcal{I}_k|}} & 0
\end{array}\right) \tag{1.39}$$

and finally the unknowns in $\mathbf{\Delta x}_j$ can be computed through

$$\mathbf{\Delta x}_j = (\bar{\mathbf{H}}^\top \bar{\mathbf{H}})^{-1} \bar{\mathbf{H}}^\top \mathbf{\Delta z}_j \tag{1.40}$$

with the same method exploited in (1.26).

Notice that the inter-agent range, as retrieved by (1.32), is not dependent on the clock bias b_j of the aided agent, like the pseudorange does. For this reason the last partial derivative in (1.38) is zero. It will be shown (Sec. 2.4.2), that in order to have an estimate of I_{jl}^s free from the clock biases of agents j and l, a non-negligible error contribution is added to the cooperative measurement. If instead no correction of the clock bias of the aiding agent j would be done, such clock bias contribution b_j would be present in all the IAR measurements included in $\mathbf{\Delta I}_j$. If this would be the case, b_j can be computed also with the contribution of IAR measurements as it happens in the non-cooperative PVT, where the pseudoranges are exploited to calculate b_j thanks to a non-null derivative in (1.17). Since I_{jl}^s would be dependent on b_j, I_{jl}^{s*} would be defined accordingly, thus resulting in a non-null partial derivative:

$$\frac{\partial I_{jl}^{s*}}{\partial b_j^*} \neq 0 \tag{1.41}$$

This alternative procedure can be adopted only if the partial derivative in (1.41) can be calculated. Further research will be hopefully oriented to this method, since it has the potential to reduce the uncertainty on the estimation of I_{jl}^{s}.

Multiple IARs and Correlated IARs

A few words have to be also spent on the set of integrated IAR measurements $\mathcal{I}_{j,k}$, whose cardinality determines the dimensions of the vector $\mathbf{\Delta I}_j$ and the sub-matrix $\mathbf{H}_I$. To each aiding agent l able to interact with j to provide the cooperative range corresponds an estimate of a different euclidean distance (the baseline between the two agents). Actually, if the collaborating peers j and l share more than one satellite, the aided peer can obtain more than one range from the aiding agent. But these estimated ranges would refer to the same euclidean distance between the two. They are therefore contextually called *multiple IARs*. The set $\mathcal{I}_{j,k}$ may include any I_{jl}^{s} coming from all possible aiding agent l and shared satellite s for an aided agent j. In this case its cardinality $|\mathcal{I}_{j,k}|$ is the total number of ranges that j is capable to obtain. This terminology will be often used to distinguish a set of all the available cooperative measures, even *multiple IARs*, from a set of IARs relative to the measure of distinct baselines (*unique IARs*).

It should be remarked also that several cooperative ranges can be obtained by j using the same satellite s that is shared with multiple cooperating agents. This would lead to different IAR measures, that represent an estimation of different euclidean distances among peers. However, this class of ranges are highly correlated, since they are based on one common measurement: the pseudorange of the aided agent ρ_j^s. Cooperative ranges from this category will be referred to as *correlated IARs*, and they will be mainly treated in Section 2.1.3.

1.2.3 Virtual Landmarks

As underlined in Section 1.2.2, in order to build the hybrid matrix $\bar{\mathbf{H}}$ and obtain an estimate of $\mathbf{\Delta x}_A$ through (1.40), the position of the aiding agents must be known at the aided agent A as well as the position of the satellites. In fact, since we are solving a trilateration problem, the locations of the reference landmarks from which the ranges are measured must be known, weather they are pseudoranges or IAR.

In a network of collaborating peers, the knowledge of $\underline{\mathbf{x}}_B$ at the receiver A may cause privacy problems, especially in ad hoc networks where validation of the user identity may be an issue. However, a method to preserve the confidentiality among the collaborating agents has been developed in [13] and it is here briefly reported.

The idea behind this technique is to mask the position information through the use of *Virtual Landmarks* (VL), while preserving the reliability of the cooperative ranging. Essentially an aiding agent generates an arbitrary set of position coordinates (the VL), over which the computation of the necessary variables to retrieve the IAR will be based. In other words, a new user-to-satellite range $r_{\tilde{B}}^{s}$ is generated by translating $\underline{\mathbf{x}}_B$ on the virtual landmark $\underline{\mathbf{x}}_{\tilde{B}}$. First, the new range is calculated in its vectorial form $\mathbf{r}_{\tilde{B}}^{s}$ by means of the *displacement vector* $\delta\underline{\mathbf{x}}_{B\to\tilde{B}}$, which is arbitrarily chosen from the aiding agent to conceal its position information. Therefore

$$\mathbf{r}_{\tilde{B}}^{s} = r_{B}^{s} \cdot \mathbf{h}_{B}^{s} + \delta\underline{\mathbf{x}}_{B\to\tilde{B}} \ . \tag{1.42}$$

The range vector $\mathbf{r}^s_{\tilde{B}}$ is then decomposed in the range $r^s_{\tilde{B}}$ and its unitary steering vector $\mathbf{h}^s_{\tilde{B}}$, such that

$$r^s_{\tilde{B}} = ||\mathbf{r}^s_{\tilde{B}}|| \tag{1.43}$$

$$\mathbf{h}^s_{\tilde{B}} = \frac{\mathbf{r}^s_{\tilde{B}}}{r^s_{\tilde{B}}} \ . \tag{1.44}$$

Since the variables related to the aiding peer in (1.32) are now based on the virtual landmark $\underline{\mathbf{x}}_{\tilde{B}}$, the IAR computation between A and B becomes

$$I^s_{A\tilde{B}} = \sqrt{(r^s_A)^2 + (r^s_{\tilde{B}})^2 - 2 r^s_A r^s_{\tilde{B}}\, \mathbf{h}^s_A \mathbf{h}^{s\top}_{\tilde{B}}} \ . \tag{1.45}$$

These operations are illustrated in Figure 1.2.

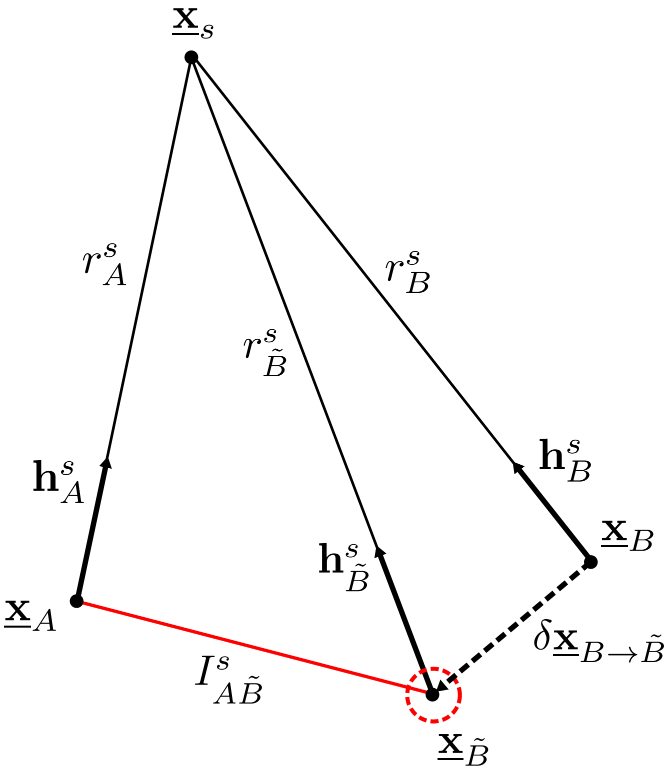

Figure 1.2: IAR computation in a static scenario with Virtual Landmark. $\underline{\mathbf{x}}_B$ is the position of the aiding agent, while $\underline{\mathbf{x}}_{\tilde{B}}$ is the Virtual Lanmark generated by the agent B.

The resulting cooperative range is now coherent with $\underline{\mathbf{x}}_{\tilde{B}}$, therefore the latter is the reference position that must be included in the cooperative sub-matrix $\mathbf{H}_I$ in (1.39). In other words, the generic aiding peer positions $\underline{\mathbf{x}}_l$ in (1.39) are replaced with their respective virtual landmarks $\underline{\mathbf{x}}_{\tilde{l}}$ and the confidentiality is preserved.

In summary, to accomplish the cooperative positioning procedure and take advantage of the additional measurements in the PVT computation, several quantities provided by the two cooperating agents are essential: some related to the agent A (r^s_A, $\mathbf{h}^s_A$) and some to the agent B (r^s_B, $\mathbf{h}^s_B$ or their VL counterparts $r^s_{\tilde{B}}$, $\mathbf{h}^s_{\tilde{B}}$). Furthermore the position $\underline{\mathbf{x}}_B$ of the aiding agent (or the VL translation $\underline{\mathbf{x}}_{\tilde{B}}$) is also needed. Unfortunately, knowing their true values is not possible in a real implementation and nothing has been said so far on their estimation process.

The rest of the thesis is organized as described in the following paragraphs. The next chapter will be devoted to the estimation procedures of such variables and the issues related to these processes. In particular, the constraints related to variable estimations and timing of the IAR computation led to the definition of two alternative novel algorithms for IAR retrieval, that include predictive stages based on Kalman filters. Furthermore, the effects on the cooperative measurements of each single estimation process are deeply studied either isolated or in combination.

A dedicated hybrid PVT algorithm based on Extended Kalman Filter (EKF) is also presented, highlighting the main differences with respect to non-cooperative PVT. Ad hoc solutions are designed in order to specifically adapt this filter to the IAR paradigm. The estimation processes and the properly designed EKF for the PVT will eventually merge in the two complete cooperative positioning algorithms that are described in this chapter.

Following the definition of specific procedures for IAR positioning, an experimental evaluation of the effectiveness of this method will be performed by means of a Monte Carlo simulation. Therefore the third chapter is focused on the simulation environment. This chapter provides a mathematical formalization for the modeling of visibility conditions of the agents and their consequent role in the cooperation. This mathematical framework will be extensively exploited during the simulation. In addition, a description of environment dynamics is provided, particularly focused on the noise sources and the modeling of the latter within the simulation environment.

Finally an extensive analysis of experimental results is reported in Chapter 4. Several scenarios are simulated, involving sky visibility, motion dynamics and network constraints. Moreover throughout the chapter a fine-tuning of the algorithms and EKF-based hybrid PVT proposed in Chapter 2 is carried out and assessed through experimental results. Selection strategies on the set of available cooperative ranges are proposed and evaluated as well. Eventually the resulting improved algorithm is tested in a dedicated simulation experiment and compared to the earlier IAR positioning method. The proposed algorithm is ultimately validated as a valuable cooperative solution for positioning, that also allows navigation data protection and does not require Line-of-Sight condition.

Chapter 2

Methodology and IAR Analysis

Before taking advantage of the Inter-agent range in positioning, the problem of a feasible retrieval of the involved quantities must be faced. To this purpose, ad hoc methods have been developed, either defined in previous works or extended to suite this comprehensive study. Such methodology must cope with the requirements of Inter-agent formula, while sustaining all the environmental constraints.

This chapter provides a detailed description of the methods employed within the context of the IAR estimation algorithm, and their consequences on the collaborative measure.

As a first innovation to the existing method, the hybridized positioning technique described in [11] is here integrated into an Extended Kalman Filter (EKF) for providing a fast-convergent PVT solution suited to a dynamic context. The estimated Inter-Agent Range is then defined and the issues related to the retrieval of variables involved are introduced. In particular, a motion prediction technique is needed and two different approaches to accomplish it are presented: one based on EKF and the other on a plain Kalman Filter (KF). Finally, the collaborative algorithm for the exchange of information presented in [11] is here adapted to the requirements of variable estimations and predictions. Within this context, a specific time sequence of operations is defined with respect to the round-trip time (RTT) of the network and tailored to variable estimation constraints.

After this exhaustive explanation of the procedure steps necessary to accomplish the IAR estimation, the statistical characteristics of the latter are presented. In particular, a deep analysis on the effects caused by the involved parameters and techniques on the IAR measure is given. Among the various factors of impact, the most critical ones are studied in isolation, where possible, and through their overall combined effect in a final section, in order to provide a meaningful characterization for a realistic scenario.

2.1 Extended Kalman Filter IAR Tight Integration

The Kalman Filter[19] is widely used in GNSS receivers. It provides a linear, unbiased and optimal estimate of the state of a dynamical system from its noisy measurements. The Extended Kalman Filter (EKF) is a KF version able to deal with non-linear systems (such as the pseudorange equations 1.11), and therefore it is widely employed in the navigation community to determine the PVT. The EKF works by means of a linearization around an approximation point, so its capacity to treat non-linear systems is good as long as a first-order approximation is a sufficient model [20]. The linearization procedure is analogous to the one employed in the LMS solution (Section 1.1), using the jacobian matrix $\mathbf{H}$ as a *measurement matrix* of the EKF. Therefore a *tight integration* of cooperative measurements can be implemented using the hybrid observation matrix $\bar{\mathbf{H}}$ in the EKF as well.

The EKF algorithm is illustrated below, as could be applied to agents in a cooperative network. A receiver employs the EKF to compute its position, but within this context, it may incorporate different type of measurements (pseudorange or IARs). Here the EKF steps are illustrated in its cooperative adaptation, i.e. as performed by the aided agents (exploiting hybrid observation matrix $\bar{\mathbf{H}}$). Despite this, the operations are essentially the same of the regular EKF, thus this section is intended also as a general review of the filter equations.

With respect to LMS theory introduced in Section 1.1, the position state $\mathbf{x}_{i,k}$ indicates explicitly the discrete time index k and has been extended to incorporate velocity variables. The state of a generic agent i at a given time instant k is

$$\mathbf{x}_{i,k} = (x_{i,k} \;\; y_{i,k} \;\; z_{i,k} \;\; \dot{x}_{i,k} \;\; \dot{y}_{i,k} \;\; \dot{z}_{i,k} \;\; b_{i,k} \;\; \dot{b}_{i,k})^\top \tag{2.1}$$

where three dimensional coordinates and relative axial velocities are considered. States $b_{i,k}$ and $\dot{b}_{i,k}$ are the receiver clock bias and its derivative (clock drift) respectively. In the following the agent's index i will be omitted for simplicity.

It should be reminded that the basic state variables of the EKF are incremental quantities [20]. However, since it is convenient to keep track of the total quantities (position, velocity, etc.), the incremental form of variables will be avoided where possible, in the following filter description.

The observation matrix $\bar{\mathbf{H}}$ is extended as well, with respect to Section 1.2, in order to be consistent with the above definition of position state. It is

$$\bar{\mathbf{H}}_k = \left(\begin{array}{c} \mathbf{H}_k \\ \hline \mathbf{H}_{I,k} \end{array} \right) = \left(\begin{array}{cccccccc} h_{x_1} & h_{y_1} & h_{z_1} & 0 & 0 & 0 & 1 & 0 \\ h_{x_2} & h_{y_2} & h_{z_2} & 0 & 0 & 0 & 1 & 0 \\ \vdots & \vdots & \vdots & \vdots & \vdots & \vdots & \vdots & \vdots \\ h_{x_{|\mathcal{G}_k|}} & h_{y_{|\mathcal{G}_k|}} & h_{z_{|\mathcal{G}_k|}} & 0 & 0 & 0 & 1 & 0 \\ \hline \hbar_{x_1} & \hbar_{y_1} & \hbar_{z_1} & 0 & 0 & 0 & 0 & 0 \\ \hbar_{x_2} & \hbar_{y_2} & \hbar_{z_2} & 0 & 0 & 0 & 0 & 0 \\ \vdots & \vdots & \vdots & \vdots & \vdots & \vdots & \vdots & \vdots \\ \hbar_{x_{|\mathcal{I}_k|}} & \hbar_{y_{|\mathcal{I}_k|}} & \hbar_{z_{|\mathcal{I}_k|}} & 0 & 0 & 0 & 0 & 0 \end{array} \right) \tag{2.2}$$

where elements h_{x_s},h_{y_s} and h_{z_s} are components of steering vectors steered toward satellite s, and $\hbar_{x_j}$,$\hbar_{y_j}$ and $\hbar_{z_j}$ are pointing at collaborating peers, as defined in Section 1.2. Furthermore, they are all based on the approximation point $\mathbf{x}_k^*$. Notice that generally more than one line of the matrix $\mathbf{H}_{I,k}$ may refer to the same aiding agent providing multiple IAR from different satellites.

2.1.1 Models Equations

The Extended Kalman filter theory is based on a *system model equation* and on a *measurement model equation*. They are briefly recalled for the sake of completeness.

The system model equation considered in this framework is a linear equation. Hence it describes the relation between past and current state by means of a *transition matrix*:

$$\mathbf{x}_k = \mathbf{\Phi}\mathbf{x}_{k-1} + \eta \ . \tag{2.3}$$

being $\mathbf{\Phi}$ the transition matrix

$$\mathbf{\Phi} = \begin{pmatrix} 1 & 0 & 0 & T_s & 0 & 0 & 0 & 0 \\ 0 & 1 & 0 & 0 & T_s & 0 & 0 & 0 \\ 0 & 0 & 1 & 0 & 0 & T_s & 0 & 0 \\ 0 & 0 & 0 & 1 & 0 & 0 & 0 & 0 \\ 0 & 0 & 0 & 0 & 1 & 0 & 0 & 0 \\ 0 & 0 & 0 & 0 & 0 & 1 & 0 & 0 \\ 0 & 0 & 0 & 0 & 0 & 0 & 1 & T_s \\ 0 & 0 & 0 & 0 & 0 & 0 & 0 & 1 \end{pmatrix} \tag{2.4}$$

where T_s is the time step; and η is the *system noise* such that

$$\eta \sim \mathcal{N}(\mathbf{0}, \mathbf{Q}) \tag{2.5}$$

with $\mathbf{Q}$ covariance matrix.

The measurement model equation provides a relation between the state $\mathbf{x}_k$ and the measurements $\mathbf{z}_k$. For what concern GNSS systems this relation is non-linear, thus the equation is in the form

$$\mathbf{z}_k = h(\mathbf{x}_k) + \mathbf{v}_k \tag{2.6}$$

where h is a known non-linear function. In the equation, $\mathbf{v}_k$ represents the measurement noise and it is modeled such that

$$\mathbf{v}_k \sim \mathcal{N}(\mathbf{0}, \bar{\mathbf{R}}) \tag{2.7}$$

with $\bar{\mathbf{R}}$ covariance matrix.

Since the relationship between position state variables and pseudoranges cannot be described by a linear equation [14], the EKF exploits linearization to deal with the trilateration problem. The *linearized measurement equation* is

$$\Delta\mathbf{z}_k = \bar{\mathbf{H}}_k \Delta\mathbf{x}_k + \mathbf{v}_k \tag{2.8}$$

where $\Delta\mathbf{z}_k$ and $\Delta\mathbf{x}_k$ are vectors build around a chosen approximation point $\mathbf{x}_k^*$. $\Delta\mathbf{x}_k$ is the difference between the actual state and the linearization point, such that

$$\mathbf{x}_k = \mathbf{x}_k^* + \Delta\mathbf{x}_k \ . \tag{2.9}$$

$\Delta\mathbf{z}_k$ is the *incremental measurement vector* [20] and it is defined as

$$\Delta\mathbf{z}_k = \mathbf{z}_k - h(\mathbf{x}_k^*) \ . \tag{2.10}$$

$\mathbf{z}_k$ is the measurement vector and collects all the ranges that the agent has estimated, while $h(\mathbf{x}_k^*)$ is the measurements vector computed from the approximation point in the absence of noise. It is then a vector of pseudo-distances between $\mathbf{x}_k^*$ and the landmarks (satellites or collaborative peers). In view of the above, the vector of incremental measurements $\Delta\mathbf{z}_k$ is simply the set of differential ranges in Section 1.2.

2.1.2 EKF Routine

The EKF routine starts with a prediction step that involves the projection of the last *state estimation* $\hat{\mathbf{x}}_{k-1}$ on the current instant k by means of the transition matrix:

$$\hat{\mathbf{x}}_k^- = \mathbf{\Phi}\hat{\mathbf{x}}_{k-1} \ . \tag{2.11}$$

At each step of the EKF routine, the predicted state estimation $\hat{\mathbf{x}}_k^-$ is chosen as linearization point $\mathbf{x}_k^*$, around which incremental quantities are build. Then, the incremental measurements $\Delta\mathbf{z}_k$ and the hybrid matrix $\bar{\mathbf{H}}_k$ are computed w.r.t. this reference point. The prediction is performed also on the *error covariance matrix* $\mathbf{P}_{k-1}$:

$$\mathbf{P}_k^- = \mathbf{\Phi}\mathbf{P}_{k-1}\mathbf{\Phi}^\top + \mathbf{Q} \ . \tag{2.12}$$

Following the prediction phase, the *Kalman gain* is computed as

$$\mathbf{K}_k = \mathbf{P}_k^-\bar{\mathbf{H}}_k^\top(\bar{\mathbf{H}}_k\mathbf{P}_k^-\bar{\mathbf{H}}_k^\top + \bar{\mathbf{R}})^{-1}. \tag{2.13}$$

Notice that the gain is dependent on the measurement matrix $\bar{\mathbf{H}}_k$, which, as stated, is updated according to the approximation point at each time k. Therefore, since $\mathbf{x}_k^* = \hat{\mathbf{x}}_k^-$, the gain sequence will depend on the sequence of measurements of a particular realization of the experiment [20].

Now, considering the incremental state estimate

$$\Delta\hat{\mathbf{x}}_k = \Delta\hat{\mathbf{x}}_k^- + \mathbf{K}_k(\Delta\mathbf{z}_k - \bar{\mathbf{H}}_k\Delta\hat{\mathbf{x}}_k^-) \tag{2.14}$$

it should be noticed that, since $\mathbf{x}_k^* = \hat{\mathbf{x}}_k^-$, the term $\Delta\hat{\mathbf{x}}_k^-$ is zero. Thus the equation 2.14 becomes

$$\Delta\hat{\mathbf{x}}_k = \mathbf{K}_k\Delta\mathbf{z}_k \ . \tag{2.15}$$

Finally the state estimation can be obtained by correcting the approximation state with the incremental estimate update:

$$\hat{\mathbf{x}}_k = \mathbf{x}_k^* + \Delta\hat{\mathbf{x}}_k \ . \tag{2.16}$$

The error covariance matrix is updated as well. This equation is implemented in a symmetric form (Joseph form), which is resilient to divergence phenomena [20]:

$$\mathbf{P}_k = (\mathbf{I} - \mathbf{K}_k\bar{\mathbf{H}}_k)\mathbf{P}_k^-(\mathbf{I} - \mathbf{K}_k\bar{\mathbf{H}}_k)^\top + \mathbf{K}_k\bar{\mathbf{R}}_k\mathbf{K}_k^\top \ . \tag{2.17}$$

2.1.3 Definition of Covariance Matrices

A few words should be additionally spent about the generation of noise covariance matrices $\mathbf{Q}_k$ and $\bar{\mathbf{R}}_k$. A suitable system noise covariance matrix can be generated through a model provided by Brown [20], which is based on time step T_s and spectral densities of the white noise driving functions of system model (2.3). The configuration is briefly reported:

$$\mathbf{Q}_k = \begin{pmatrix} \frac{S_pT_s^3}{3} & 0 & 0 & \frac{S_pT_s^2}{2} & 0 & 0 & 0 & 0 \\ 0 & \frac{S_pT_s^3}{3} & 0 & 0 & \frac{S_pT_s^2}{2} & 0 & 0 & 0 \\ 0 & 0 & \frac{S_pT_s^3}{3} & 0 & 0 & \frac{S_pT_s^2}{2} & 0 & 0 \\ \frac{S_pT_s^2}{2} & 0 & 0 & S_pT_s & 0 & 0 & 0 & 0 \\ 0 & \frac{S_pT_s^2}{2} & 0 & 0 & S_pT_s & 0 & 0 & 0 \\ 0 & 0 & \frac{S_pT_s^2}{2} & 0 & 0 & S_pT_s & 0 & 0 \\ 0 & 0 & 0 & 0 & 0 & 0 & S_fT_s + \frac{S_gT_s^3}{3} & \frac{S_gT_s^2}{2} \\ 0 & 0 & 0 & 0 & 0 & 0 & \frac{S_gT_s^2}{2} & S_gT_s \end{pmatrix} . \tag{2.18}$$

The parameters S_p,S_f and S_g are the spectral densities related to the system noise η. They are associated, respectively, with the the position variables (x,y,z), the user clock bias error b_i, and the user clock drift $\dot{b}_i$[1].

Each row of the covariance matrix $\bar{\mathbf{R}}_k$ models the noise of the correspondent measurement that feeds the EKF. When measurement are pseudoranges, the relative covariance matrix is usually a diagonal matrix, with pseudorange variances σ^2_{UERE} on the main diagonal, since no correlation is assumed between these quantities [20]. In this cooperative framework however, also IAR measures are involved in the measurement process and therefore the matrix $\bar{\mathbf{R}}_k$ should include elements associated to these quantities. In particular, each IAR measurement is dependent on one of the pseudoranges included in the measurement vector such that cross-correlation terms have to be taken into account for the filter design.

The error covariance matrix designed for the proposed algorithm is no longer diagonal, it is indeed defined as

$$\bar{\mathbf{R}}_k = \left(\begin{array}{c|c} \mathbf{R}_\rho & \mathbf{R}_{\rho I} \\ \hline \mathbf{R}_{\rho I}^\top & \mathbf{R}_I \end{array}\right) \tag{2.19}$$

where the sub-matrix $\mathbf{R}_\rho$ is a $|\mathcal{G}_k| \times |\mathcal{G}_k|$[2] diagonal covariance matrix with values defined according to the σ^2_{UERE} of each pseudorange.

Similarly the sub-matrix $\mathbf{R}_I$ is a $|\mathcal{I}_k| \times |\mathcal{I}_k|$[3] matrix. If no *correlated IARs* are considered, the IAR measurements will be all dependent on distinct pseudorange measurements. As a consequence, cooperative ranges will be uncorrelated among each other and this sub-matrix will include only diagonal elements. These non-null elements are the variances of the measurements $\hat{I}^s_{jl}$.

---

[1] Actually the spectral densities parameters may be considered static throughout an observation time, even if the system noise is a time-dependent process. As a consequence $\mathbf{Q}_k = \mathbf{Q}$.

[2] $|\mathcal{G}_k|$ is the number of visible satellites for an agent at time k. Similar sets were defined in Section 1.2.

[3] $|\mathcal{I}_k|$ is the number of cooperative ranges that an agent is able to retrieve at time k.

The investigation presented in [12] provides an useful upper bound for the variance of estimated IAR:

$$\sigma^2_{\hat{I}} \leq \sigma^2_{UERE,j} + \sigma^2_{UERE,l} \tag{2.20}$$

where j and l are the two agents involved in the cooperation. This result can be exploited to adapt the measurement matrix to the IAR method, while being conservative in the trust granted to the cooperative range. A further investigation in Sec. 4.3 will pursue less conservative methods that include proper weighting of the upper bound on the basis of experimental performances of the resulting matrix $\bar{\mathbf{R}}_k$.

The $\mathbf{R}_{\rho I}$ sub-matrix contains the cross-correlation terms which link pseudorange measurements and IAR contributions. For these terms, the Cauchy-Schwarz inequality can be exploited to assign to the covariance terms a value according to their lower or upper bound, defined as

$$|\sigma_{\hat{I}\rho}| \leq \sqrt{\sigma^2_{\hat{I}} \cdot \sigma^2_{UERE,j}} \; . \tag{2.21}$$

The transposed matrix $\mathbf{R}^{\top}_{\rho I}$ can be then defined accordingly.

Assigning the maximum correlation between $\hat{I}^s_{jl}$ and ρ^s_j is a worst-case assumption. Thus, a proper weight on this bound will be again discussed through experimental assessment in Section 4.3. It should be underlined, however, that to exploit (2.19) as a model for the integrated measurements, the latter should be normally distributed in order to satisfy the Gaussian assumption [20]. This will prevent the EKF to be sub-optimal when dealing with IARs.

This concludes the illustration of the EKF routine adapted for IAR collaborative positioning. The equations are not so far from the computational steps of a plain Kalman filter. In fact, even if it is applied on non-linear problems, the EKF involves linear dynamics by means of incremental quantities and linearization. As a matter of fact, the error covariance equations (2.12) and (2.17), and the Kalman gain equation (2.13) are the same as in the case of the regular Kalman filter.

2.1.4 Choice of the Linearization Point

A problem to be faced, is the choice of the linearisation point $\mathbf{x}^*_k$. The use of the estimated trajectory $\hat{\mathbf{x}}^-_k$ is a reasonable choice, since it is presumably the best estimate available at time k before the measurement update. However, a poor choice for $\mathbf{x}^*_k$ could cause the EKF estimate to diverge if the first-order approximation on which the linearization is based is not enough. Due to the feedback of measurements into the estimate equations, instability phenomena may arise in the EKF. Several works have investigated the conditions for EKF stability [21] [22], but such requirements are often too restrictive for realistic applications [22].

This problem is especially critical in the initialization phase of the filter, when the information on the position is scarce. In this phase, in order to select a $\mathbf{x}^*_0$, a LMS routine is commonly employed [20], but it needs at least 4 ranges at disposal to converge to a solution. Through IAR cooperative ranging the outage events are massively reduced and a re-initialization of this kind is often possible, eventually compensating a divergent EKF estimate sequence.

2.2 Estimated Inter-agent Range

The previous section was dedicated to the tight integration of cooperative ranges in the hybrid PVT algorithm implemented through an EKF. Nevertheless, a description of the estimation procedures necessary to ultimately retrieve the Inter-agent ranges is still missing. The quantity involved in the IAR formula are known from Section 1.2, but their estimation in a realistic scenario is not trivial and certainly requires to be illustrated. This is the objective of the current section.

The basic formula for IAR calculation (1.32) was defined in Section 1.2. In (1.32) the indexes A and B are employed to unambiguously underline specific roles in cooperation (aided and aiding agent). Remember, however, that the pieces of information that B is willing to share with the aided agent A are all based on its generated virtual landmark $\tilde{B}$, as discussed in Section 1.2.3. For the sake of simplicity, the index $\tilde{B}$ is generally omitted in favor of B, except for the last part of the section where the virtual landmark solution is recalled. As usual the index i indicates a generic agent. Notice also that the time index k is omitted as well throughout this section, assuming for each variable the same associated time instant.

Ranges r_A^s and r_B^s are part of the set of elements to be retrieved. The information on these ranges is carried by the respective pseudoranges ρ_A^s and ρ_B^s, but the user clock biases error b_A and b_B need to be removed first. The *corrected psuedoranges* are thus obtained for any agent i as

$$\tilde{r}_i^s = \rho_i^s - b_i \ . \tag{2.22}$$

Recalling Section 1.1, the pseudorange here considered are bias-free, i.e.

$$\rho_i^s \sim \mathcal{N}(r_i^s + b_i,\, \sigma_{UERE}^2) \tag{2.23}$$

and consequently

$$\tilde{r}_i^s \sim \mathcal{N}(r_i^s,\, \sigma_{UERE}^2) \ . \tag{2.24}$$

Unfortunately, a perfect knowledge of the user clock bias is not possible and an estimation of it must be provided in this phase. As a consequence, the estimated IAR formula will necessary include the corrected pseudorange estimations $\hat{r}_A^s$ and $\hat{r}_B^s$, whose probability distribution depends on the characteristics of the random variables $\hat{b}_A$ and $\hat{b}_B$ (estimated user clock biases). Summarizing, to retrieve an estimation of the range variables in (1.32), four quantities are needed: ρ_A^s and $\hat{b}_A$ for the aided agent, and ρ_B^s and $\hat{b}_B$ for the aiding agent. Their relation is

$$\begin{aligned} \hat{r}_A^s &= \rho_A^s - \hat{b}_A \\ \hat{r}_B^s &= \rho_B^s - \hat{b}_B \ . \end{aligned} \tag{2.25}$$

The two pseudoranges are independently measured by the two GNSS receivers, but the estimation of a user clock bias b_i would need a convergent PVT stage that computes the state $\mathbf{x}_{i,k}$ of the agent, or, at least, the non-derivative elements x_i, y_i, z_i and b_i in (2.1).

In the context of the proposed method, it is assumed that the receiver that plays the role of aiding agent is always able to autonomously locate itself with sufficient precision and accuracy, i.e. to obtain a reliable PVT solution without additional ranges. Its GNSS positioning algorithm provides, among other state variables, $\hat{b}_B$, which is certainly its best estimate of the user clock bias error. On the contrary, the aided agent experiences poor GNSS visibility conditions, thus additional ranges may be essential to obtain a convergent PVT solution. However, in order to retrieve additional cooperative ranges, A would have to get its user clock bias from a reliable PVT algorithm and so forth, resulting in a deadlock.

The solution for this agent is to estimate b_A through a predictive filter. Moreover, since it is eligible for being aided, at least one updated pseudorange is available to the agent A. In fact, in order to retrieve a IAR measure, a satellite signal must be tracked by both the receivers involved in the cooperative procedure, i.e. at least one satellite must be visible. As a result, even if the pseudoranges are less than four (thus potentially leading to an underestimated PVT problem), they are conveniently exploited at the last stage of the IAR estimation process to obtain a clock bias estimate (Sec. 2.3). For this reasons, an Extended Kalman Filter is a good choice as predictive filter, since it integrates the available measurements and compensates for their scarcity with a model of the dynamics of the system. Hence, besides being used in the hybrid PVT stage to provide a cooperatively-obtained position, the EKF is also used at this preliminary stage, for the estimation of variables involved in IAR estimation process. This is the critical part of the estimation of r_A^s and r_B^s and further details on it will be presented in Section 2.3 discussing prediction techniques.

The other two important actors in the IAR computation (1.32) are the steering vectors $\mathbf{h}_A^s$ and $\mathbf{h}_B^s$. These quantities needs to be estimated as well and the definition of estimated steering vectors comes easily after (1.30), where position states $\underline{\mathbf{x}}_i$ and $\underline{\mathbf{x}}_s$ are replaced by estimated quantities:

$$\hat{\mathbf{h}}_i^s = \frac{\underline{\mathbf{x}}_s - \hat{\underline{\mathbf{x}}}_i}{||\underline{\mathbf{x}}_s - \hat{\underline{\mathbf{x}}}_i||} \ . \tag{2.26}$$

When computing $\hat{\mathbf{h}}_A^s$ and $\hat{\mathbf{h}}_B^s$ through (2.26), the satellites position $\underline{\mathbf{x}}_s$ is known at the receiver after the demodulation of the navigation message. The variables $\hat{\underline{\mathbf{x}}}_A$ and $\hat{\underline{\mathbf{x}}}_B$ are instead estimated through a PVT algorithm.

The problem of their estimation is analogous to the issues related to $\hat{b}_A$ and $\hat{b}_B$ since, while $\hat{\mathbf{h}}_B^s$ can be based on the output $\hat{\underline{\mathbf{x}}}_B$ of a non-cooperative PVT, $\hat{\mathbf{h}}_A^s$ must be, at least partially, predicted due to the impossibility of A to have a sufficiently reliable position estimate $\hat{\underline{\mathbf{x}}}_A$ without cooperation.

A predictive filter is again exploited to counteract this issue, but, since $\hat{\mathbf{h}}_A^s$ is not necessarily computed at the last stage of the IAR estimation process (as $\hat{b}_A$), the number of observations with which the filter is fed may vary. For this reason the predictive filter may be different. Further details on this prediction phase will be discussed in the next section.

Recalling Section 1.2.3, prior to communicate the necessary data to the aided agent A, the agent B needs to convert its position-related variables to a virtual-landmark-based version. Since the true steering vector $\mathbf{h}_B^s$ and the true range r_B^s are generally unknown to B, the operations that define the VL in Section 1.2.3 would be actually performed with estimated quantities, resulting in

$$\hat{\mathbf{r}}^s_{\tilde{B}} = \hat{r}^s_B \cdot \hat{\mathbf{h}}^s_B + \delta\underline{\mathbf{x}}_{B\to\tilde{B}} \tag{2.27}$$

$$\hat{r}^s_{\tilde{B}} = ||\hat{\mathbf{r}}^s_{\tilde{B}}|| \tag{2.28}$$

$$\hat{\mathbf{h}}^s_{\tilde{B}} = \frac{\hat{\mathbf{r}}^s_{\tilde{B}}}{\hat{r}^s_{\tilde{B}}} \tag{2.29}$$

where the notation $\hat{\mathbf{r}}^s_i$ represents the estimated corrected pseudorange in vector form.

Summarizing, the quantity provided by the IAR method is an estimate of (1.29), ultimately computed after the estimations of $r^s_A, r^s_{\tilde{B}}, \mathbf{h}^s_A, \mathbf{h}^s_{\tilde{B}}$ through

$$\hat{I}^s_{A\tilde{B}} = \sqrt{(\hat{r}^s_A)^2 + (\hat{r}^s_{\tilde{B}})^2 - 2\hat{r}^s_A\hat{r}^s_{\tilde{B}}cos(\hat{\gamma})} \tag{2.30}$$

$$\hat{\gamma} = cos^{-1}(\hat{\mathbf{h}}^s_A\hat{\mathbf{h}}^{s\top}_{\tilde{B}})\ . \tag{2.31}$$

2.3 A Priori Estimation and Collaborative Algorithm

In Sections 1.2 and 2.2, the IAR has been presented without showing the time dependence of the variables involved. Basically, each variable has been retrieved regardless of the communication latency, as if everything took place instantaneously. In order to provide a precise picture of the IAR algorithm, the implicit assumption of instantaneous communication maintained so far is removed, and the variables involved may now be related to distinct time instants. For this reason, a discrete time index k is often added to variables notation, indicating the time-dependency. In particular, k indicates the receiver's fixing epoch (Sec. 1.1) at which operations take place, consistently with the GNSS receiver's update rate of the position (i.e. the granularity of fixing epochs).

If we set the fixing epoch k at which the IAR is retrieved and integrated in the PVT, the time instants involved in IAR estimation procedure are essentially three:

- an initial time $k - RTT$, at which the agent A request aid;
- a time $k - \tau_2$, at which the agent B receives the request, processes the necessary data and sends them back to A;
- a time k, at which A receives the response message from B and performs the hybrid PVT.

Within this timeline the computational delay is neglected and the Round-Trip time (RTT) of the communication channel is the network parameter that drives the overall algorithmic delay. Hence, time delays are defined such that

$$RTT = \tau_1 + \tau_2\ , \tag{2.32}$$

where τ_1 is the time elapsed from the transmission of the help request to the reception of the latter and τ_2 is the time interval between the communication of B's response and its reception by A.

However, to be consistent with the discrete-time notation, the delays τ_1, τ_2 and RTT are assumed integers and defined in order to be a measure of fixing epochs elapsed. In other words, they are equal to the real continuous-time delay that they describe divided by the interval between two fixing epochs (the update interval) and rounded up to the next integer. If for example the real round-trip time is lower than the update interval, let's say 0.5 s, $k - RTT$ refers to the previous fixing epoch $k - 1$. In this way $\hat{\mathbf{x}}_{k-1}$ indicates the last position update available 0.5 s before the instant k, which is the most recent position information available at that time. As a matter of fact, the main objective in the definition of a suitable procedure, is to output a IAR estimate that involves the most up-to-date state estimations, while preventing agent's position from being openly shared.

Another important constraint is to have consistent ranges. This means that the vectors involved in the Carnot theorem, on which IAR formula is based, must form a triangle, as reproduced in Figure 1.1. This geometric structure must hold even considering a dynamic environment where vectors change continuously. Figure 2.1 allows a better understanding of the concept, while extending the static scenario of Figure 1.1.

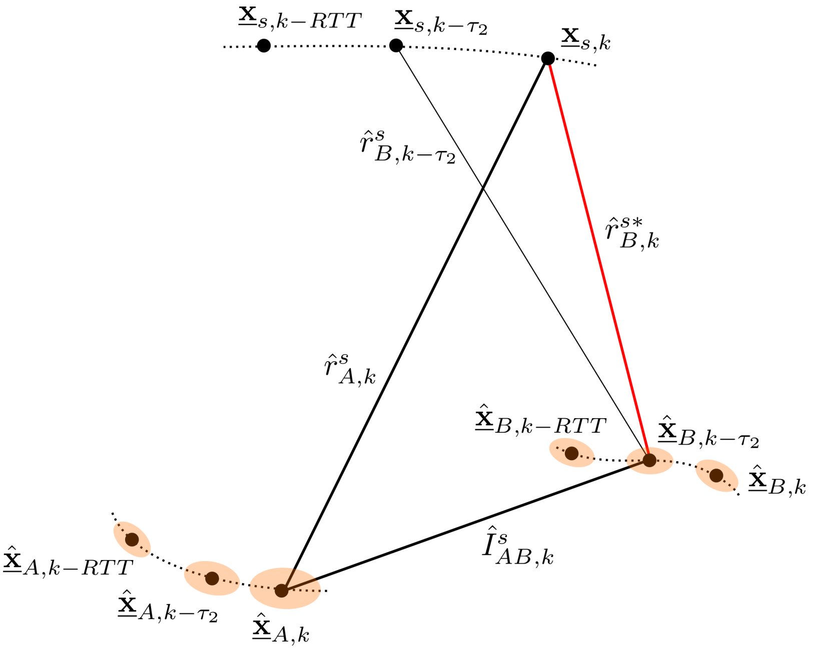

Figure 2.1: IAR estimation in a dynamic scenario. The ranges involved in the computation should be consistent.

In Figure 2.1, the position of the three items involved (aided agent A, satellite s and aiding agent B) is shown at the three fundamental time instants ($k - RTT$, $k - \tau_2$ and k). The IAR will be computed at time k, when the most recent pseudorange measured by A can be exploited to obtain $\hat{r}^{s}_{A,k}$, that will be used in equation (2.30). However, for what concern data from B, the most recent information available for A at time k is τ_2 seconds old, because the communication delay cannot be bypassed. The problem is that these two edges are not connected through a triangle, and this leads to an inconsistent result of the Carnot theorem.

To mitigate this problem, agent B has to predict a range that refers to the future satellite position $\underline{\mathbf{x}}_{s,k}$, starting from its current estimated range $\hat{\mathbf{r}}^{s}_{B,k-\tau_2}$. The orbital data of s are known from the demodulation of navigation message, hence the forecast of $\underline{\mathbf{x}}_{s,k}$ is not an issue. An estimation of $\underline{\mathbf{x}}_{B,k}$ would require instead a blind prediction, but it is easily avoided by considering an *inter-epoch* range as a consistent edge of the Carnot's triangle, computed w.r.t. $\underline{\mathbf{x}}_{B,k-\tau_2}$ and $\underline{\mathbf{x}}_{s,k}$ such that:

$$\hat{\mathbf{r}}^{s*}_{B,k} = \hat{\mathbf{r}}^{s}_{B,k-\tau_2} + (\underline{\mathbf{x}}_{s,k} - \underline{\mathbf{x}}_{s,k-\tau_2}) \tag{2.33}$$

$$\hat{r}^{s*}_{B,k} = ||\hat{\mathbf{r}}^{s*}_{B,k}|| \ . \tag{2.34}$$

The definition of (2.34) allows the computation of a baseline (IAR) between $\underline{\mathbf{x}}_{B,k-\tau_2}$, the position of B when shares its data, and $\underline{\mathbf{x}}_{A,k}$, the position of A when hybrid PVT is accomplished (Figure 2.1). It has to be reminded however, that B computes its virtual landmark $\underline{\mathbf{x}}_{\tilde{B},k-\tau_2}$ and uses it in place of its real position in the above computation, but the considerations done so far hold anyway.

In view of the above characterization on the communication delay involved in the IAR algorithm, some of the previous definitions of this chapter must be revised in order to include a consistent time index and get rid of the instantaneous communication assumption. In particular, the estimated IAR formula (2.30) is now written as

$$\hat{I}^{s}_{A\tilde{B},k} = \sqrt{(\hat{r}^{s}_{A,k})^2 + (\hat{r}^{s*}_{\tilde{B},k})^2 - 2\hat{r}^{s}_{A,k}\hat{r}^{s*}_{\tilde{B},k}cos(\hat{\gamma})} \tag{2.35}$$

where

$$\hat{\gamma} = cos^{-1}(\hat{\mathbf{h}}^{s}_{A,k} \cdot \hat{\mathbf{h}}^{s*}_{\tilde{B},k}) \ . \tag{2.36}$$

and it integrates the inter-epoch range and the respective steering vector. The above formula is reported just for completeness, but, in the rest of the dissertation, $\hat{r}^{s*}_{\tilde{B},k}$ and $\hat{\mathbf{h}}^{s*}_{\tilde{B},k}$ will be simply referred to as $\hat{r}^{s}_{\tilde{B},k}$ and $\hat{\mathbf{h}}^{s}_{\tilde{B},k}$, as they would be a regular range and its steering vector, in order to avoid additional notation complexity.

The block diagram in Figure 2.2 provides a compact illustration of the cooperative positioning algorithm adopted by the aided agent A. This high-level representation allows to summarize the process, highlighting the variables involved. In order to obtain the cooperative range $\hat{I}^{s}_{AB}$, the aided agent needs an estimate of the variables involved in (1.32). The variables $\hat{\mathbf{h}}^{s}_{A,k}$ and $\hat{r}^{s}_{A,k}$ have been retrieved through a predictive stage based on the position estimate of A (feedback). The predictive stage may also take advantage of current pseudorange measurements $\rho_{A,k}$ to provide the variables. The other two quantities necessary to accomplish the IAR computation are $\hat{\mathbf{h}}^{s}_{B,k}$ and $\hat{r}^{s}_{B,k}$. They are provided by the aiding peer B and are available to A after some delay (τ_2). Finally the aided peer integrates the additional range $\hat{I}^{s}_{AB}$ and the pseudoranges available at time k, in a hybrid PVT stage (that exploits an EKF to perform a GNSS/IAR tight-integration). Notice that also the non-cooperative PVT stage of agent B is based on an EKF routine.

In the next sections, the predictive stage block is discussed in details and the predictive filters inside it are presented. The choice of the filters is tightly related to constraints arisen from the premature estimation of $\mathbf{h}^{s}_{A}$ and b_A, that will eventually lead to two different implementations of the predictive stage and consequently to two versions of the cooperative algorithm for retrieve $\hat{I}^{s}_{AB}$.

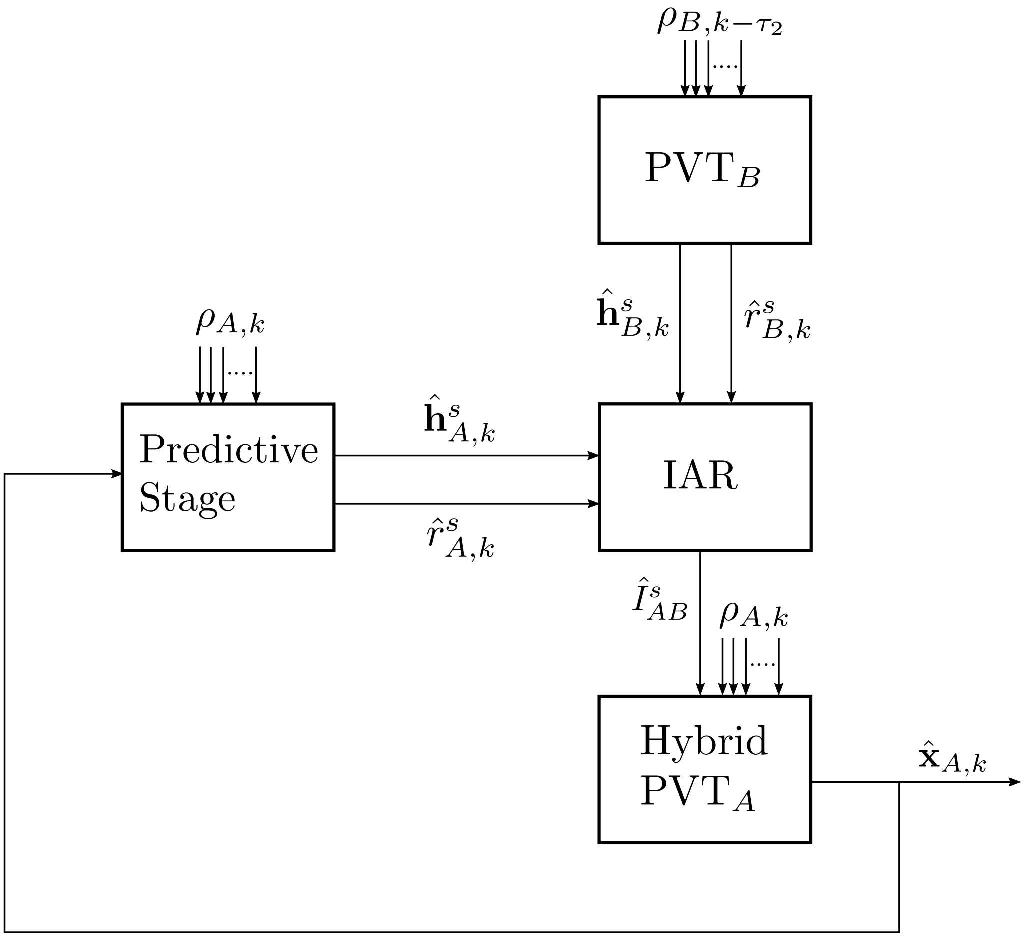

Figure 2.2: High level block diagram representation. Variables involved in IAR estimation are highlighted. The "PVT blocks" incorporate the feedbacks explicitly showed in Figure 2.3 and 2.4. The feedback from PVT stage and prediction stage is left visible at this level of representation.

2.3.1 KF A Priori Estimation

As mentioned, a key point is the estimation of $\mathbf{h}^s_A$. In the algorithm proposed in [13], and revised in Table 1, A sends an help request that includes the steering vector over which the angle computation ($\hat{\gamma}$) performed by B will be based.

This steering vector $\hat{\mathbf{h}}^s_A$ is generated at time $k - RTT$, thus it is estimated through the information available at that time. In particular, the estimation has to approximate the position that A will have at time k. Basically A has to foresee 1 RTT ahead to estimate the steering vector and it does not have the possibility to exploit future pseudorange measurements to obtain the steering vector orientation at time k. This predictive operation is thus accomplished only through the propagation of motion dynamics, according to (2.3).

This kind of estimation, that does not take advantage of state observations, will be referred to as *a priori estimation* (AP), in a way consistent with Kalman filter's terminology.

Algorithm 1 IAR Collaborative Algorithm with a priori estimation.

```
Time $k - RTT$: the aided agent $A$ broadcasts to the potential aiding agent $B$ its $\hat{\mathbf{h}}^s_A$
    based on the KF-prediction for time $k$
Time $k - \tau_2$: $B$ receives the request and generates a virtual landmark $\tilde{B}$
$B$ computes its inter-epoch steering vector $\hat{\mathbf{h}}^s_{\tilde{B}}$ w.r.t. $\tilde{B}$
$B$ computes $\hat{\gamma}$ using its inter-epoch steering vector $\hat{\mathbf{h}}^s_{\tilde{B}}$ and the one received by $A$
$B$ replies to $A$ sending $\hat{\gamma}$, $\hat{r}^s_{\tilde{B}}$ and $\underline{\mathbf{x}}_{\tilde{B}}$
Time $k$: $A$ receives the response and measures the pseudorange $\rho^s_A$ w.r.t. shared
    satellite $s$
$A$ estimates $\hat{b}_A$ using EKF fed by available pseudoranges and computes $\hat{r}^s_A$
$A$ estimates $I^s_{A\tilde{B}}$ using $\hat{r}^s_A$, $\hat{r}^s_{\tilde{B}}$ and $\hat{\gamma}$
$A$ obtain its position state $\hat{\mathbf{x}}_A$ through the EKF hybrid positioning routine
```

The predictive filter considered in this procedure is a plain Kalman filter (configured to work with no input measurements). In fact, since the estimation of $\hat{\mathbf{h}}^s_A$ is performed without observations, a linearization of the measurement model equation (2.6) is not necessary and the use of EKF would be redundant.

According to Algorithm 1, the agent A computes $\hat{r}^s_A$ in the last phase of the algorithm, when the angle $\hat{\gamma}$ has been already received from B. In this phase it is possible to exploit the available pseudorange measurements to obtain a better estimate of b_A and consequently a more reliable $\hat{r}^s_A$, according to (2.25). Measurements integration is generally convenient, when possible, even though the aided agent experiences reduced visibility and a small number of pseudoranges available. However, in order to integrate pseudoranges in b_A estimation, an EKF must be employed also in this phase.

Therefore the predictive stage in Figure 2.2 is composed by two filters: a plain KF that predicts $\hat{\mathbf{h}}^s_A$ without measurement observations and an EKF that provides $\hat{b}_A$. The block diagram in Figure 2.3 illustrates the roles of such filters (indicated as KF$_{AP}$ and EKF$_{QAP}$) in the computation of states and cooperative ranges, for this version of the algorithm. The scheme focuses on time occurrence and filter relationships. Variables involved in IAR estimation are highlighted as outputs from the predictive stage and from a *IAR variables extrapolation block* that simply extracts $\hat{\mathbf{h}}^s_B$ and $\hat{r}^s_B$ from the position estimate provided by the EKF. The four estimates can be then processed in the IAR estimation block at time k, that consequently feeds the PVT stage of agent A. Feedbacks are also depicted since, as it will be shown in Section 2.4, they play a key role in the performance of IAR.

This strategy has some disadvantages due to the prediction effort required and the absence of measurements in the steering vector prediction phase, but it is a more transparent approach. In fact, by assigning to B the burden of γ calculation, A is forced to share some information about its position: the steering vector $\hat{\mathbf{h}}^s_{A,k}$. The knowledge of its steering vector places A on an *ambiguity line*[11] that passes through $\underline{\mathbf{x}}_{s,k}$ (Figure 2.1). In a network of peers this information could be an evidence of trustworthiness, especially in large ad hoc networks, where identity and data validation may be an issue.

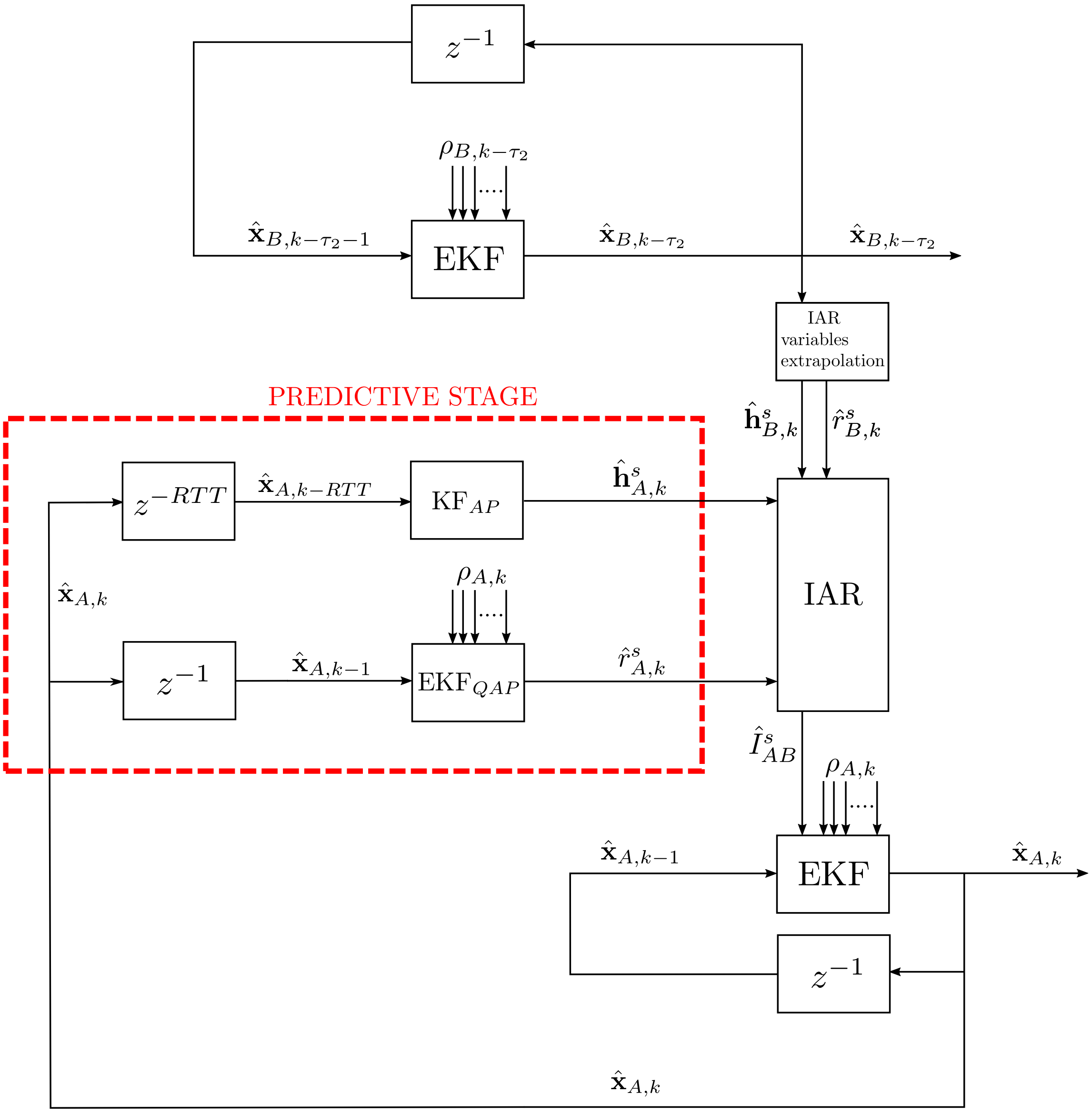

Figure 2.3: Algorithm 1 block diagram. The dashed rectangle highlights the predictive stages, where KF_{AP} is the Kalman Filter a priori estimation and EKF_{QAP} is the EKF quasi-a-priori estimation.

2.3.2 EKF Quasi-a-priori Estimation

The other possible strategy privileges the use of the most recent information. The set of IAR calculations is ultimately performed at instant k, when updated measurements can be exploited to derive the steering vector $\hat{\mathbf{h}}^s_A$, instead of predicting such steering vector 1 RTT early.

To accomplish this improvement, the collaborative algorithm must be revised in order to let the agent A to compute the angle $\hat{\gamma}$ in the final phase of the procedure. As a consequence, B have to share its steering vector on the communication channel, leaving to the aiding agent A all the computational burden. The privacy of B is still preserved due to the Virtual Landmark mechanism. But the information provided by B is still subjected to aging, since the communication delay τ_2 cannot be bypassed. In this view, A is not required to share anything, and can simply broadcast an help request over the network. The steps involved are summarized in Algorithm 2.

Algorithm 2 IAR Collaborative Algorithm with quasi-a-priori estimation.

```
Time $k - RTT$: the aided agent $A$ broadcasts to the potential aiding agent $B$ a help request
Time $k - \tau_2$: $B$ receives the request and generates a virtual landmark $\tilde{B}$
$B$ computes its inter-epoch steering vector $\hat{\mathbf{h}}^s_{\tilde{B}}$ w.r.t. $\tilde{B}$
$B$ replies to $A$ sending $\hat{\mathbf{h}}^s_{\tilde{B}}$, $\hat{r}^s_{\tilde{B}}$ and $\underline{\mathbf{x}}_{\tilde{B}}$
Time $k$: $A$ receives the response and measures the pseudorange $\rho^s_A$ w.r.t. shared satellite $s$
$A$ estimates $\hat{b}_A$ using EKF fed by available pseudoranges and computes $\hat{r}^s_A$
$A$ estimates $\hat{\mathbf{h}}^s_A$ using EKF fed by available pseudoranges and computes $\hat{\gamma}$
$A$ estimates $I^s_{A\tilde{B}}$ using $\hat{r}^s_A$, $\hat{r}^s_{\tilde{B}}$ and $\hat{\gamma}$
$A$ obtain its position state $\hat{\mathbf{x}}_A$ through the EKF hybrid positioning routine
```

Within this strategy, the estimation of $\mathbf{h}^s_{A,k}$ is derived from a preliminary estimated position $\hat{\underline{\mathbf{x}}}_A$, performed using the observations available at the current time k and not simply propagating the motion of the agent for the duration of a RTT. Since A needs to be aided, the number of available measurements is not sufficient for the convergence of a single point positioning algorithm. An EKF, however, is able to provide a state estimation even with a reduced set of observations, and consistently with the non-linear relation between measurements and state.

An EKF is therefore also employed at this stage, prior to the hybrid PVT (based on EKF as well), to provide the variables $\hat{\mathbf{h}}^s_A$ and $\hat{r}^s_A$ necessary for IAR estimation. As a consequence, according to this version of the algorithm, the predictive stage block of the high-level scheme in Figure 2.2 contains only an EKF (Figure 2.4), used as predictive filter in the sense that it works with a reduced number of observations. This kind of estimation that integrates measurement is usually called "a posteriori" in the Kalman filter's theory. In this text, the operations performed by the EKF employed in the predictive stage will be referred to as *quasi-a-priori estimation* (QAP), with a small abuse of terminology. This notation is used to distinguish this EKF, preliminary to IAR computation (EKF$_{QAP}$), from the successive hybrid EKF estimation (within the Hybrid PVT$_A$ block in Figure 2.2), that is performed with an enhanced number of measurements (pseudoranges and IARs) to provide the definitive position.

The block diagram in Figure 2.4 clarifies the roles of filters in IAR retrieval and position estimation for this algorithmic approach. Comparing block diagrams of Figures 2.3 and 2.4, it should be remarked that the preventive estimation of b_A (hidden inside $\hat{r}^s_A$) is computed at time k in both versions of the algorithm (Algorithm 1 and 2), when its estimation

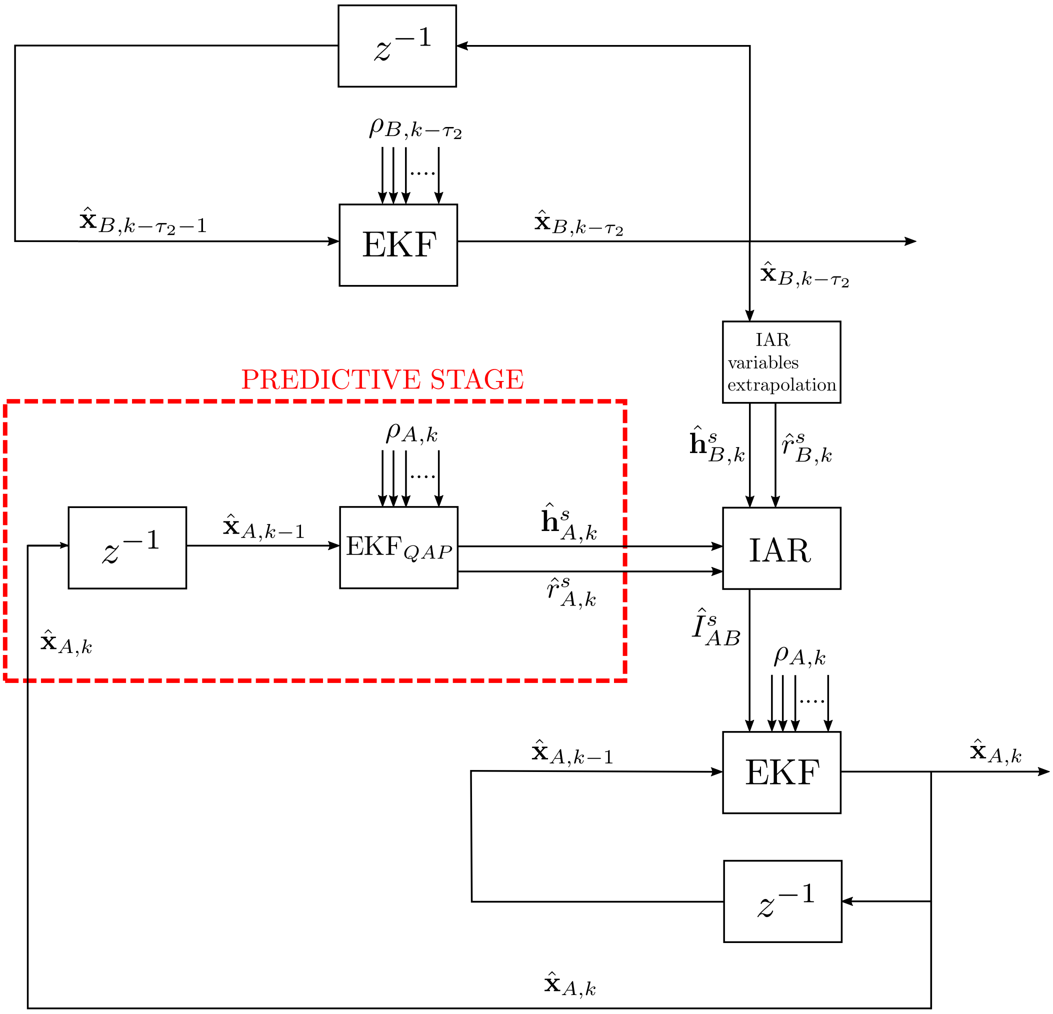

Figure 2.4: Algorithm 2 block diagram. The dashed rectangle highlights the a priori estimation block, where EKF_{QAP} is the EKF quasi-a-priori estimation stage.

can be performed exploiting updated pseudoranges (measured at time k). Hence, since it is computed integrating measurements, $\hat{b}_A$ is the output of an EKF_{QAP} block in both diagrams.

The use of EKF in the estimation of the steering vector $\mathbf{h}^s_A$ allows a general enhancement of its quality, provided that the measurements employed are valuable. Besides this, the main difference with respect to Algorithm 1, is that here A broadcasts a help message without sharing its steering vector information ($\hat{\mathbf{h}}^s_A$), since the computation of $\hat{\gamma}$ is not performed by B (Algorithm 2). As a consequence, the potential aiding agents will have to grant additional ranges in response to a bare help request. As it will be illustrated in Chapter 2.4, the advantages of an estimation that integrates observations are significant. On the other hand, the prediction effort required in an implementation of Algorithm 1 is 1 RTT and such a time interval could be very brief. If modern communication systems are considered, like the upcoming 5G [23], the round-trip latency addressed is around 1 ms [24]. This low-latency feature is also particularly relevant if the RTT is compared to common GNSS receiver update rates of 1 Hz [17].

This part on the a priori estimations completes an extensive description on the methodology that concerns the IAR paradigm. It has been underlined, in particular, that the quantities related to the aided agent represent a critical point, due to the necessity of an estimation in a condition of insufficient data. As a consequence, these estimations require ad hoc predictive procedures that involve measurements observation and feedbacks. Such techniques could potentially lead to divergent outputs, and the stability of the EKF is put to the test. For these reasons, their effects on the IAR measure need to be investigated carefully.

In the upcoming section, this study is carried out through a careful analysis. The impact of the aforementioned methods on the collaborative range is observed and, moreover, each single component of IAR estimation formula is analyzed w.r.t. to its effects on the IAR measure.

2.4 Inter-Agent Range Analysis

In the attempt of a deep understanding of the estimated IAR behavior, a look at the quantities that are involved in its estimation is mandatory. In this section the estimated IAR formula is taken apart and the impact of its components on the collaborative range is analyzed from a statistical point of view.

The quantities to be investigated have been carefully described in previous sections. However, even if the critical aspects have been individuated, the effects of their estimations' quality on the IAR have not been addressed yet. The high-level block diagram of Figure 2.2 provides a compact illustration of the variables involved. It will be kept as a reference throughout the section to have a clear picture of variables and their relationships, especially when they will be studied in separation.

The investigation on isolated effects of variables will be carried out focusing on one of the estimated quantities visible in Figure 2.2 and forcing the others to assume their true values. The analysis will be first focused on corrected pseudorange estimates $\hat{r}_A^s$ and $\hat{r}_B^s$, assessing the impact of pseudorange variance σ_{UERE} and the consequences of the user clock bias estimation. Then, steering vector estimation effects are inspected meticulously, either coming from the aiding agent ($\hat{\mathbf{h}}_B^s$) or from the aided agent ($\hat{\mathbf{h}}_A^s$). Ultimately, the combined effect of these estimations is presented and analyzed. It should be highlighted however, that generally, the superposition principle cannot be exploited due to the non-linearity of the system (e.g. IAR formula), but this still remains an effective method to take apart the IAR estimation process.

A few words should be spent on the analysis criteria. The quality of the estimated IAR is assessed by considering the difference w.r.t. a measure of the distance between A and B, namely the *IAR error*. It is considered as a reference in this sense the distance between the true position of agent B and the true position of agent A, since this quantity is the ideal IAR I_{AB}^s, as it would be obtained from an error-free set of parameters imposed in

(2.30). With this in mind, the IAR error is defined as

$$e_I = I_{AB}^s - \hat{I}_{AB}^s. \tag{2.37}$$

2.4.1 Pseudorange impact

Among the variables involved in IAR estimation, an obvious impact factor of a GNSS-based measure are the pseudoranges and their variance σ_{UERE}^2. Besides affecting the regular PVT solution, they are involved in IAR estimation formula since they are included in the definition of the estimated *corrected pseudoranges* $\hat{r}_A^s$ and $\hat{r}_B^s$. Recalling Section 2.2, $\hat{r}_i^s$ is obtained from pseudorange measurements:

$$\hat{r}_i^s = \rho_i^s - \hat{b}_i. \tag{2.38}$$

From (2.38) it can be noticed that the pseudorange ρ_i^s is not the only random quantity that affects the corrected pseudorange, in fact the estimated user clock bias affects $\hat{r}_i^s$ as well. As explained in Section 2.3, the user clock bias estimation is not straightforward, especially for the aided agent A, for which predictive techniques are needed. Therefore a specific analysis of its impact will be addressed in the next Section.

In order to simplify the problem a first analysis is done by considering a perfect estimation of the user clock bias, so that $\hat{b}_i = b_i$ for every agent. As stated in Section 1.1, the pseudorange error is modeled as a zero-mean normally distributed random variable such that

$$\rho_i^s \sim \mathcal{N}(r_i^s + b_i,\, \sigma_{UERE}^2). \tag{2.39}$$

In the case of an error-free estimation of the user clock bias, $\hat{r}_i^s$ is simply obtained with the addition of a deterministic value. As a consequence, the probability density function shape is unchanged, resulting in

$$\hat{r}_i^s = \tilde{r}_i^s \sim \mathcal{N}(r_i^s, \sigma_{UERE}^2) \tag{2.40}$$

where the variance is still σ_{UERE}^2. This simplification ensures that the estimated range $\hat{r}_i^s$ will depend on a single random variable i.e. the pseudorange error with its variance.

It is worth noticing that now the estimator $\hat{r}_i^s$ of the satellite-user distance is unbiased, since

$$\mathbf{E}[\hat{r}_i^s] = r_i^s. \tag{2.41}$$

With this assumption, the analysis of the pseudorange impact on $\hat{I}_{AB}^s$ can be carried out in a more rigorous way. The issues derived from clock estimation are avoided, in order to approach a study of the IAR independent from variables prediction. In fact, with respect to the diagram in Figure 2.2, the use of true user clock biases b_A and b_B in the corrected pseudoranges $\hat{r}_A^s$ and $\hat{r}_B^s$ results in a complete independence of these variables from respectively, the predictive stage and the PVT section of agent B.

Similarly, a perfect steering vectors estimation, such that $\hat{\mathbf{h}}_A^s = \mathbf{h}_A^s$ and $\hat{\mathbf{h}}_B^s = \mathbf{h}_B^s$, produces the same effect on the aforementioned diagram. With these ideal assumptions, a complete isolation of the effects provoked by σ_{UERE} on $I_{A,B}^s$ is addressed. These relations are summarized in the block diagram of Figure 2.5, which is a simplification of the scheme of Figure 2.2 that fits this idealized case.

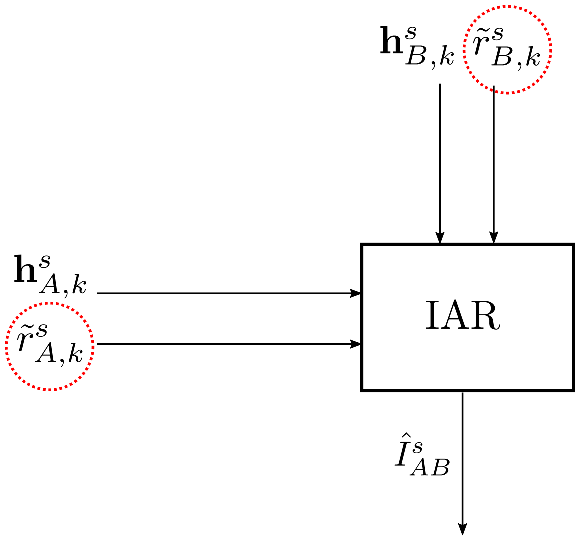

Figure 2.5: IAR estimation block diagram with isolated ρ effect. Variables involved in IAR estimation are highlighted, but $\hat{b}_A$, $\hat{b}_B$, $\hat{\mathbf{h}}^s_A$ and $\hat{\mathbf{h}}^s_B$ are assumed equal to their true values.

The characteristics of $\hat{I}^s_{AB}$ in this highly ideal situation are shown in Figure 2.6 through mean and standard deviation evolution of the IAR error e_I. The error is studied in comparison to the alterations of the variance of the pseudorange measurements σ^2_{UERE}. It is worth mentioning that σ^2_{UERE} characterizes the pseudorange noise of the entire swarm of agents: thus also contributions from aiding agents are affected by this variance.

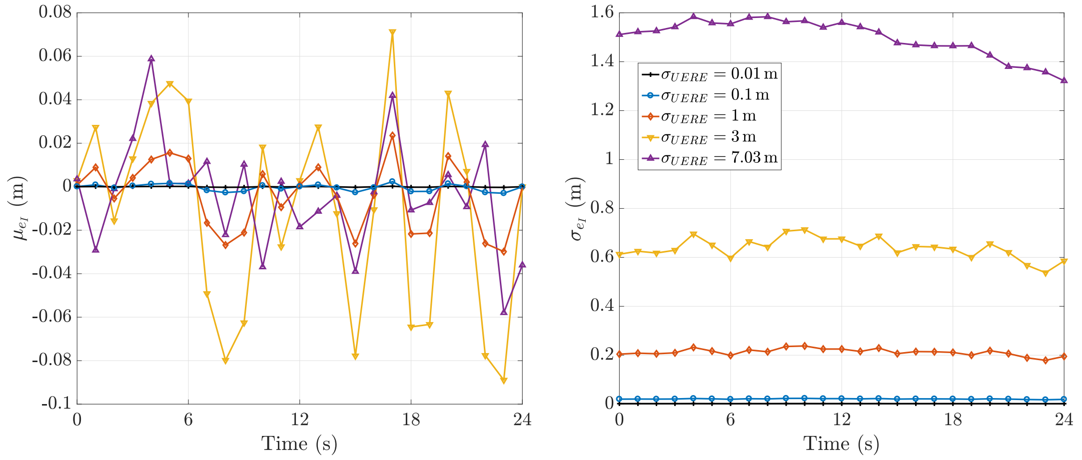

Figure 2.6: IAR error evolution. Mean and standard deviation w.r.t. different σ_{UERE} values. A perfect correction of the user clock bias in $\hat{r}^s_A$ is assumed as well as perfect steering vectors estimations.

The error statistic is coherent with the intensity of pseudorange noise. For bigger values of σ_{UERE} the mean error μ_{e_I} shows a wider dynamic. However, It must be noticed that all these curves highlight a very limited bias. The intensity of fluctuations is proportional to the amount of pseudorange noise involved in the IAR calculation, but the peaks have negligible values even for a realistic σ_{UERE} of 7.03 meters. In this favorable scenario the bias is close to zero, approaching the better performances demonstrated in [12] with static agents. This empirical result confirms also (2.41)

The standard deviation is consistent with the variations as well. For higher levels of pseudorange noise it is generally larger. Particularly, the initial values of the curves are already wide spread at the first instant of outage, since a strong σ_{UERE} directly affects the IAR calculation producing a larger uncertainty of this measure.

In this phase of the IAR analysis it may be interesting to inspect the probability distribution of $\hat{I}^s_{AB}$ as a random quantity. In fact, the pseudoranges are the only random variables involved in IAR estimation and the relative probability distribution represents a highly simplified case, useful for future comparisons. Figure 2.7 shows the outcome of a distribution fitting applied to IAR samples at the beginning of its evolution. The dataset is compared with several distributions[4] and the most suitable are plotted in order of fit. As a result, the normal distribution is the probability distribution that better describes the characteristics of the estimated IAR in this case.

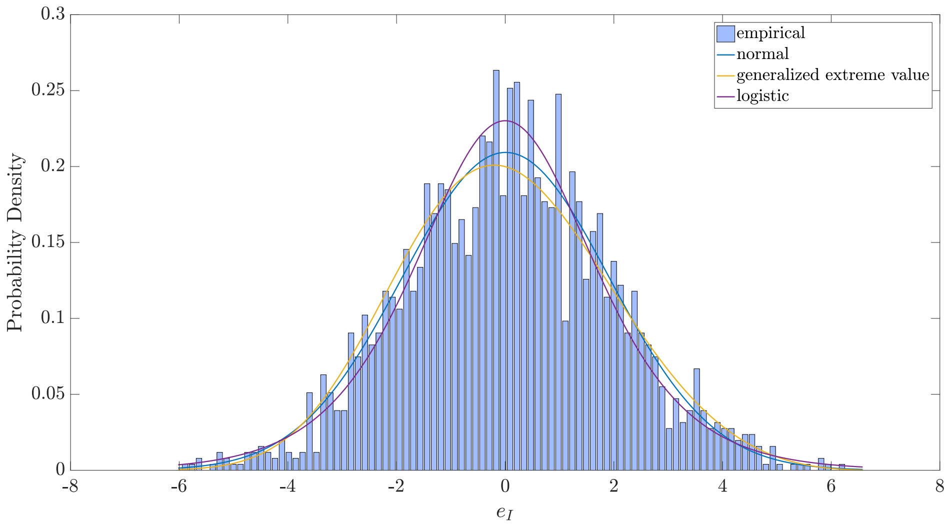

Figure 2.7: Probability distribution fitting on random variable $\hat{I}^s_{AB}$ at first instant. Pseudoranges are the only random variables involved in th estimation.

Summarizing, the variance of the pseudorange error is certainly a major factor influencing the standard deviation experienced by $\hat{I}^s_{AB}$. It is responsible for the intensity of the

---

[4] The continuous probability distributions tested are: beta, Birnbaum-Saunders, exponential, extreme value, gamma, generalized extreme value, generalized Pareto, inverse Gaussian, logistic, log-logistic, lognormal, Nakagami, normal, Rayleigh, Rician, t location-scale, Weibull

average fluctuations of $\hat{I}^s_{AB}$ around its true value I^s_{AB}, but it does not cause pronounced non-stationary phenomena by itself: the σ_{e_I} curves does not deteriorate as the outage time passes. In the same way, the average IAR error does not degenerate as well and moreover, it is always set around limited values. The pseudorange error variance alone σ^2_{UERE} is not responsible for biases enhancement of $\hat{I}^s_{AB}$ nor it is involved in variance divergence.

2.4.2 User Clock Bias estimation effect

The estimation of the user clock bias b_i is a critical aspect of this cooperative algorithm. According to (2.38), b_i is preliminary estimated to obtain the corrected pseudorange from the pseudorange measurement. In the previous section, this estimation was considered perfect, thus $\hat{b}_i = b_i$ was assumed. In this section instead, the non-ideal estimation of the user clock bias is introduced in $\hat{r}^s_i$ and its effect is specifically observed. The analysis is carried out again varying the σ_{UERE} intensity and assuming a perfect estimation of the steering vectors, in the tentative to observe the effects of $\hat{b}_i$ in isolation.

As underlined in Section 2.2, aided agent A and aiding agent B have to overcome different problems to obtain an estimate of b_i. While $\hat{b}_B$ is the result of a non-hybrid PVT algorithm, $\hat{b}_A$ cannot be retrieved through a plain GNSS PVT solution and has to be predicted (Sec. 2.3) using the available measurement observations. Due to this issue, the impact of the corrected pseudorange of agent A on IAR error is not straightforward.

The comparison with several levels of pseudorange noise discussed in the last section is here repeated and the results are summarized in Figure 2.8.

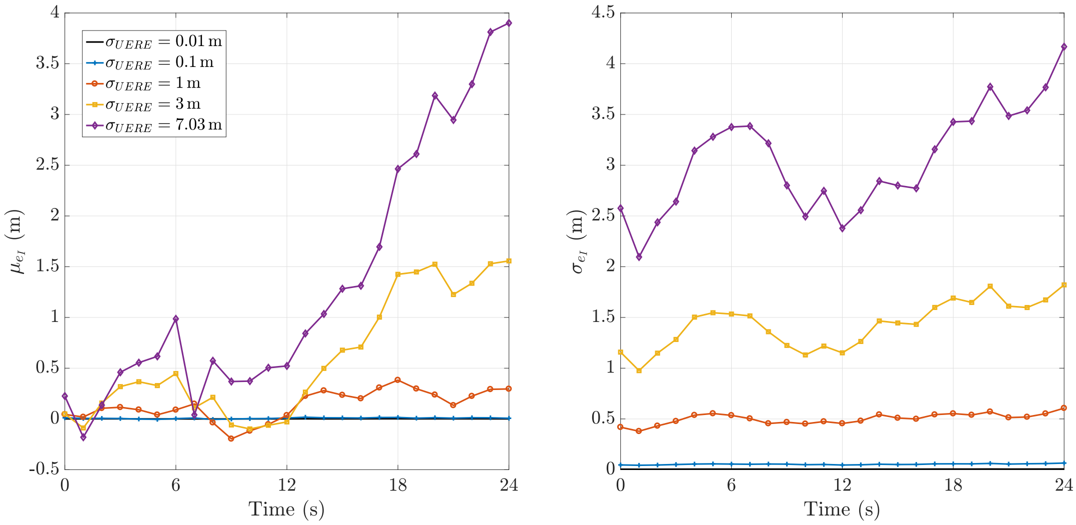

Figure 2.8: IAR error evolution during GNSS-outage. Mean and standard deviation w.r.t. different σ_{UERE} values.

With respect to Figure 2.6, where a perfect correction of the user clock bias in $\hat{r}^s_A$ was assumed, a fast worsening of the variance is clearly visible. The curves related to σ_{e_I} rapidly grow within the outage period. They show an increasing trend and, notably, the slope is proportional to the intensity of σ_{UERE}. A similar effect is produced also on the average IAR error, where the curves diverge proportionally to the intensity of pseudorange error variance as well.

The divergent behavior of error curves is not surprising. Figure 2.9 is an adaption to this case analysis of the more general high-level block diagram of Figure 2.2. Referring to this figure, it is possible to observe that the feedback that links the PVT$_A$ block with the prediction stage plays a crucial role in the arising of the divergent trend. Basically, the IAR estimation that enters in the aided agent's PVT block is based on the state estimation that this block has produced at previous instant. In other words, $\hat{I}^s_{AB}$, used to compute the state $\hat{\mathbf{x}}_{A,k}$, is calculated through $\hat{r}^s_{A,k}$ that is based on $\hat{b}_A$, which in turn is predicted from $\hat{\mathbf{x}}_{A,k-1}$.

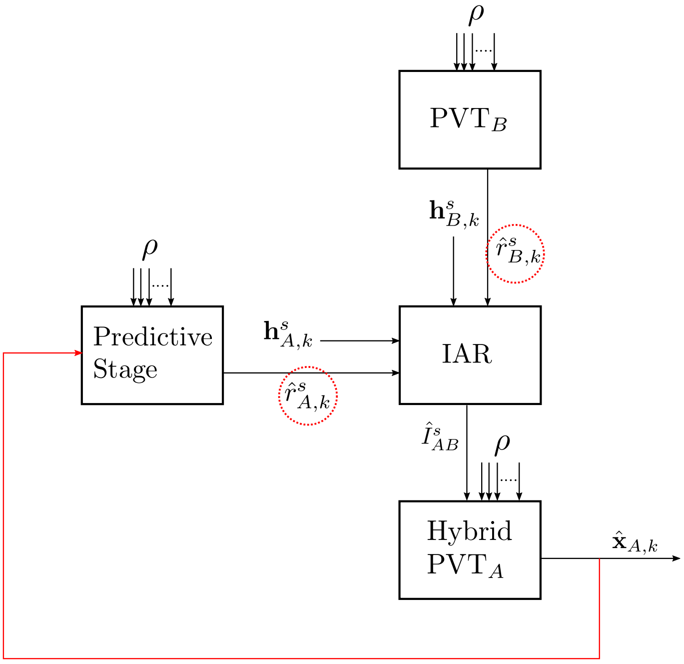

Figure 2.9: IAR estimation block diagram with isolated $\hat{b}_A$ and $\hat{b}_B$ effect. Variables involved in IAR estimation are highlighted, but $\hat{\mathbf{h}}^s_A$ and $\hat{\mathbf{h}}^s_B$ are assumed equal to their true values.

Through this closed loop, the state estimate re-enter (after processing) in the PVT block as an observation measurement. As a consequence, errors in $\hat{\mathbf{x}}_{A,k}$ are easily "amplified". Moreover, the pseudoranges affect the IAR estimation in two ways: directly in $\hat{r}^s_A$ equation 2.38 and indirectly through the estimation in the EKF$_{QAP}$ block of $\hat{b}_A$. The slope increase of curves in Figure 2.8 w.r.t. σ_{UERE} is therefore reasonable, since a poor pseudorange will be re-injected in the closed loop more than one time (Figure 2.9).

2.4.3 Steering Vector impact

In this section, the estimations of steering vectors $\mathbf{h}^s_A$ and $\mathbf{h}^s_B$ are investigated with respect to their influence on the range $\hat{I}^s_{AB}$. It is foreseeable at this point, that the two estimated quantities $\hat{\mathbf{h}}_A^s$ and $\hat{\mathbf{h}}_B^s$ will have very different characteristics, caused by their distinct estimation techniques (Sec. 2.2). In particular, $\hat{\mathbf{h}}_A^s$ can be estimated through two different methods (Sec. 2.3) that are compared in this section as well.

A precise characterization of the steering vectors effects demands an analysis where $\hat{\mathbf{h}}_i^s$ is the only random variable involved in IAR computation, besides measurement noise. For this reason, the effects of the user clock bias estimation are nullified, imposing $\hat{b}_i = b_i$ for all agents.

Furthermore, in order to specifically inspect the role of feedbacks in steering vectors' determination, a comparison with *random steering vectors* will be provided. The intent is to have steering vectors with arbitrary accuracy and precision, whose generation is also independent from past epochs. In this way it is possible to distinguish the response of the IAR estimation caused by an erroneous steering vector alone or by the presence of the re-injection of errors through feedback. Random steering vectors are obtained from a true position $\underline{\mathbf{x}}_{i,k}$ corrupted with white Gaussian noise. The resulting steering vector is therefore a time-independent noisy version of $\mathbf{h}_i^s$.

The following analyses are carried out differently w.r.t. to the agent considered. Since the determination of $\hat{\mathbf{h}}_B^s$ is the result of a plain non-hybrid PVT solution (Figure 2.2), a first simpler analysis is devoted to the influence of the aiding agent's steering vector on IAR. To this purpose, the interference of the aided agent's steering vector estimation is erased, i.e. $\hat{\mathbf{h}}_A^s = \mathbf{h}_A^s$ is assumed. Subsequently, the effects of the prediction of $\mathbf{h}_A^s$ alone are presented, studying both the a priori estimation procedures while assuming $\hat{\mathbf{h}}_B^s = \mathbf{h}_B^s$.

Aiding agent steering vector impact

As mentioned, the isolated effects of the steering vector $\hat{\mathbf{h}}_B^s$ on estimated IAR are assessed imposing perfect estimations of user clock biases and steering vector $\mathbf{h}_A^s$. These assumptions lead to the block diagram of Figure 2.10, where $\hat{\mathbf{h}}_B^s$ and ρ are the only random variables left. The quantity $\hat{\mathbf{h}}_B^s$ in particular, is influenced by the latter and by the state estimate of agent B obtained through the PVT stage.

In Figure 2.11 the statistical characteristics of the IAR process are reported in these idealized conditions.

The black curves are related to a steering vector estimation obtained from the EKF-based PVT solution of the aiding agent B. In the left plot, regarding the IAR average error μ_{e_I}, the curve exhibits a wide dynamic reaching non-negligible peaks of bias. The evolution of this bias however, suggests a bounded behavior that does not give birth to a divergent trend as the IAR estimation is reiterated through time. Similarly, the standard deviation σ_{e_I} evolves smoothly and settles around a constant value, that is coherent with the standard deviation associated to the pseudoranges involved ($\sigma_{UERE} = 7.03\,\mathrm{m}$).

From these curves, related to the $\hat{\mathbf{h}}_B^s$ derived from a EKF-based PVT, it can be noticed that both average and STD of the IAR error are slow varying function of time. This suggests the presence of time correlation in the process. Since in this case the PVT algorithm is based on EKF, this comes at no surprise.

In Figure 2.11, the IAR error is also compared to one computed through a $\hat{\mathbf{h}}_B^s$ vector derived from a PVT solution based on a Least Mean Square algorithm (LMS). In this case, the solution at each time is independent from the past and this is noticeable from a

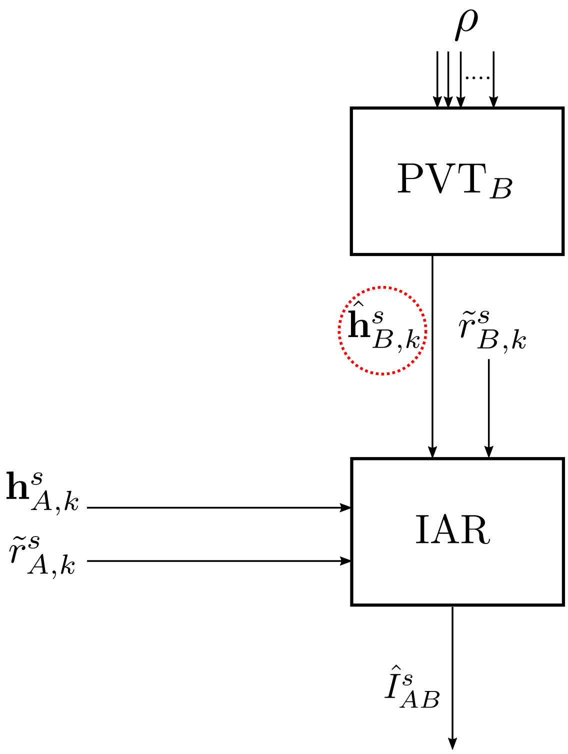

Figure 2.10: IAR estimation block diagram with isolated $\hat{\mathbf{h}}^s_B$ effect. Variables involved in IAR estimation are highlighted, but $\hat{\mathbf{h}}^s_A$, $\hat{b}_A$ and $\hat{b}_B$ are assumed equal to their true values.

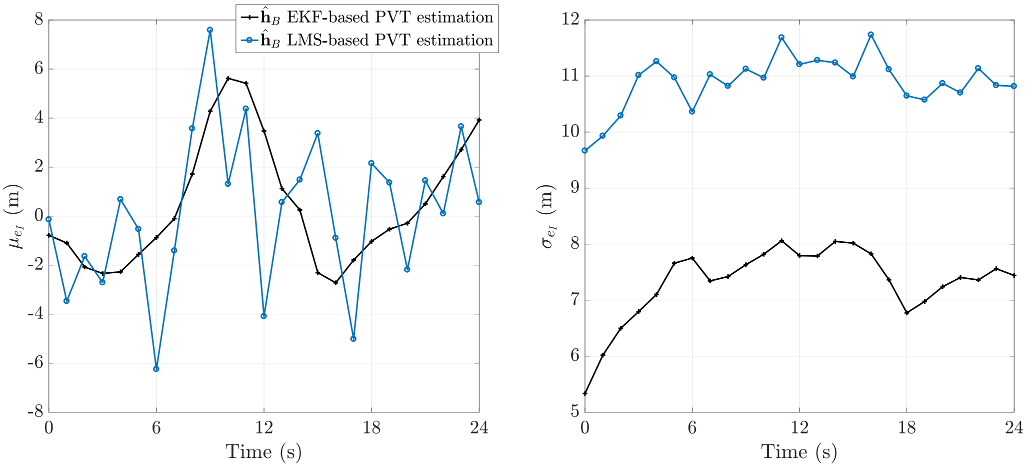

Figure 2.11: IAR mean and standard deviation through time. A steering vector obtained from a EKF-based PVT is compared to one obtained from a LMS-based PVT solution.

less smooth bias characterization. Moreover, σ_{e_I} settles to higher values w.r.t to the EKF counterpart, as it is expected by a LMS-based solution, provided that the Kalman's model assumptions are sufficiently accurate [25]. In this example, average and STD of e_I are consistent with the estimation characteristics of the aiding agent's position.

In order to further investigate the influence of agent B's position state estimation on IAR, the generation of random steering vectors is exploited. As mentioned, they are based on an exact position $\underline{\mathbf{x}}_{i,k}$ that has been corrupted with Gaussian noise. In particular, the true position is affected by the noise vector $\mathbf{w}_k$, according to

$$\underline{\mathbf{x}}_{i,k} + \mathbf{w}_k \sim \mathcal{N}(\boldsymbol{\mu}, \boldsymbol{\Sigma}), \tag{2.42}$$

where the mean vector μ is

$$\boldsymbol{\mu} = (\mu \quad \mu \quad \mu)^\top \tag{2.43}$$

and the covariance matrix $\boldsymbol{\Sigma}$ is

$$\boldsymbol{\Sigma} = \begin{pmatrix} \sigma^2 & 0 & 0 \\ 0 & \sigma^2 & 0 \\ 0 & 0 & \sigma^2 \end{pmatrix} . \tag{2.44}$$

The values μ and σ^2 are arbitrarily set in order to regulate the noise intensity and average. If $\mu = 0$ this technique produces an estimated steering vector that is unbiased, besides being characterized by a stationary error. The intent is to have an overview on the toleration of the IAR w.r.t. steering vectors received from an aiding peer with a poor position precision. Several position variances have been investigated and their effect on the IAR error is described by Figure 2.12 along with the case of $\hat{\mathbf{h}}_B^s$ derived from an EKF-based PVT solution.

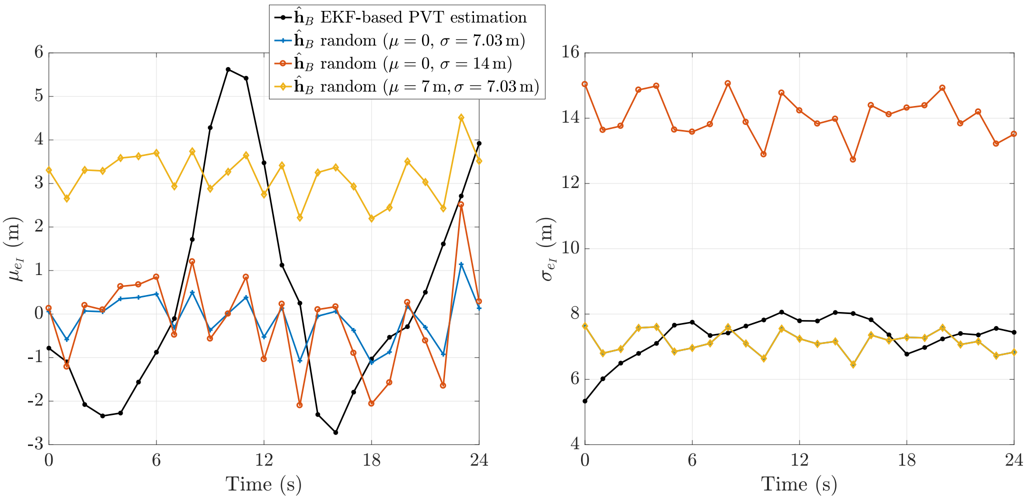

Figure 2.12: IAR mean and standard deviation through time. A steering vector obtained from a EKF-based PVT is compared to random $\hat{\mathbf{h}}_B^s$ with different values of σ and μ.

According to the plots, the steering vector estimated by B has generally a non-negligible effect on the cooperative range. When $\hat{\mathbf{h}}_B^s$ is random, the effects on the average IAR error are again coherent with the estimated position characteristics. The same happens to σ_{e_I}, which is substantially stationary, with values coherent with the standard deviation of the corrupted position over which a random steering vector is based. This position's error has also no time-correlation and the IAR error curve behaves consistently.

To complete the investigation on effects of a poor position estimate of the aiding agent on IAR, the comparison with a biased random steering vector $\hat{\mathbf{h}}_B^s$ is also provided. The result is outlined as well in Figure 2.12. As expected, the standard deviation is equal to the curve relative to the same random steering vector characteristics with no forced bias. The average error instead is clearly non-zero but the trend is constant. The statistical characteristics of the IAR error are again coherent with random steering vector's properties: this is a further confirmation that the IAR estimation error behave consistently with aiding agent accuracy and precision. Therefore as long as B does not obtain a poor position fix, the IAR is still a valuable measure of euclidean distance. In other words, the IAR error does not diverge when IAR estimation is fed by bounded position errors of the aiding agent.

This aspect foster a conservative choice of the aiding agent. Agent that are not experiencing outage and are able to position themselves with no external aiding are certainly a good choice. Furthermore in a crowded environment, a selection of collaborating peers may be done on this basis, with respect to collaborative peers' positioning quality (see Sec. 4.3).

Aided agent steering vector impact

A final investigation is devoted to the influence on IAR error of the steering vector estimated by A. As underlined throughout the chapter, this estimation must face a data underestimation problem, thus, similarly to the estimation of b_A, prediction techniques are required that may put to the test algorithm's stability.

In order to isolate the effects of $\hat{\mathbf{h}}_A^s$ on the Inter-Agent Range, it is assumed in this part a perfect estimation of $\hat{\mathbf{h}}_B^s$, $\hat{b}_A$ and $\hat{b}_B$. As a result, the dependencies highlighted in Figure 2.2 are reduced, resulting in the simplified block diagram of Figure 2.13, where $\hat{\mathbf{h}}_A^s$ and ρ are the only random variables.

The estimated steering vector $\hat{\mathbf{h}}_A^s$ is the outcome of a prediction step, weather it is an a priori KF prediction that looks 1 RTT forward or a quasi-a-priori EKF step updated with available pseudoranges (Section 2.3). The statistical characteristics of the IAR error resulting from the application of both methods are compared in Figure 2.14.

The two curves in the aforementioned figure share a distinctive divergent trend. A behavior similar to the one observed during the analysis devoted to effects of b_i estimation. At the beginning of observation time, both average and STD are characterized by small and similar values. But, as the IAR algorithm is reiterated, the IAR error gradually degrade.

In the previous analysis on aiding agent's influence, it has been observed that the estimation of $\mathbf{h}_B^s$ is not subject to the same instability issues that characterized the estimation of $\mathbf{h}_A^s$. The feedback that links the output of hybrid PVT to the IAR computation is the main difference between the two estimation procedures (highlighted in red in Figure 2.13). Hence it is likely the cause of the different statistical characteristics of the IAR error in the two analyses.

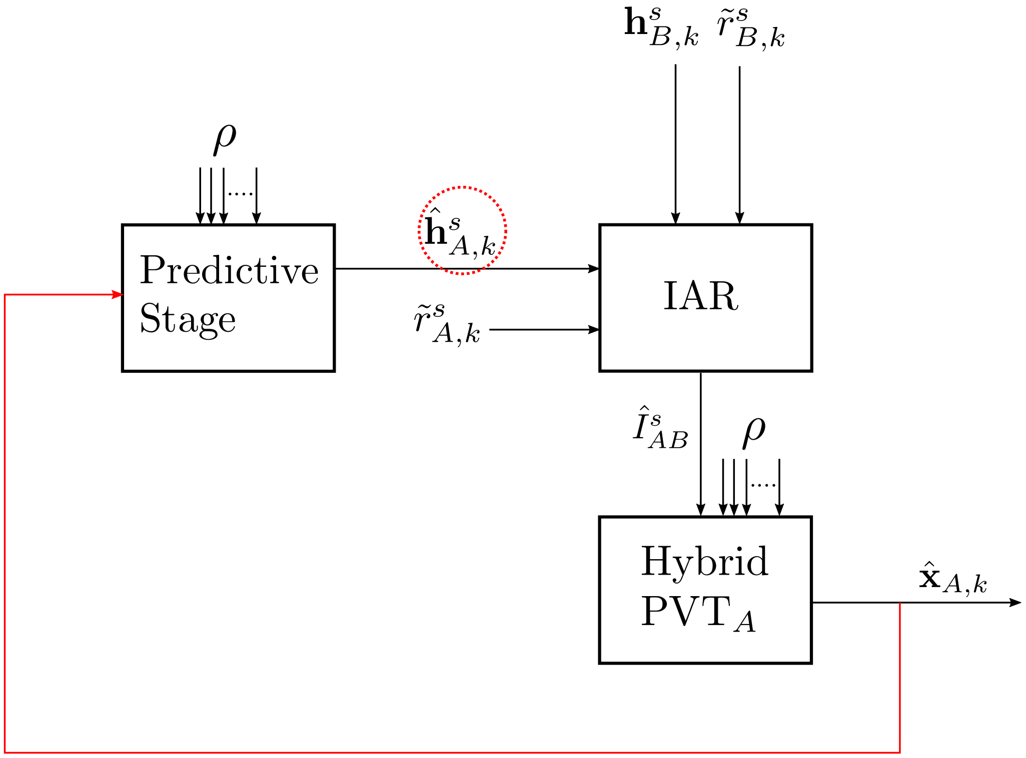

Figure 2.13: IAR estimation block diagram with isolated $\hat{\mathbf{h}}^s_A$ effect. Variables involved in IAR estimation are highlighted, but $\hat{\mathbf{h}}^s_B$, $\hat{b}_B$ and $\hat{b}_A$ are assumed equal to their true values.

To distinguish between the feedback response from the sole effects of an erroneous steering vector prediction, a comparison among IAR error caused by random steering vectors is provided (Figure 2.15). It is the same technique employed above, since the random steering vector's generation is based on noisy time-independent positions that emulates the absence of feedbacks.

Several considerations can be done regarding Figure 2.15. Focusing on random $\hat{\mathbf{h}}^s_A$, it is clear that such steering vectors impact the IAR error variance with intensity that depends on σ. Obviously a σ variation has almost no effect on IAR error bias since in this case $\mathbf{E}[\hat{\mathbf{h}}^s_A] = \mathbf{h}^s_A$ at any time instant. In any case a stationary variance of these steering vectors produces a IAR error whose statistical characteristics does not change over time. In fact, even a biased random steering vector (purple line) does not give birth to divergent phenomena, while affecting the μe_I. Random steering vectors provoke a IAR error whose average and STD are constants, with values consistent with their stationary characteristics. This confirms that the isolated use of erroneous steering vectors $\hat{\mathbf{h}}^s_A$ is not responsible of IAR error's divergence of any kind.

The comparison with the curves related to the two prediction methods of $\mathbf{h}^s_A$ in Figure 2.14 suggests that the unavoidable prediction of the steering vector is another major contributor to the growth of variance and bias in IAR estimation, causing a deterioration of the cooperative range. As illustrated in the analysis of $\hat{b}_i$, this is a reasonable aftermath of a priori estimation, since the latter introduce a feedback from a hybrid PVT (Figure 2.13).

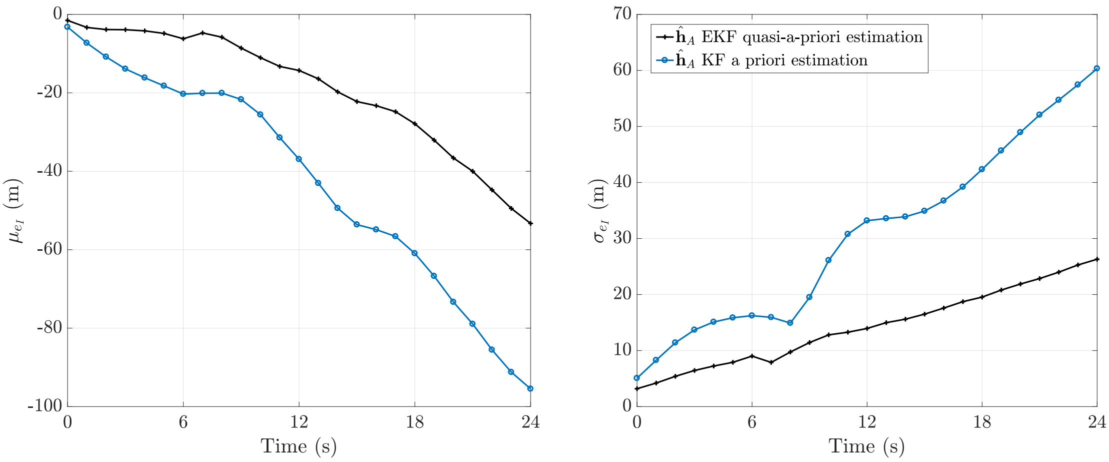

Figure 2.14: IAR mean and standard deviation through time. A steering vector obtained through a EKF-based quasi-a-priori estimation is compared to one predicted through a KF-based a priori estimation.

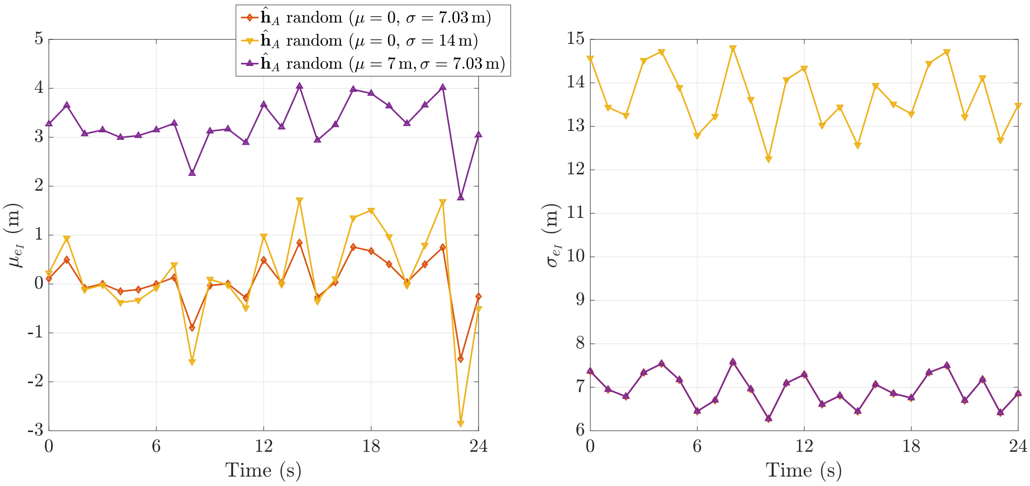

Figure 2.15: IAR mean and standard deviation through time. A steering vector obtained from a EKF-based PVT is compared to random $\hat{\mathbf{h}}_A^s$ with different values of σ and μ.

Errors in IAR estimation affect the PVT outcome which, in turn, influences the next IAR estimations propagating such errors in the closed loop. Due to the feedback's presence, the injection of erroneous estimated steering vectors in the IAR algorithm is amplified throughout the epochs and could potentially lead to instability issues. This phenomenon is more intense in the KF prediction case, where the prediction stage is heavily based on previous PVT outcomes, because no measurement observations are exploited to estimate $\hat{\mathbf{h}}_A^s$. As a result a more severe divergence can be observed.

2.4.4 Combined effect

To provide a complete statistical characterization of the IAR estimate, the evolution of $\hat{I}_{AB}^s$ should be studied in presence of the concurrent effects of all the parameters involved. The analysis of combined effects of all the variables previously described is presented in this part. Envisioning a realistic implementation, it represents a meaningful statistical characterization.

The assumptions made so far are removed and each quantity involved in IAR estimation formula is retrieved as described in the IAR procedure. In particular, user clock bias and steering vectors are estimated by aiding and aided agent as illustrated by the complete block diagram of Figure 2.2.

Figure 2.16 illustrates the evolution of the IAR error in this realistic condition, comparing different prediction methods of $\mathbf{h}_A^s$.

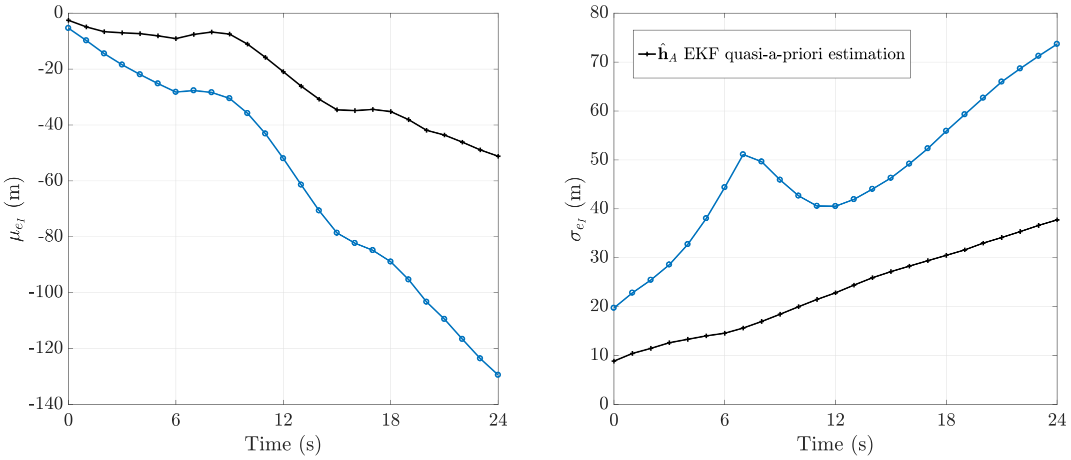

Figure 2.16: IAR error evolution through time. Mean and standard deviation w.r.t. different steering vector estimation methods. Realistic configuration with estimated steering vectors and user clock bias errors. $\sigma_{UERE} = 7.03\,\text{m}$.

From the figure, it is possible to recognize the contributions from some of the parameters investigated so far. Remember however that, as stated in the introduction of Section 2.4, the superposition principle cannot be exploited due to the non-linearity of the system. All previous components' estimations contribute to bias and variance levels in the IAR error, but the divergent trend of μe_I and σ_{e_I}, introduced by the estimations of $\mathbf{h}_A^s$ and b_A, dominates the overall behavior. The a priori estimations of both $\mathbf{h}_A^s$ and b_A are indeed responsible for this deterioration.

The combination of these two phenomena encourages the divergent trend of the curves as the outage period passes. As a result this process is faster than in previous configurations: the combined influence of the two parameters makes bias and STD worse in a briefer time.

It should be remarked however, that the deteriorations caused by the two predicted variables have not the same intensity. According to their isolated effects (Figure 2.14 and 2.8), bias and variance provoked by the user clock bias estimation are far less harmful than those caused by $\hat{\mathbf{h}}_A^s$, since their intensity is much smaller. Nevertheless, their combined effect may be worse than their sum since the superposition principle does not hold. This is reasonable because now, every time a poor position estimation is re-injected in the IAR computation through the feedback, its negative effect is repeatedly spread over more estimated variables ($\hat{\mathbf{h}}_A^s$ and $\hat{b}_A$).

In accordance to previous results, also in this realistic situation, the strength of the deterioration depends on the pseudorange error noise intensity, as suggested by the representation of Figure 2.17. This means that IAR errors are more biased and less concentrated as the time passes, and the worsen of these characteristics is faster when fed by pseudoranges characterized by a bigger σ_{UERE}.

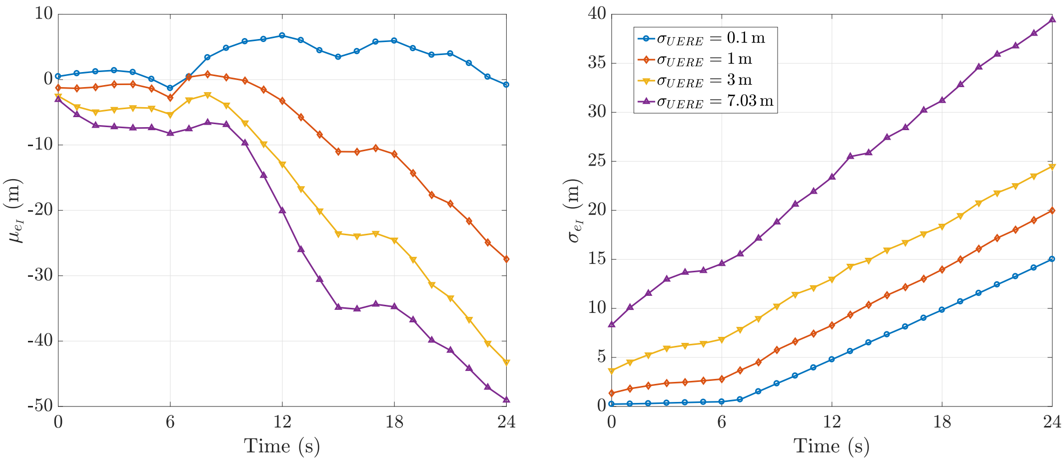

Figure 2.17: IAR error evolution through time. Mean and standard deviation w.r.t. different σ_{UERE} levels. The steering vector $\hat{\mathbf{h}}_A^s$ is obtained through EKF quasi-a-priori estimation.

It is interesting to notice that the bias is not nullified even in presence of a very small σ_{UERE} (0.1 m). This means that even small fluctuations around true pseudorange values are able to produce non-negligible effects, due to the wide impact that the measurement noise has over the system described by Figure 2.2. In particular, the average IAR error is mostly non-zero during its evolution, suggesting that

$$\mathbf{E}[\hat{I}_{AB}^s] \neq I_{AB}^s \tag{2.45}$$

for a generic time instant. Therefore, in general, the IAR method is a biased estimator of the euclidean distance between two receivers.

Now that all the estimated variables are included in the process, $\hat{I}^s_{AB}$ is a random variable dependent from several random quantities. The study of its probability distribution would complete the characterization of the statistical properties, but the derivation of an analytical form is certainly non-trivial. Such characterization is assessed in this part by means of an empirical approach.

A similar analysis was done in Section 2.4.1, where the gaussian distribution has been identified as the closest matching result of a distribution fitting algorithm. The result of Section 2.4.1 was derived in a highly-idealized situation, where the pseudorange noise affected the IAR process only through corrected pseudoranges $\hat{r}^s_i$ (Figure 2.5). With the current realistic assumptions instead, $\hat{I}^s_{AB}$ is the result of a complex interaction among variables affected by the pseudorange noise, and the outcome of a distribution fitting algorithm may be unexpected.

Figure 2.18 illustrates the output of this procedure when applied to samples of IAR error evaluated at the first instant of $\hat{I}^s_{AB}$ evolution[5]. The procedure is applied on IAR estimates obtained through the quasi-a-priori prediction method of $\mathbf{h}^s_A$. Mean and variance of the histogram in Figure 2.18 are therefore consistent with the ones read from Figure 2.16 at the first time instant. The closest distributions are shown in the figure legend in order of fit.

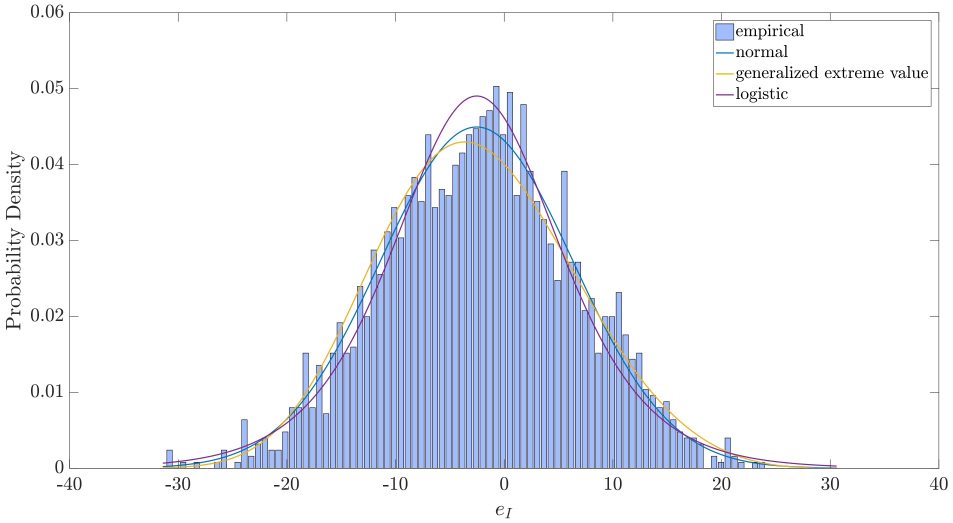

Figure 2.18: Probability distribution fitting on random variable $\hat{I}^s_{AB}$ at first instant. Realistic configuration with estimated steering vectors and user clock bias errors. The steering vector $\hat{\mathbf{h}}^s_A$ is obtained through EKF quasi-a-priori estimation.

The distribution with the highest matching is the same of the highly idealized case of Section 2.4.1, i.e. the Gaussian distribution. This is quite reasonable since a snapshot at

---

[5] As before, the continuous probability distributions tested are: beta, Birnbaum-Saunders, exponential, extreme value, gamma, generalized extreme value, generalized Pareto, inverse Gaussian, logistic, log-logistic, lognormal, Nakagami, normal, Rayleigh, Rician, t location-scale, Weibull

early instants of the algorithm repetitions provides a collaborative estimate that is free from effects induced by previous IAR estimation processes.

A different outcome of the fitting procedure may arise if the IAR error distribution is analyzed when more seconds (and more algorithm repetitions) are elapsed. Mean and variance are certainly expected to change, accordingly to values reported in Figure 2.16, but the distribution shape may not remain the same throughout time evolution. Figure 2.19 summarizes the outcomes of this distribution fitting algorithm, applied to the realizations of random variable $\hat{I}^s_{AB}$ when 24 seconds are elapsed. It is clear that the gaussian distribution is still the closest matching among the probability distributions tested. This is an essential result for the IAR measurement characterization.

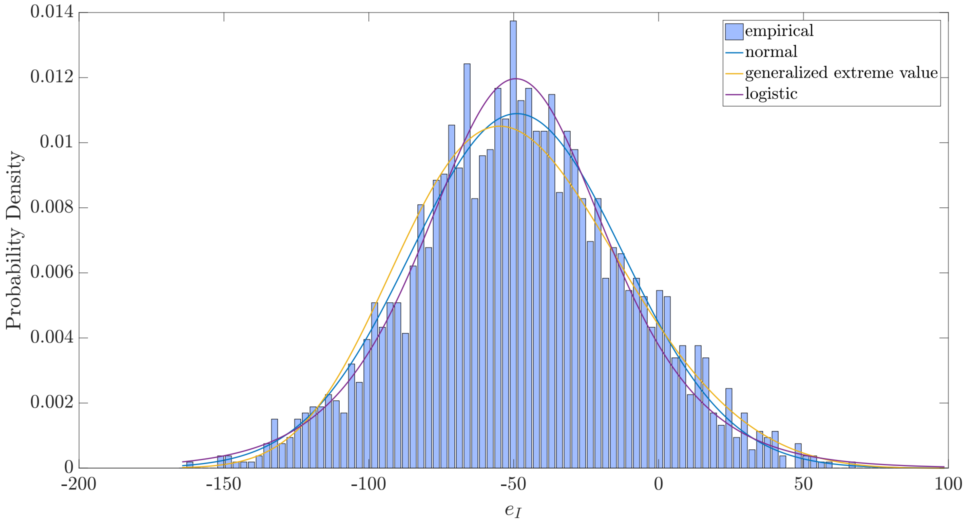

Figure 2.19: Probability distribution fitting on random variable $\hat{I}^s_{AB}$ after 24 epochs of IAR estimation processing. Realistic configuration with estimated steering vectors and user clock bias errors. The steering vector $\hat{\mathbf{h}}^s_A$ is obtained through EKF quasi-a-priori estimation.

In the EKF measurement model from Section 2.1 the measurement noise in (2.6) is assumed normally distributed. This is verified for the pseudoranges, but the vector $\mathbf{z}_k$ integrates also IAR collaborative measurements in this hybrid implementation of EKF. As a consequence, the gaussian noise assumption must be true also for IAR measurements. The covariance $\bar{\mathbf{R}}_k$ in fact, models their variances as well, and it is used in the EKF routine to provide an optimal estimate, as long as the model is true. With this in mind, the empirical result from the distribution fitting test represent a further confirmation that the EKF measurement model is still a suitable choice when integrating Inter-agent collaborative ranges. A further proof is given in Figure 2.20, where the fitting tests are performed at more time instants and the results are shown together to provide a general perspective on the evolution of the statistical properties through time.

From this extensive analysis of combined effect, it has been observed a significant worsening of the statistical properties of $\hat{I}^s_{AB}$. Precision and accuracy of the IAR estimate

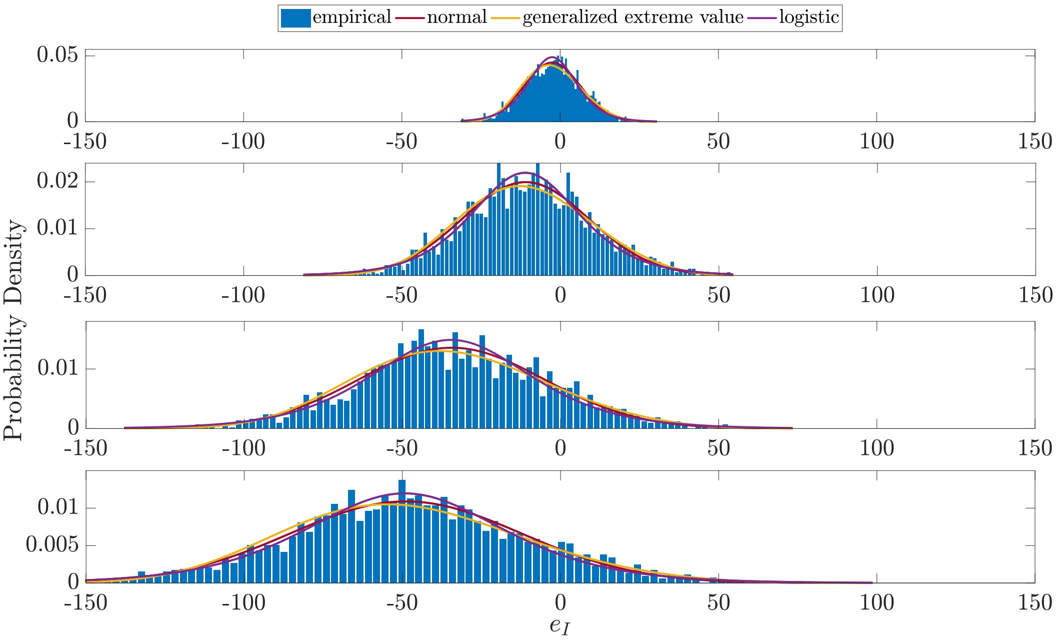

Figure 2.20: Probability density estimation of a single IAR measurement along an outage of 25 s. Snapshots obtained at 0 s, 9 s, 17 s and 25 s.

are not constant throughout the repetitions of the process but rather deteriorate progressively. As a consequence the statistical properties of $\hat{I}^s_{AB}$ are time-dependent: $\hat{I}^s_{AB}$ is a non-stationary process with properties related to the outage duration.

It should be reminded however, that this behavior arises after many repetitions of IAR algorithm, that would correspond to a long outage period experienced by an agent. Moreover the observation has been focused on the same Inter-agent range I^s_{AB}, that would not necessary be the only collaborative measurement integrated in the hybrid PVT of an aided agent. A generic aided agent A might be able to obtain several IAR measures, relative to various aided agents and common satellites. In a realistic implementation, this diversity is exploited by taking advantage from the integration of multiple collaborative ranges. This will result in preventing the same estimation errors that affect a specific IAR, from being continuously re-injected in the IAR estimation through feedback, thus producing the divergent phenomena observed so far.

2.5 Final Remarks

This chapter has provided a comprehensive description of the methodology concerning the IAR paradigm. Limits and constraints of the method has been discussed, along with procedures necessary to face them. In particular, the GNSS/IAR tight integration has been illustrated in its EKF implementation. The stability issues relative to the choice of the linearization point has been presented as well as the possibility of a LMS re-initialization of the EKF, possible thanks to the IAR integration, useful to neutralize divergent phenomena. Then, the IAR estimation procedure has been deeply discussed, presenting the quantities involved and the relative estimation issues. In particular, a critical point is represented by the variables related to the aided agent, which need to be estimated in a condition of lack of sufficient data. Their evaluation requires the use of a priori estimation techniques that have been illustrated as well. A comparison between these prediction strategies has been presented, highlighting the advantages and drawbacks of the respective algorithms.

The last section was then devoted to an extensive analysis of the IAR estimate as a random variable and to the impact that several system parameters and variables have on it. From the analysis it has been verified that the sole injection of noise in the system is not responsible for instability in the IAR algorithm. Divergence arises instead with the concurrent presence of feedback, which is unfortunately unavoidable in the IAR estimation scheme. With this in mind, it was observed that the prediction of the user clock bias produces increasing bias and variance in the collaborative range error. This estimation procedure is not the main responsible of IAR measure's deterioration: the estimation of the steering vector of the aided agent is certainly the primary cause of instability. On the other hand, although it adds some uncertainty to the IAR computation, the estimation of the steering vector of the aiding agent does not give birth to divergence phenomena, provided non-divergent positioning solutions of this agent. This happens despite the fact that the aiding agent makes use of a feedback in its PVT algorithm, due to the employment of EKF. The latter introduces correlation but it does not cause error amplification nor instability in the IAR estimation process. The key point is that, in this case the state estimate (and its error) does not re-enter in the PVT computation as a measurement. Instead in the case of aided agent, the state estimate is used to predict variables involved in IAR computation, whose output will become a measurement used to compute the next state estimate. As a consequence, errors contained in such estimates are easily amplified through this closed loop.

The effectiveness of this cooperative paradigm in positioning has been also tested, exploiting a Monte Carlo simulation method. In the next chapter, the characteristics of such simulation framework will be illustrated, along with the features of the software implementation.

Chapter 3

Simulation Framework

To assess its applicability in a dynamic context, the cooperative navigation algorithm based on IAR is tested through a Monte Carlo method in a software simulation environment. Before proceeding to the analysis of experimental results, a characterization of such simulation environment is presented in order to provide a complete picture of the experiment.

A swarm of cooperating agents is managed within the simulation environment through realistic motion dynamics and communication delays. Essentially, the implemented model takes into account all the constraints related to the estimation of the involved variables, thus besides dynamics and network properties, also environmental conditions like sky visibility and measurement noise. In this chapter a classification of the agents is defined in order to build a consistent framework for simulation and a solid basis for the roles of the peers in the cooperative protocol. In a cooperative network of GNSS-based positioning units several random factors may influence the state of the network. Hence, an overview on the uncertainties modeled in the simulation is also presented to complete the picture on the experimental framework.

3.1 Models for the Simulation

3.1.1 Visibility State

As recalled in the introductory part on GNSS (Section 1.1), a receiver that is able to get 4 pseudoranges from 4 satellites can locate itself on Earth. Actually by exploiting the EKF in the navigation algorithm, this limitation can be overcome and a position estimate is made available even for a reduced number of measurements. However the condition of having at least 4 tracked satellites is still indicative of position estimation reliability, since it permits single point positioning without additional information [25]. As mentioned in the description of the IAR method (Section 1.2), the peers eligible for aiding are only those who can position themselves autonomously, i.e. with an acceptable confidence. Hence, we can exploit the aforementioned visibility condition as a good indicator of positioning quality, in order to select a particular set of receivers eligible to become aiding agents. It is convenient to anticipate here that, in this context, those receivers are said to be in a *Fixing state (F)*.

Hereafter a mathematical formalization is defined to classify agents. The definitions given for sets satellites and IAR measurements are resumed from Section 1.2 and extended to be used throughout the chapter. Set notations are reported in Table 3.1. Notice that each set is defined at a specific time instant k, hence the elements included may change for each k.

Name	Symbol
Set of receivers	$\mathcal{N}_k$
Set of satellites	$\mathcal{M}_k$
Set of visible satellites for the j-th receiver	$\mathcal{G}_{j,k}$
Set of collaborating agents for the j-th receiver	$\mathcal{S}_{j,k}$
Set of IAR integrated in the PVT algorithm of j-th receiver	$\mathcal{I}_{j,k}$
Set of agents in F state	$\mathcal{F}_k$
Set of agents in D state	$\mathcal{D}_k$
Set of agents in L state	$\mathcal{L}_k$

Table 3.1: Set definitions.

Assume for now, that everything takes place instantaneously, at time k, and, as a consequence, the definitions that follow temporarily involve only this specific time instant. This is done for clarity reasons, but a further formalization, that includes the communication delays, will be given at the end of the section.

GNSS service availability is represented by means of a *Satellite Visibility Matrix* $\mathbf{V}_k$, defined as

$$\mathbf{V}_k = \begin{pmatrix} v_{1,k}^{1} & v_{1,k}^{2} & \dots & v_{1,k}^{|\mathcal{M}_k|} \\ v_{2,k}^{1} & v_{2,k}^{2} & \dots & v_{2,k}^{|\mathcal{M}_k|} \\ \vdots & \vdots & \ddots & \vdots \\ v_{|\mathcal{N}_k|,k}^{1} & v_{|\mathcal{N}_k|,k}^{2} & \dots & v_{|\mathcal{N}_k|,k}^{|\mathcal{M}_k|} \end{pmatrix} \tag{3.1}$$

where each element $v_{j,k}^{s}$ is a binary variable that indicates if a receiver j sees and tracks the satellite s at time k. More formally:

$$v_{j,k}^{s} = \begin{cases} 1 & \text{if } s \in \mathcal{G}_{j,k} \\ 0 & \text{otherwise} \end{cases}$$

The Satellite Visibility matrix is defined to model the visibility conditions of the satellites signals. Changes in visibility of the constellation or degradation in tracking performances correspond to a binary transition of the elements in (3.1). In the simulation this matrix is updated according to a given transition rate.

From the Satellite Visibility Matrix follows the cardinality of the set $\mathcal{G}_{j,k}$, which for each time instant k is

$$|\mathcal{G}_{j,k}| = \sum_{s=1}^{|\mathcal{M}_k|} v_{j,k}^{s} \ . \tag{3.2}$$

An analogous matrix is defined to manage the availability for cooperation among peers. It is called *Pairwise Visibility Matrix* and it is defined as:

$$\mathbf{W}_k = \begin{pmatrix} w_{11,k} & w_{12,k} & \cdots & w_{1|\mathcal{N}_k|,k} \\ w_{21,k} & w_{22,k} & \cdots & w_{2|\mathcal{N}_k|,k} \\ \vdots & \vdots & \ddots & \vdots \\ w_{|\mathcal{N}_k|1,k} & w_{|\mathcal{N}_k|2,k} & \cdots & w_{|\mathcal{N}_k||\mathcal{M}_k|,k} \end{pmatrix} \tag{3.3}$$

Each element $w_{jl,k}$ of the matrix is again a binary variable that represents the possibility for the agent j to start the IAR algorithm and to receive help from agent l. This event is possible if two conditions are verified:

- a common satellite must be visible and tracked by both receivers;
- the aiding agent l should be in a F state.

The first condition is a necessary condition for the application of the IAR algorithm, while the second is employed to provide a more conservative collaborative method.

The elements in the matrix $\mathbf{W}_k$ can be defined in a more rigorous way:

$$w_{jl,k} = \begin{cases} 1 & \text{if } \exists\ s \in \mathcal{M}_k \colon v^s_{j,k} + v^s_{l,k} = 2\ ,\ l \in \mathcal{F}_k \\ 0 & \text{otherwise} \end{cases}$$

Now from this matrix, which in turn is completely determined by the matrix $\mathbf{V}_k$, the cardinality of the set of collaborating peers for the agent j can be inferred:

$$|\mathcal{S}_{j,k}| = \sum_{l=1}^{|\mathcal{N}_k|} w_{jl,k}\ .$$

Each agent at any time instant k is characterized by the properties of its visibility matrices, that define its role in the cooperation paradigm. The classification of the agent in this sense is performed through the definition of a *Visibility State* that is based upon Satellite Visibility matrix and Pairwise Visibility matrix. The formalizations introduced so far are useful to unambiguously define the current Visibility State of agent j and its transitions throughout the time.

As anticipated in this section, agents in a *Fixing state* (F) or *Fixing agents* are able to retrieve their position by means of GNSS measurements and legacy positioning algorithms. For this class of receivers, the continuity of service is guaranteed, as long as the tracking of at least four satellites is maintained. In this context, they are eligible for the aiding of GNSS-denied agents. It follows that

$$l \in \mathcal{F}_k \iff |\mathcal{G}_{l,k}| \geq 4\ .$$

Among receivers that are not able to satisfy this condition, one particular class is able to exploit collaborative positioning in order to retrieve at least 4 total ranges. Agents of this class are said to be in a *GNSS-denied state* (D) (or *GNSS-denied agents*). They obtain cooperative ranges from Fixing agents but are not allowed to provide aiding. In this case

$$j \in \mathcal{D}_k \iff \begin{cases} |\mathcal{G}_{j,k}| + |\mathcal{S}_{j,k}| \geq 4 \\ |\mathcal{G}_{j,k}| < 4 \end{cases}\ .$$

It should be stressed here that $|\mathcal{S}_{j,k}|$ is the number of single collaborative agents able to interact with the agent j to provide the cooperative range. This means that only the contributions from distinct agents are counted for making a peer eligible of being aided. Actually, if the collaborating peers share more than one satellite, the aided peer can obtain more than one range from the aiding agent. But these estimated ranges would refer to the same euclidean distance between the two agents. Therefore, for conservative reasons, it is chosen to prevent these *multiple IARs* (Sec. 1.2) to contribute to the visibility state definition with more than one measurement. Nevertheless, they may be ultimately used in the hybrid positioning algorithm. The use and managing of these quantities will be further exploited in Chapter 4 when dealing with IAR selection strategies (Sec. 4.3.3).

The last possible Visibility State to which a receiver j can belong is the *Lost state* and receivers in this condition are called *Lost agents*. Agents from this class have an insufficient number of ranges at the disposal, whether they are pseudoranges or come from collaborative peers. They cannot obtain a position fix. In this case

$$j \in \mathcal{L}_k \iff |\mathcal{G}_{j,k}| + |\mathcal{S}_{j,k}| < 4 \ .$$

Notice that the entire set of definitions and states described so far is solely dependent on the configuration of the Satellite Visibility matrix throughout time. In fact, the state of an agent is completely determined by the transformations occurred to $\mathbf{V}_k$, with respect to its sky visibility and that of the other agents. Furthermore, each agent can be in only one state at a time, but its visibility state will likely change several times. The Finite State Machine (FSM) presented in Figure 3.1 illustrates in a compact way the states and their transitions. Throughout an observation time of the simulation, each agent passes several states and its role in the cooperative algorithm change accordingly. As a consequence, an agent may have for instance, past positions based on legacy GNSS algorithms and a current position obtained through hybridized solutions and vice versa.

To complete this formal characterization, the communication delay involved in the IAR algorithm is now considered, in order to get rid of the instantaneous communication assumption done at the beginning of the section. In section 2.3, a specific time sequence of operations was defined w.r.t. RTT. As a consequence the above definitions must be refined in order to consider timing constraints and latency.

In particular, the elements of the pairwise visibility matrix (3.3) are now modified: the conditions for an agent j to cooperate with agent l to obtain a IAR, require that a common satellite must have been visible at different time instants. Also, the agent l should have been in Fixing state at that instant. In other words

$$w_{jl,k} = \begin{cases} 1 & \text{if } \exists \ s \in \mathcal{M}_k : v^s_{j,k} + v^s_{l,k-\tau_2} = 2 \ , \ l \in \mathcal{F}_{k-\tau_2} \\ 0 & \text{otherwise} \end{cases} \ . \tag{3.4}$$

All the other definitions are eventually updated according to (3.4) and they hold without modification. The above condition completes the model, that is now totally coherent with the structure of the Monte Carlo simulation implemented within the context of this work.

To conclude, the characteristics of each class of agents are summarized in Table 3.2, along with a brief description of the visibility states and their definitions, for future reference throughout the reading.

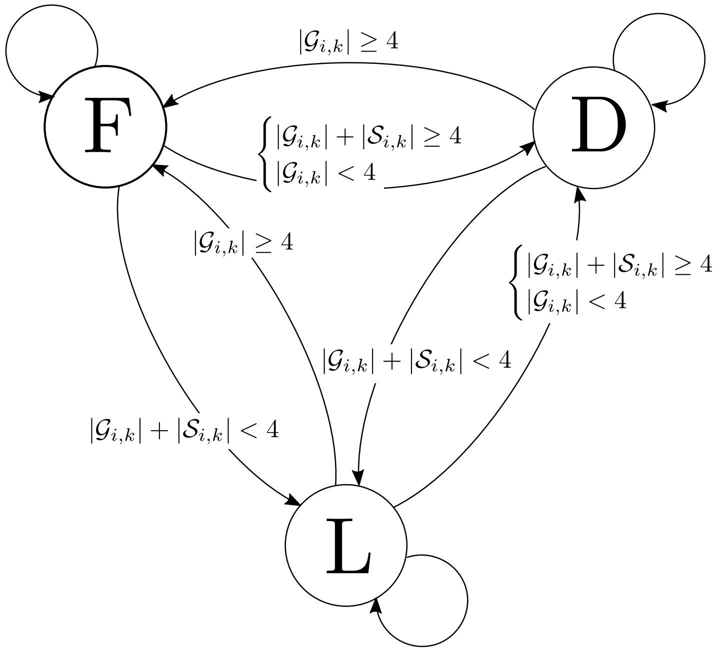

Figure 3.1: Finite State Machine for visibility states. At each time instant k a transition is triggered.

State	Condition	Description
Fixing (F)	No. of SV in view ≥ 4	Agents able to obtain the position without external aiding. They are available to provide aid.
GNSS-denied (D)	No. of SV in view < 4. No. of SV in view + no. of collaborating peers ≥ 4.	They are not able to retrieve the position autonomously, but can obtain more than 4 ranges through cooperation. They are not allowed to provide aid.
Lost (L)	No. of SV in view + no. of collaborating peers < 4.	They cannot obtain a fix either autonomously or with cooperative ranges.

Table 3.2: Visibility State summary.

3.1.2 Environment Dynamics

In order to provide a complete picture of the experiment's framework, one last section is devoted to the description of randomness present in the system and consequently modeled in the simulation.

A complex network of moving and communicating peers is characterized by a high number of elements and many of them are modeled as random processes. Among the random processes that influence the system behavior, the most significants are the measurements noise, the navigation path and the progression of the visibility states. All of these random processes evolve during the observation time and they are all independent among agents.

The measurement noise affects the pseudoranges and is normally-distributed, as described in Section 1.1, with variance $\sigma^2_{UERE} = 7.03\,\mathrm{m}$ [14] if not otherwise specified.

The navigation paths traveled by the agents are created mainly by two different generators. A generator produces motion dynamics according to the EKF motion model equation (2.3). It corrupts an agent state obtained through (2.3) by means of matrix $\mathbf{\Phi}$, with a set of random samples extracted from a multivariate normal distribution with covariance matrix $\mathbf{Q}_k$. In this way the EKF has a perfect knowledge of the system noise and can perform at its best, fostering an analysis focused on other sub-optimal effects. This generator is also exploited to assess the validity of the algorithms on an unconstrained trajectory. To this purpose, the resulting path will be referred to as *random trajectory*.

The other traffic generator is alternatively employed to pursue a more realistic scenario. The generated trajectories are provided by the SUMO software[1], which is a microscopic road traffic simulator designed to handle large road networks. This kind of road simulations are partially deterministic, but there are various options for introducing randomness. However the details of the SUMO setup are omitted since they are outside of the scope of this dissertation.

The visibility states are all derived from single satellite visibility conditions: for each agent a given satellite may be visible or not with probability 0.5, i.e. in a discrete uniform distribution fashion. With this assumption, the progression of visibility states is generated for each agent. However, a constraint on the random generation is imposed at each instant, in order to produce a desired number of agent in a D-state.

It has to be remarked, however, that these random processes are managed in different ways, with respect to the experimental necessities. In fact, in order to have a meaningful analysis, the path characteristics and the sky conditions relative to a single agent needs to be repeated through each realization of the experiment. This allows to observe the statistical properties of valuable outputs, such as position and IAR estimate, with respect to specific sky visibility conditions and particular motion dynamics.

As a consequence, in this analysis framework either the visibility states and peers trajectories repeatedly follows the same randomly extracted sequence during each realization of the simulation, while measurements noise samples are unconditionally randomly extracted along time and across realizations. As a matter of fact, each measurement sample is extracted from a Gaussian distribution and the random sequence is never reseeded while spanning throughout the process realizations.

---

[1] Simulation of Urban MObility software [26]

Chapter 4

Results

Within the extensive analysis on estimated IAR characteristics carried out in Chapter 2, a non-trivial attribute of the IAR process emerged: a tight relationship of this cooperative paradigm with past position estimates. Obviously the cooperative data alter the current position estimate $\underline{\hat{\mathbf{x}}}_{A,k}$, since they are incorporated as additional ranges in the set of measurements exploited to obtain the PVT solution. But the peculiarity of this relationship is the fact that $\underline{\hat{\mathbf{x}}}_{A,k}$ is partially involved in the computation of a measurement (the IAR) for the forthcoming position estimate, due to the prediction efforts demanded by the IAR estimation procedure. As a result, the IAR estimate $\hat{I}^{s}_{AB}$ is not only affected directly by parameters that appear in IAR estimation formula (2.30), but also from all the events and conditions that have an influence on position estimation. Therefore also network characteristics, environmental conditions and specific trajectories realizations, that also affect $\underline{\hat{\mathbf{x}}}_{A}$ directly, will impact this collaborative range and consequently future position estimations. The result is that all the variables involved in the hybrid PVT algorithm may have a broad impact on the following positioning epochs, that, as seen in Section 2.4 could also lead to instability.

A consequence of this widespread impact is that the evaluation of positioning performances is a hard task, due to a non-straightforward analysis of the effects. As a result, the accomplishment of a fine tuning of the algorithm is challenging, due to the difficulty related to an empirical evaluation of optimal parameters. However, tuning is extremely important and could prevent instability and divergence both in IAR and position estimations.

Another consequence is that a complete separation of the positioning performances from its effects on IAR would be limiting, but in the tentative to keep a continuity with Section 2.4 and to provide a meaningful performance analysis, this chapter will be focused mainly on positioning outcomes.

The objective of this chapter is to analyze the estimated position error of the aided agent, when the GNSS fix is obtained through a hybrid PVT stage based on Inter-agent Range. First, some preliminary results are reported, testing the cooperative algorithm as presented so far. The analysis of results is mainly focused on single agents trajectories, evaluating several scenarios through different case-studies, in order to show strengths and weaknesses of the current algorithm configuration with respect to different situations. A comparison with a EKF-based positioning solution, which does not exploit cooperative ranges is presented. In this case the outage periods are managed by the EKF, that integrates the previous position and updates the estimate through available observations. This analysis is carried out also to find room for improvements, therefore after this preliminary evaluation some tunable aspects are discussed in order to reduce positioning errors.

A fine-tuning is carried out exploring different approaches. First, the investigation is focused on possible measurement model refinements, assessed by means of an optimization procedure. Consequently, the implementation of a heuristic technique that acts on the error covariance matrix $\mathbf{P}_k$ is discussed. The analysis is then oriented mainly to the observation of single user's positioning within the network, i.e. with respect to the aiding received by multiple agents. This point of view foster the study of the cooperative ranges as a set, giving the chance to manage them through aggregation methods and selective criteria. Thus after the refinement of Kalman filter's models, these strategies are discussed and the resulting positioning outcomes are presented.

In the end, the proposed configurations are tested and the effective improvement on preliminary results is assessed. After performance validation the IAR method is extended in order to integrate improvements.

It should be mentioned here that even if the analysis is mainly devoted to the study of a single user's position error, a network perspective is often provided. The evaluation of overall average position errors experienced by the entire network of peers is important in order to have a general point of view and to give a case-independent evaluation on performance. In fact, more often than not, system tunable parameters have an impact on position error that strictly depends on the current user's scenario (motion dynamics, sky visibility, neighboring peers). As a consequence, aggregated data are often used to assess the average performance of the network and consequently provide a valuable metric for parameters optimization.

4.1 Simulation Setup and Performance Metrics

The simulation setup is reported in Table 4.1. This configuration holds for all the analyses presented throughout the chapter, unless different specifications are explicitly mentioned. The constellation dynamics (Sec. 1.1) are extrapolated from rinex files and simulated with respect to the specific location and time.

Before proceeding with the analyses of results, it is useful to define the *position error*

$$\mathbf{e}_p = \underline{\mathbf{x}}_i - \hat{\underline{\mathbf{x}}}_i \tag{4.1}$$

$$\mathbf{e}_p = (e_x \quad e_y \quad e_z)^\top \tag{4.2}$$

and its norm

$$e_p = ||\mathbf{e}_p|| \tag{4.3}$$

Notice that the position error $\mathbf{e}_p$ is a random vector. Throughout the study then, each position error $\mathbf{e}_p$, at any time instant, is characterized through a Monte Carlo approach, by a high number of simulated realizations in order to be statistically meaningful. Moreover, to deal with general network analyses, $\mu_{\mathcal{N}}$ will be used to indicate the network average of the mean position error μ_{e_p} experienced by each agent. In a similar way $\sigma_{\mathcal{N}}$ represents the network average of the position error standard deviation of a single agent σ_{e_p}.

Parameters	Value
Number of Agents	30
Number of GNSS-denied Agents	10
GNSS System	GPS
σ_{UERE}	7.03 m
Location	Turin (45° 4’ 5.2716" N 7° 39’ 28.818" E)
Starting Time	9-22-2017 12:17:28 UTC
Observation Time	60 s
RTT	1 s
Agents geographical distribution (σ)	1000 m s
Visibility Matrix $\mathbf{V}_k$ update rate	10 s
S_p	1.0 $(\mathrm{m/s^2})^2/\mathrm{Hz}$
S_f	$0.4 \cdot 10^{-18}$ $(\mathrm{m/s^2})^2/\mathrm{Hz}$
S_g	$1.58 \cdot 10^{-18}$ $(\mathrm{m/s^2})^2/\mathrm{Hz}$
Process Realizations	1000
Position update rate	1 Hz

Table 4.1: Simulation setup. S_p, S_f and S_g are spectral densities associated respectively with position, clock bias and clock drift as defined in Section 2.1. Values taken from [20]

.

As a meaningful reference for performance evaluation, a comparison with the outcome of a *non-cooperative* positioning algorithm is often provided. The PVT stage of this solution is still based on an EKF, but the integration of cooperative measurements in the set of observations is prevented. In this way the output of the EKF is based on the pseudoranges only, which are integrated according to widely tested models, since the EKF is a well established procedure for solving PVT in the GNSS community [27]. An EKF-based non-cooperative PVT is thus a valuable benchmark for this comprehensive analysis.

4.2 Preliminary Results

In this section, some preliminary results from the application of IAR hybrid positioning technique are presented. Because of the high heterogeneity of environmental conditions and scenarios, several case-studies are presented. The simulated scenarios involve both motion dynamics and sky visibility, but also network constraints (such as RTT). These case-studies are investigated in order to provide a valuable analysis of hybrid positioning performances that holds for the most common situations, or to show limiting conditions of IAR paradigm’s applicability.

The algorithm is implemented in its basic architecture as described so far, without additional modifications that will eventually follow from fine-tuning and optimization. In particular, the elements of the measurement covariance matrix (2.19) are set to their upper bounds (2.20) and (2.21), as a suitable conservative choice for this preliminary analysis.

4.2.1 Case 1: Reduced Visibility

In Figure 4.1 the evolution of a receiver's path is presented, over a time interval of 60 seconds. An agent estimates its position along a trajectory, exploiting cooperative techniques when needed, i.e. when less than four satellites signal are being tracked (GNSS-denied or D state). Two types of predictive techniques can be employed within the IAR algorithm (Sec. 2.3) and the resulting estimations are shown in Figure 4.1b and 4.1a. The two figures show the evolution of true position state $\underline{\mathbf{x}}_A$ and estimated position state $\hat{\underline{\mathbf{x}}}_A$. Visibility states are also displayed in the graphs.

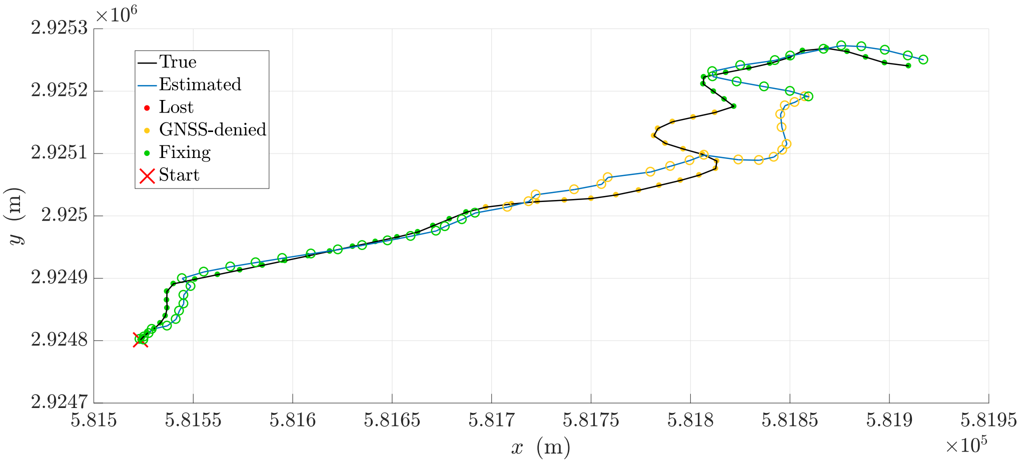

(a) KF a priori estimation

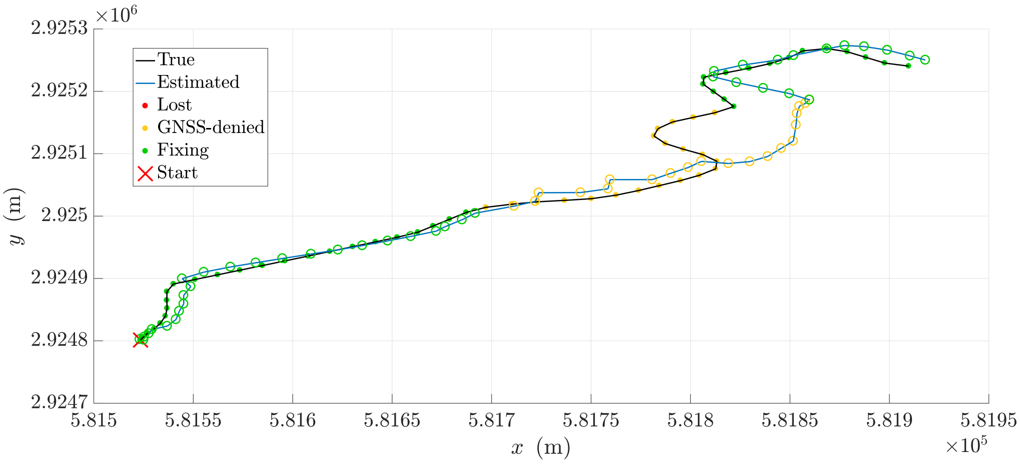

(b) EKF quasi-a-priori estimation

Figure 4.1: Hybrid positioning with IAR measurements. Agent's path observed for 60 seconds. Visibility states are highlighted.

In order to have a statistically meaningful result, each displayed position is the result of 1000 Monte Carlo simulations (Table 4.1), where in each instance a different sequence of measurement noise samples is extracted, while the agent motion evolution and GNSS visibility conditions are fixed, as described in Section 3.

During the fixing epochs the estimated trajectories show a small position error. The real trajectory is smooth and the PVT routine can easily follow it. When a GNSS outage occurs however, the number of tracked satellites is reduced and, despite the cooperative aid, the estimated trajectories react slowly to the change in direction with both prediction schemes (Figures 4.1a and 4.1b).

The effectiveness of a positioning algorithm is related to the number of measurements exploited in the PVT calculation and their quality. From the analyses presented in Section 2.4, it was observed that the IAR is often a worse range estimate than pseudoranges, especially after many outage epochs. As a result, the capability of the tightly-integrated EKF to track an agent's position is still dominated by the number of satellite in visibility (and the relative pseudorange measurements available).

In order to inspect the visibility conditions deeper, Figure 4.2 is provided. In the picture the number of ranges integrated in the PVT of the considered agent's path is shown for each epoch. Moreover, further information on performance is given: the evolution of position error is summarized through the average and standard deviation of its norm.

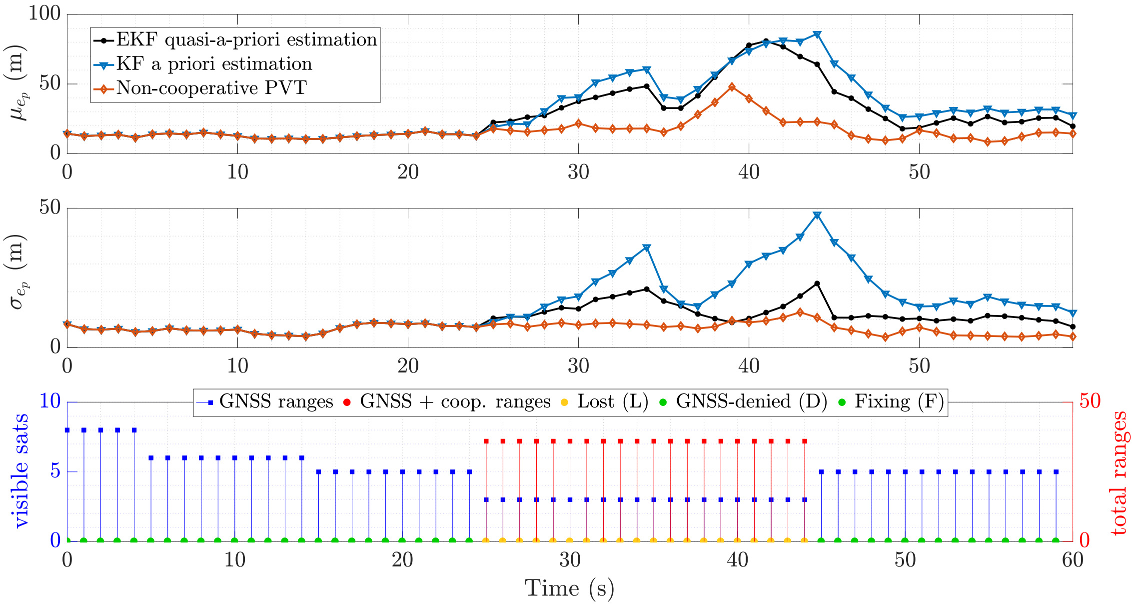

Figure 4.2: Case 1: position error statistic. Average and STD of position error norm are shown along with visibility states progression. An outage of 20 seconds is present.

Figure 4.2 shows that within the current trajectory, 3 satellite signals are tracked during the outage period of 20 seconds. With such visibility, the EKF-based PVT is able to provide quality results even in its non-cooperative version. As a matter of fact, it has been simulated a plain non-cooperative positioning algorithm based on EKF, that integrates just legacy GNSS measurements. The resulting positioning performance is shown in Figure 4.2 as well.

In these conditions, a non-hybrid PVT solution produces, in the outage interval, a smaller average position error, also characterized by a lower variance. A reason may be the well known effectiveness of the EKF in satellite navigation systems [28]. In the case of the regular non-cooperative PVT algorithms the ability of the EKF to optimally update an estimate with the available measurements is widely used and efficiently exploited. Moreover the Extended Kalman filter can provide optimal estimation with any number of input measurements. A PVT stage based on LMS iterations would not be able to converge to a solution with 3 input ranges, but an EKF is able to supply good quality estimates also with a reduced sky visibility (4.2). Hence, this effectiveness is particularly relevant when the PVT is just one measurement away from a full convergent LMS, as in the considered scenario.

The high number of pseudorange observations may be the reason of success of the non-cooperative PVT over the IAR paradigm, because in this condition the biased IAR measurements may be overwhelmed by EKF's optimality for the non-cooperative case, making the additional ranges unnecessary.

4.2.2 Case 2: Severe Outage

During a more severe outage instead, the EKF-based PVT estimation may be not enough accurate if a sufficient number of pseudorange measurements is not present. In this situation the use of additional ranges may be essential. In Figure 4.3 another realistic trajectory is displayed. In this case the GNSS receiver moves within a more harsh environment and it often experiences a reduced sky visibility.

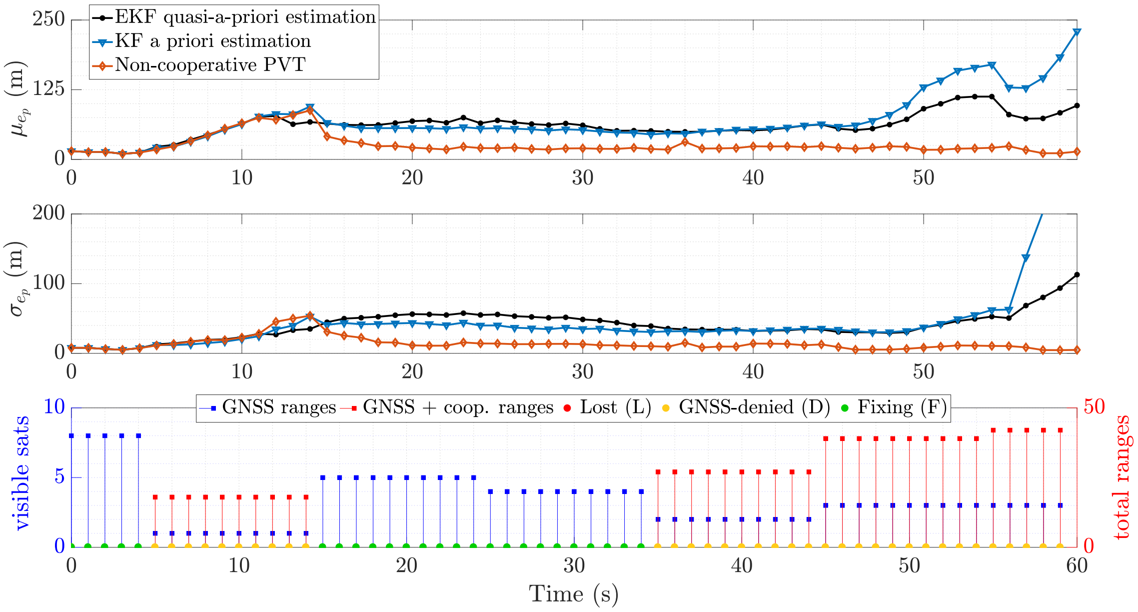

Figure 4.3: Case 2: position error statistic. Average and STD of position error norm are shown along with visibility states progression. A severe outage is present, where the signal from only 1 satellite is tracked.

In the first outage interval the agent is able to track only one satellite. The output of the non-cooperative algorithm in this case is more prone to this single pseudorange variability and the provided position estimate has a higher STD with respect to a cooperative solution, where more measures are combined to obtain a position. After the outage, however, the two cooperative positioning curves struggle to return to less harmful levels of position error, and the non-cooperative PVT generally provides a better guess on position.

With the plain tight-integration model presented so far, the collaborative ranges are not able to provide a significant advantage to the positioning. Furthermore, they eventually cause the position error to drift after a long outage period (Figure 4.3).

4.2.3 Case 3: EKF Sub-optimality

The filter modeling is fundamental to accomplish good positioning performance. However, the EKF/IAR tight integration is a novel approach and the modeling still need a fine-tuning to be competitive with the non-cooperative EKF.

The design of the EKF is based on two model equations: the system model equation and the measurement model equation (Section 2.1). A perfect knowledge of the real models is generally not available and the rise of non-modeled effects makes the estimator to be sub-optimal.

Nevertheless, the system model is the same for the cooperative and non-cooperative case. It describes the system dynamics, which is independent from the measurements integration. However, the use that the two paradigms do of such models is different. The Kalman models are massively exploited within the IAR paradigm, since prediction filters are essential to provide each additional Inter-agent range. For these reason, non-modeled processes have a broader impact in hybrid positioning, along with all the other variables involved, as explained in the analysis of impact factors of Section 2.4.

In the end, the model's deficiency will penalize more the IAR paradigm than the non-cooperative solution, producing poorer performance. As a consequence the rougher is the model and the poorer will be the hybrid-PVT estimate w.r.t. the non-cooperative output. To investigate this aspect a particular trajectory simulator is exploited. This simulator outputs *random trajectories* (Sec. 3.1.2) that are build under the exact application of the system model equation (2.3), here reported

$$\mathbf{x}_k = \mathbf{\Phi}\mathbf{x}_{k-1} + \eta \sim \mathcal{N}(\mathbf{0}, \mathbf{Q}) \ .$$

As explained during the simulation environment description (Sec. 3.1.2), this kind of path realization is perfectly modeled by the EKF, which has an exact knowledge of the system noise and consequently can perform at its best. Through a simulation experiment based on this kind of trajectories the analysis can be focused on other effects and the comparison with non-hybrid EKF is free from the impact of a sub-optimal modeling of system dynamics.

A sample trajectory of this kind is shown in Figure 4.4, where in the left panel a position estimated through the IAR method is shown, while the outcome of a non-cooperative PVT is drawn in the right panel. The figure provides a more informative representation of an agent's path, w.r.t. previous trajectories representations, because, besides the average estimated trajectory, also the standard deviation information is presented by means of the axis-relative errorbars.

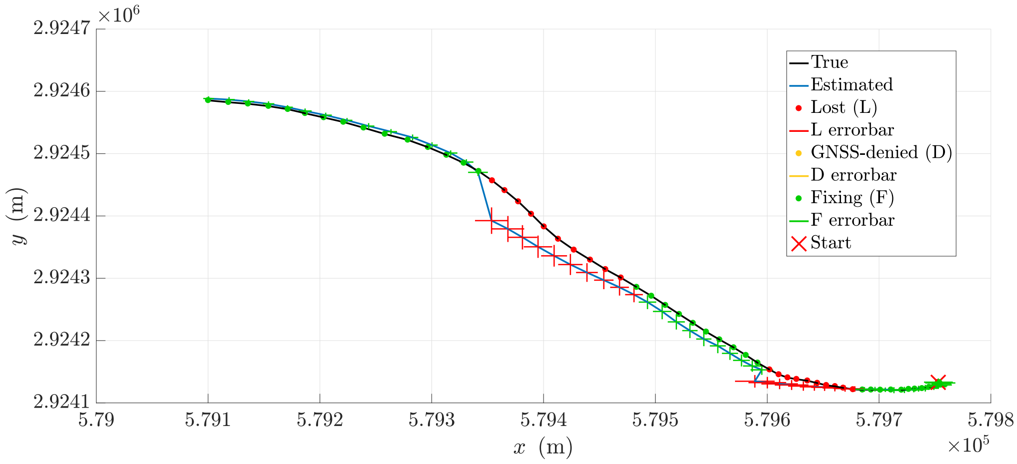

(a) Non-cooperative estimation

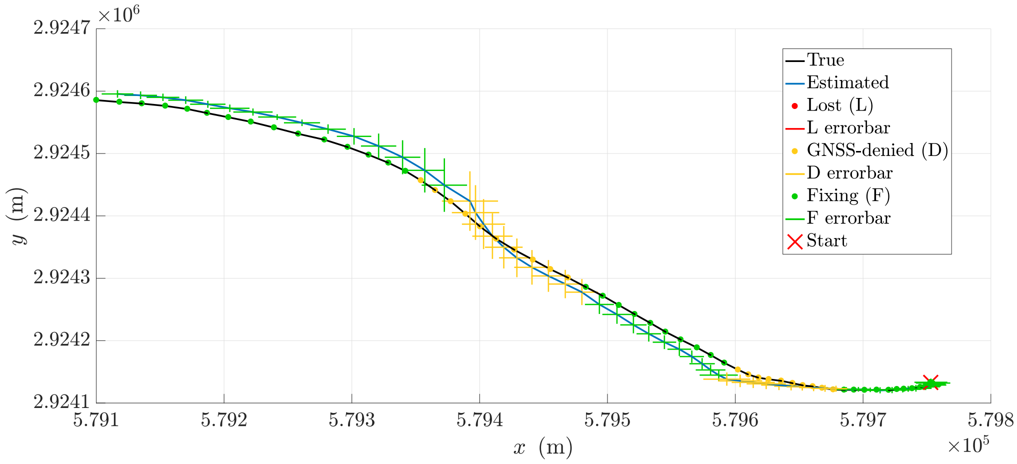

(b) EKF quasi-a-priori estimation

Figure 4.4: Case 3: simulated trajectories. Agent's path observed for 60 seconds. Visibility states are highlighted and STD errorbars are visible.

In this idealized estimation condition, the Kalman filters present in both positioning paradigms (non-cooperative positioning and IAR hybrid positioning) model exactly the motion dynamic of the agent. Under this assumption, a significant reduction of the gap between the two techniques is observable, suggesting that the IAR method was more penalized by erroneous assumptions on the system model (2.3). The same benefits are not visible looking at the STD. In fact the errorbars show a growing variance of the hybrid estimation, that quickly become greater than its non-cooperative counterpart. Moreover, the variance degradation continues after the outage period, due to the propagation of the error covariance matrix $\mathbf{P}_k$ that takes into account the increased number of measurements employed during the outage.

In order to have a less qualitative evaluation, a comparison among the position errors is provided in Figure 4.5. The plots provide also a fair comparison w.r.t. Figure 4.4, since they show the norm of the position error, which takes into account all the three axis. The plots include also the positioning error experienced by an agent that employs the KF as a predictive filter.

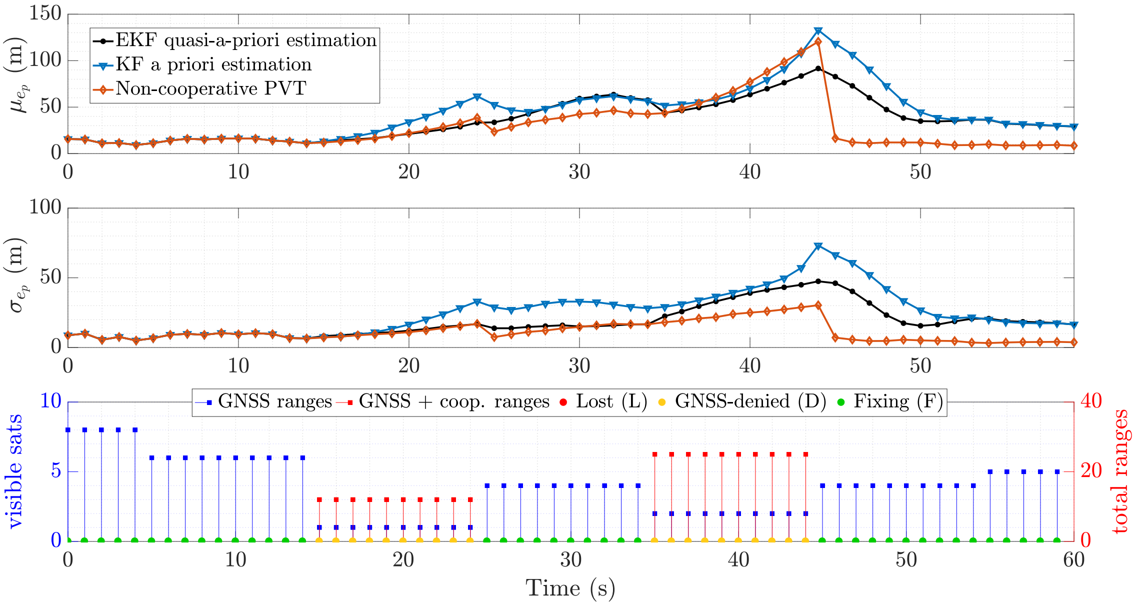

Figure 4.5: Case 3: position error statistic of a randomly generated trajectory. Average and STD of position error norm are shown throughout time, along with visibility states progression.

Figure 4.5 confirms the previous considerations: the hybrid positioning is often able to overcome the average position error given by the non-coperative estimations during outages, but the σ_{e_p} curve is always higher. Therefore, in this case, the current implementation of the IAR method results in a more accurate but less precise positioning during the outage intervals.

Observing the hybrid positioning outcomes from the previous sample trajectories (Figure 4.2 and 4.3), it can be noticed that bias and variance of the error struggle to return to less harmful levels after an outage period. This behavior may be the result of an excessive trust of the filter in cooperative measurements, that are affected by a variance that does not meet the model's expectations. This trend is again present in this last example (Figure 4.5), where effects possibly caused by an imperfect knowledge of the statistic of system noise were prevented. This is a further clue that a model refinement should be directed toward a finer design of a measurement model (i.e. of the measurement noise covariance matrix $\bar{\mathbf{R}}$) suited for the IAR paradigm. The current implementation represents a coarse approximation of the reality that is often unacceptable and such refinement is essential to design a competitive cooperative algorithm.

To this purpose, in Section 4.3 a fine-tuning of the IAR-related parameters of the measurement model will be accomplished through empirical evaluations. Moreover, no selective strategy has been applied so far on additional ranges and, if the measurement model is often a poor approximation, the management of a great number of unselected cooperative ranges will likely make a fine estimation a harder task.

4.2.4 Effects of Communication Delay

Little attention has been paid so far to the comparison between the positioning performance of the two different a priori estimation techniques involved in IAR algorithm. Referring again to previous sample trajectories drawn in Figures 4.2, 4.3 and 4.5, some small differences can be noticed. The two estimated track are identical when the agent is in Fixing state (3.2), but, as GNSS outage arises, the estimates based on KF prediction exhibit a slightly worse position error, both w.r.t. average and STD. As underlined in previous chapters, this technique involves an a priori estimation that does not exploit measurements, and this affects the IAR estimation in a negative way. Hence it results in a poorer position estimate as well.

This drawback of the KF predictive stage is even more dangerous in presence of non-negligible communication delays, because the KF AP estimation is more influenced by the network latency than the EKF QAP estimation. This is a consequence of the fact that in the Algorithm 1, the aided agent transmits its steering vector $\hat{\mathbf{h}}^{s}_{A,k}$ together with the help request at time $k - RTT$. It needs therefore to predict its steering vector $\hat{\mathbf{h}}^{s}_{A,k}$ 1 RTT forward, without available observations related to the future time k (Sec. 2.3.1). The goodness of its prediction is then strongly dependent on the prediction effort required. On the contrary, in the algorithm based on EKF QAP estimation (Algorithm 2), the estimation of the steering vector $\mathbf{h}^{s}_{A,k}$ is performed at time k and taking advantage of current measurements (Sec. 2.3.2). In this IAR estimation process, the only variables affected by aging are those retrieved from agent B, $\hat{r}^{s*}_{B,k}$ and $\hat{\mathbf{h}}^{s*}_{B,k}$ (2.35) which are necessarily dependent on τ_2, since the response communication delay cannot be bypassed (and this holds also for the KF AP algorithm). As a result, positioning based on this last IAR estimation algorithm is far more robust to network latency issues.

These considerations are confirmed by Figure 4.6 that summarizes the overall network performances of these IAR implementations where three different RTT are experienced. The dependency of the position error on the communication delay is in fact largely reduced in the EKF-based prediction (Figure 4.6b) w.r.t. the KF case (Figure 4.6a).

Other differences in the reported curves may be due to the quality of variables involved in (2.35). Since they change in time, an older variable has different characteristics that may alter the position error. For this reason an evaluation of latency effects based on specific trajectories as done so far would have produced misleading results. In fact a greater RTT may lead sometimes to lower position errors if the chosen variables are accidentally more accurate than a less aged version of them. An aggregated network metric has been then employed to provide a more significant average behavior.

As shown by Figures 4.6a and 4.6b, the simulated network latencies are in the order of seconds. Communication delays of this kind are fairly over-conservative envisioning a modern communication system like the upcoming 5G, where the latencies addressed are around 1 ms [24]. Despite this, GNSS receiver's usual update rate is 1 Hz [17], therefore a simulated RTT of 1 s represents a realistic choice. Due to the relatively slow update rate in fact, the newest position available before the completion of the current PVT stage is 1 second old. Hence, as long as the RTT is less than the GNSS update interval, a $RTT = 1\,\mathrm{s}$

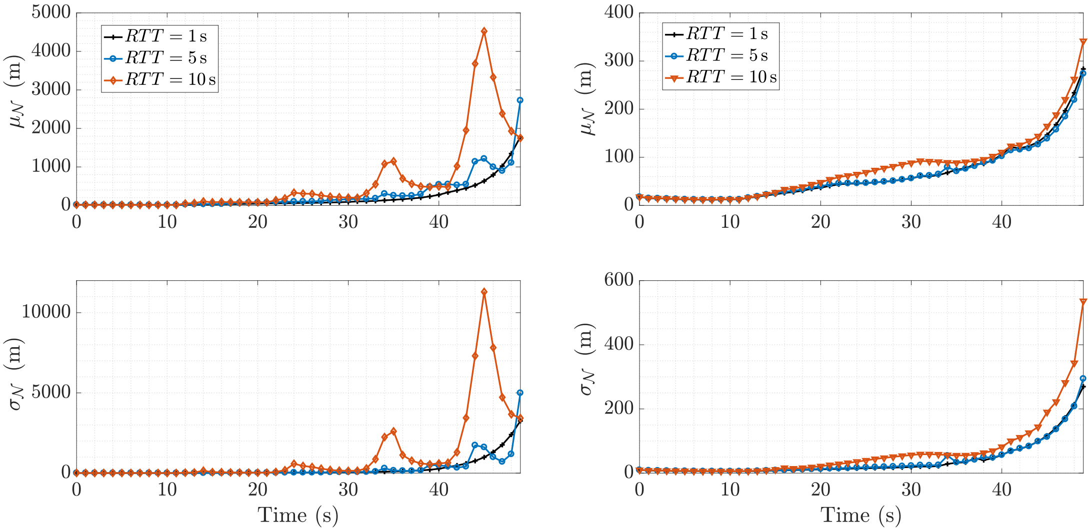

(a) KF AP estimation

(b) EKF QAP estimation

Figure 4.6: Network position error statistic. Network average of μ_{e_p} and σ_{e_p}. Different network latencies are simulated.

suits the vast majority of cases and congested network scenarios.

Despite the bound imposed by the update rate, communication delays closer to the characteristics of modern wireless communication systems have been simulated, to provide a deeper investigation of the limits of the IAR paradigm. The experiment is carried out simulating a GNSS update rate of 100 Hz. Consequently a time step granularity of 10 ms is exploited to impose a RTT of 20 ms and 100 ms on the target network of agents (Figure 4.7).

Limited effects of RTT in the EKF QAP estimation version are also negligible in this low-latency example. The behavior of the KF AP estimation version is instead more affected by the delays experienced in the network as in Figure 4.6a. Notice the lower position error present w.r.t. Figure 4.6, obtained thanks to the frequent availability of measurements in fixing epochs and to the limited motion dynamics within this short observation time (6 s).

4.2.5 Virtual Landmark Numerical Effects

As introduced in Section 1.2.3, the *Virtual Landmark* technique [13] is a method for hiding the position of agent B, thus guaranteeing confidentiality during the cooperation. Until now, this expedient has been considered an equivalent technique that does not affects positioning performance. In fact, the determination of the virtual landmark (VL) $\tilde{B}$ and its range $\hat{r}^s_{\tilde{B}}$ in (1.42), performed by means of the displacement vector $\delta\underline{\mathbf{x}}_{B\rightarrow\tilde{B}}$, is a known transformation that does not add uncertainty to the quantities involved.

However, a different reference position of the aiding agent B in the cooperative algorithm

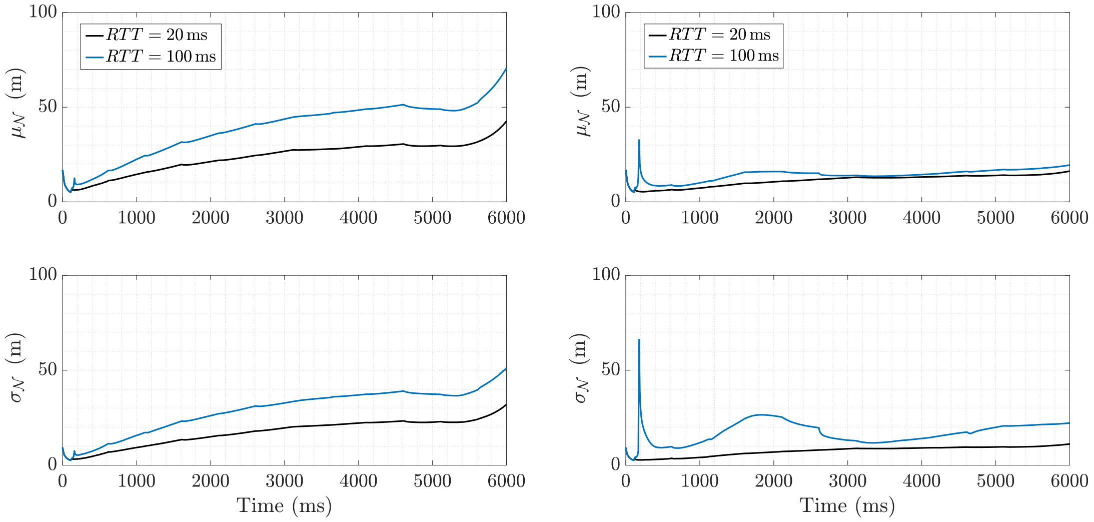

(a) KF AP estimation

(b) EKF QAP estimation

Figure 4.7: Network position error statistic. Network average of μ_{e_p} and σ_{e_p}. Observation time is 6 s, GNSS update interval is 10 ms.

alter the variance of the estimated IAR even if the range involved are affected by the same error. In fact, due to the different geometries involved, the projection of the range error on the estimated baseline $\hat{I}^s_{A\tilde{B}}$ is characterized by a different uncertainty. In the end, although the retrieved cooperative range $\hat{I}^s_{A\tilde{B}}$ is consistent with the new position (the VL), the positioning performance may be altered. As an example, the trajectory considered in Section 4.2.1 is resumed in Figure 4.8. The agent is surrounded by the same collaborative agents that this time take advantage of the VL technique. As a consequence, a different outcome is observable w.r.t. the non-confidential cooperation already considered.

However, one of the critical points of the basic IAR estimation is the fact that the calculation in (2.30) have to deal with extremely small angles γ. In fact, the relative distance between any agent belonging to the same communication network can be certainly assumed much smaller than the distances between such receivers and the GNSS satellite. Small values of $\hat{\gamma}$ cause indeed higher variances of the collaborative measurements [13]. Moreover, this kind of calculation are prone to numerical errors, that may result in very large variations of the estimated euclidean distance between the two peers ($\hat{I}^s_{AB}$).

A possible countermeasure is the introduction of displacement vectors with very large magnitude, not necessarily comparable to the distance between the considered GNSS system constellation and the Earth, but sufficiently large to cope with the finite precision of the simulation platform (MATLAB). When dealing with larger baselines, the angles involved in (2.30) take reasonable values. This efficient exploitation of the existing privacy oriented VL technique results in a massive reduction of numerical errors phenomena.

This technique provides general benefits to the entire network, even if not directly observable from the specific case of Figure 4.8. Therefore in Figure 4.9 an aggregated

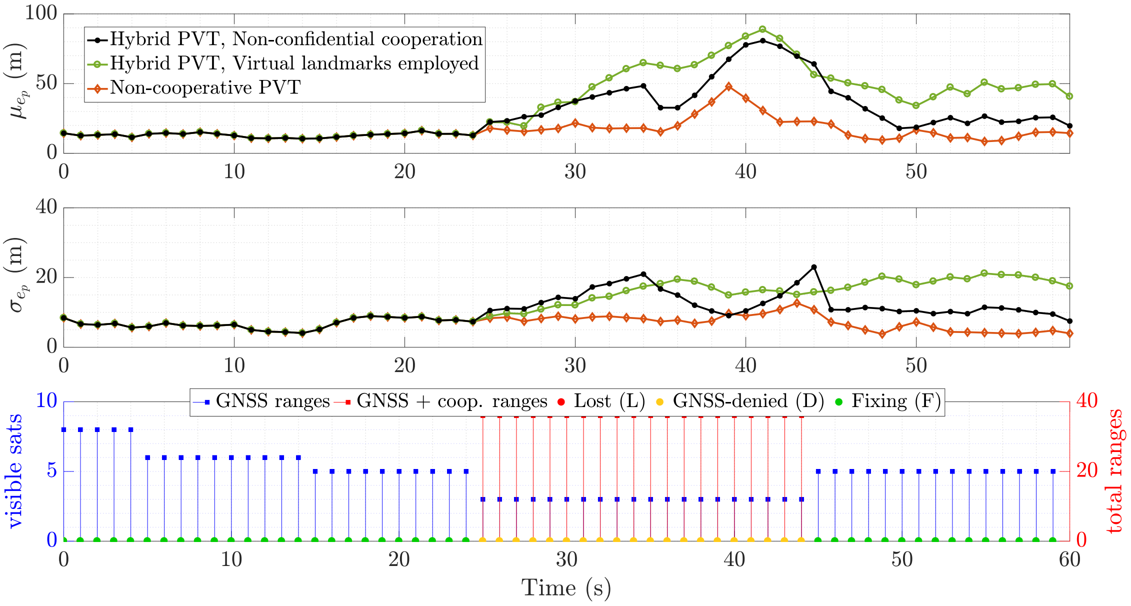

Figure 4.8: Position error statistic with virtual landmarks. EKF quasi-a-priori estimation is employed. The average magnitude of the displacement vectors used by collaborating peers is 350 km. .

network statistic is shown, in order to underline the general validity of this method.

4.3 Algorithm Tuning and Optimization

Experimental results from a preliminary hybrid positioning implementation show limited improvements with respect to a non-cooperative positioning solution based on the Extended Kalman filter. From the analysis, the weaknesses of the IAR method implementation emerged, underlining the area towards which improvements of the algorithm should be addressed. The feasibility of these improvements is assessed in this section and the proposed solutions are evaluated by means of experimental results.

In particular, the optimization of tunable parameters applied to the Kalman filter's measurement model is achieved through empirical methods. In addition, the effectiveness of a heuristic solution is also studied. Selective strategies on cooperative ranges are proposed as well and evaluated with respect to different filtering criteria.

4.3.1 Measurement Model Optimization

The experimental results discussed in Section 4.2 suggests that the models over which the EKF is based needs some further refinements in order to make the EKF/IAR tight integration an effective cooperative strategy. The model of the system dynamics is common to cooperative and regular positioning algorithms. It is indeed related to the user dynamic, independently from measurement observations. Thus a perfect knowledge of the system

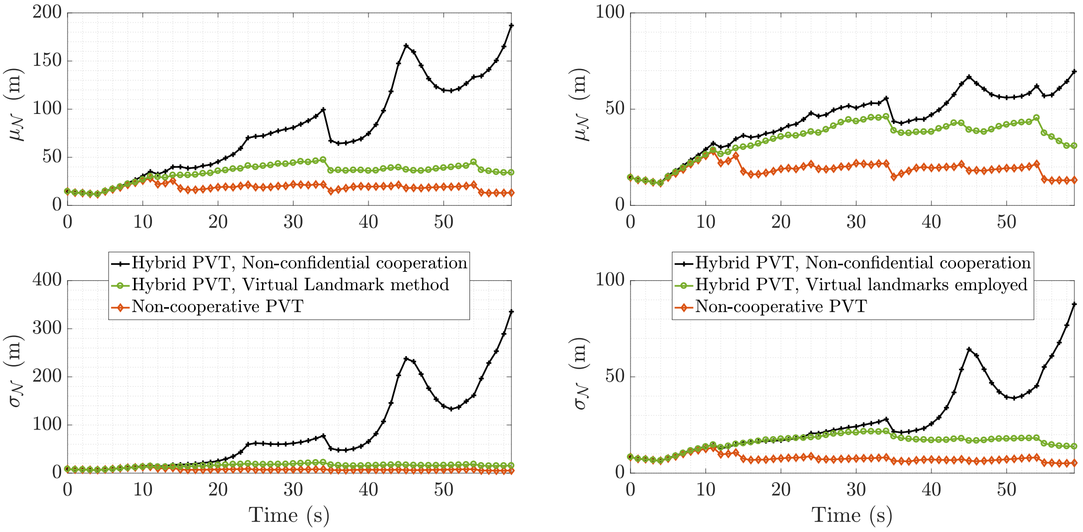

(a) KF AP estimation

(b) EKF QAP estimation

Figure 4.9: Network position error statistic with virtual landmarks. Network average of μ_{e_p} and σ_{e_p}. The average magnitude of the displacement vectors used by collaborating peers is 350 km.

dynamic would be optimal also for the IAR method and there is no need for specific adjustments. This holds also when the imperfections of such model have a wider impact on state estimation, as in the case of IAR positioning (Sec. 4.2). Hence, tuning efforts needs to be oriented towards the measurement model equation of the Extended Kalman filter. Particularly relevant in this case is the role of measurement noise covariance matrix $\bar{\mathbf{R}}_k$ defined in (2.19).

In Section 2.1 the EKF routine was adapted to the IAR paradigm by a proper manipulation of the measurement noise covariance matrix $\bar{\mathbf{R}}_k$ (2.19). Among the assumptions made for the preliminary results reported at the beginning of this chapter, the diagonal elements of $\mathbf{R}_I$ (i.e. the variance terms $\sigma_{\hat{I}}^2$) were assumed equal to their upper bounds (2.20). The other assumption made so far concerns the cross-correlation terms among pseudoranges and cooperative ranges, that define the sub-matrix $\mathbf{R}_{\rho I}$ (and its transpose $\mathbf{R}_{\rho I}^\top$). The elements of the matrix are the covariances $\sigma_{\rho\hat{I}}$ of random variables $\hat{I}_{jl}^s$ and ρ_j and they were set equal to their relative upper bounds (2.21).

Assigning the maximum value to elements of $\bar{\mathbf{R}}_k$ may result in an over-conservative strategy. In order to improve the performance of the algorithm and to approach a covariance matrix definition closer to the real noise characteristics, a finer configuration of the matrix $\bar{\mathbf{R}}_k$ is required.

For what concerns $\hat{I}_{jl}^s$, the real value of the variance can be approached exploiting the approximated formula derived in [12], where the IAR variance is defined as

$$\sigma_{\hat{I}}^2 = (\sigma_{UERE,j}^2 + \sigma_{UERE,l}^2)\sin^2[(\phi_j^s - \phi_{j,l}) - \frac{\pi}{2}]\cos^2(\theta_j^s) \tag{4.4}$$

where ϕ_j^s is the satellite azimuth, $\phi_{j,l}$ is the relative azimuth w.r.t. aiding agent, and θ_j^s is the satellite elevation [12]. Several approximations lead to the definition of (4.4). The most relevant is the assumption of perfect steering vector estimations, leaving pseudorange error as the only noise source. Within this framework, however, a similar simplification is too optimistic. As deeply discussed in Section 2.4, the steering vector estimation and its drawbacks play a significant role in the positioning error of a realistic IAR algorithm implementation.

Regarding the value of $\sigma_{\rho\hat{I}}$, the decision to assign the maximum correlation between IAR and pseudorange reduces dramatically the role of the Inter-agent range in providing position information. However, the analytical derivation of a closed form for this covariance is not possible in this context.

In view of the absence of approximated formulas for the elements of $\mathbf{R}_I$ and $\mathbf{R}_{\rho I}$, a Monte Carlo simulation is exploited to achieve a refinement of (2.19). Approximations of $\sigma_{\hat{I}}^2$ and $\sigma_{\hat{I}\rho}$ can be thus derived through an empirical optimization procedure. A valuable strategy is to base the elements of the matrix on their respective upper bounds, by fixing a proper weight coefficient. To this aim is convenient to use a *weight matrix* $\mathbf{W}_{UB}$ and a matrix $\bar{\mathbf{R}}_{UB,k}$ that contains all the upper bounds of the measurement covariance matrix, such that

$$\bar{\mathbf{R}}_k = \mathbf{W}_{UB} \circ \bar{\mathbf{R}}_{UB,k} \tag{4.5}$$

where the symbol "$\circ$" denotes the *Hadamard product* or *entrywise product*, i.e. the matrices are multiplied element-by-element.

The definition of the weight matrix affects the complexity of the optimization procedure. The elements $\sigma_{\hat{I}}^2$ and $\sigma_{\rho\hat{I}}$ of the covariance matrix are obviously dependent on the random variables involved in the determination of $\hat{I}_{jl}^s$ and, more notably, on the geometry generated by the involved agents and satellite. It follows that each entry of the sub-matrices $\mathbf{R}_I$ and $\mathbf{R}_{\rho I}$ is dependent on the specific couple of agents considered and on the common satellite. As a consequence, the optimal weights should be different for each entry of the matrix. Therefore these coefficients should be adaptive, in order to approximate with sufficient precision the correspondent variance and covariance. An analytical approximation of the covariance formula is indeed a more valuable and adaptive approach and it will be investigated in further research.

The optimal weight for each upper bound in $\bar{\mathbf{R}}_{UB,k}$ can be derived exploiting the Monte Carlo simulation, but obtaining a joint optimization for each single entry of matrix $\mathbf{W}_{UB}$ would not be cost-effective in terms of computational burden. Therefore some simplifications are introduced, that eventually lead to a weight matrix with a more general validity. The same weight coefficient α_1 is assigned to all the IAR variances upper bounds. Similarly, a single coefficient α_2 regulates the weight of the covariance bounds. According to these assumptions, the definition of the weight matrix is

$$\mathbf{W}_{UB} = \left(\begin{array}{c|c} \mathbf{W}_\rho & \mathbf{W}_{\rho I} \\ \hline \mathbf{W}_{\rho I} & \mathbf{W}_I \end{array}\right) = \left(\begin{array}{cccc|cccc} 1 & 0 & \cdots & 0 & \alpha_2 & \alpha_2 & \cdots & \alpha_2 \\ 0 & 1 & \ddots & \vdots & \alpha_2 & \alpha_2 & \cdots & \alpha_2 \\ \vdots & \ddots & \ddots & 0 & \vdots & \vdots & \ddots & \vdots \\ 0 & \cdots & 0 & 1 & \alpha_2 & \alpha_2 & \cdots & \alpha_2 \\ \hline \alpha_2 & \alpha_2 & \cdots & \alpha_2 & \alpha_1 & 0 & \cdots & 0 \\ \alpha_2 & \alpha_2 & \cdots & \alpha_2 & 0 & \alpha_1 & \ddots & \vdots \\ \vdots & \vdots & \ddots & \vdots & \vdots & \ddots & \ddots & 0 \\ \alpha_2 & \alpha_2 & \cdots & \alpha_2 & 0 & \cdots & 0 & \alpha_1 \end{array}\right) \tag{4.6}$$

Eventually, in order to obtain a good approximation of $\sigma^2_{\hat{I}}$ and $\sigma_{\hat{I}\rho}$, the optimal parameters to seek for are the coefficients α_1 and α_2. The optimization criteria focus on the minimization of the positioning error norm e_p. In particular, two optimal weight matrices $\mathbf{W}_{UB}$ are derived, depending on the optimization criterion: one minimize μ_{e_p} and another correspond to a minimum σ_{e_p}.

Actually in this context, a more general approach to the determination of optimal weights is pursued. The optimization criteria are set to provide broader results, minimizing the standard deviation and the average position error of the entire network ($\mu_{\mathcal{N}}$ and $\sigma_{\mathcal{N}}$), in order to obtain a solution that is independent from a specific trajectory or visibility conditions. This strategy represents another approximation for the resulting measurement model, accepted in the tentative to obtain a $\mathbf{W}_{UB}$ suited to the majority of cases, while preserving a reasonable computational cost.

The simulation carried out to support the optimization process is performed over a random network of 30 agents, where the network positioning error is measured through $\mu_{\mathcal{N}}$ and $\sigma_{\mathcal{N}}$ for each combination of weight coefficients α_1 and α_2. In order to summarize the positioning error performance in a single value for each tested $\mathbf{W}_{UB}$, some assumptions must be done. A practical choice is to observe several realizations of the system performance metrics at a fixed time (snapshot) and collect them for each configuration of the weight matrix. The problem of the choice of the proper time instant arises: after some time the system is more influenced by the parameter and its effects are more visible. Thus a snapshot after a sufficiently long outage should be chosen as a valuable instant in which evaluate the positioning error. However, after a long outage period the estimated IAR heavily deteriorates and this could lead to an over-conservative optimization for the weights in $\mathbf{W}_I$, assigned to IAR variances, since IAR measurements are poorly precise after such a long time. In view of these issues, a reasonable time snapshot of 10 seconds has been chosen to perform the simulation.

The outcome of the joint optimization are summarized in Figure 4.10 and 4.11, where the results of both optimization criteria are shown. From the experiment the optimal value of the weight coefficients obtained are

$$\begin{aligned} \alpha_1 &= 1 \\ \alpha_2 &= -0.067 \ . \end{aligned}$$

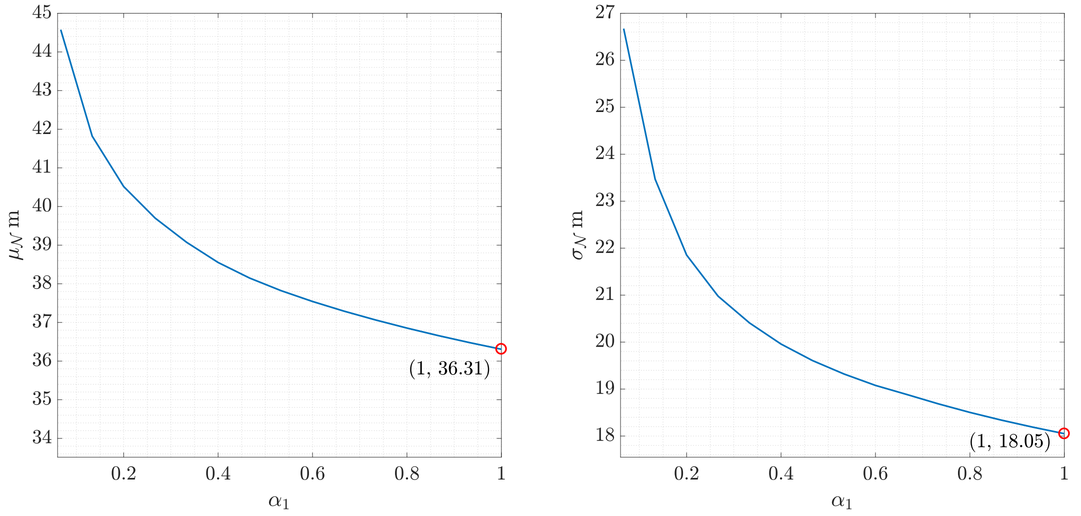

(a) Network mean position error

(b) Network STD position error

Figure 4.10: Network position error versus α_1. The position error norm e_p of each GNSS-denid agent is collected after 10 seconds of outage. Statistical properties (mean and STD) of e_p are evaluated and averaged over the $|\mathcal{D}_k|$ agents in the network. Coefficient α_2 is fixed at its optimal value.

for the minimum μ_{e_p} criterion, and

$$\begin{aligned} \alpha_1 &= 1 \\ \alpha_2 &= 0.2 \ . \end{aligned}$$

for the minimum σ_{e_p} criterion. It can be noted that the coefficient α_1, applied on variance upper bound, minimizes on average both the standard deviation and the mean value of the position error norm e_p, as it can be seen from Figures 4.10a and 4.10b. The optimal coefficient α_2 is instead slightly different w.r.t. the two criteria. However, in order to provide an overall good performance, it will be assumed $\alpha_2 = 0$ as a general optimal coefficient.

The outcomes of this optimization have clear meanings. Optimal diagonal coefficients of sub-matrix $\mathbf{W}_I$ force the values of each $\sigma_{\hat{I}}$ to be equal to their upper bounds. Therefore a cautious integration of IAR measurements is encouraged, probably due to the fast deterioration that these ranges experience, as extensively discussed in Section 2.4. The optimal value of coefficient α_2 results in a model with no correlation among IAR measurements and the pseudoranges on which they are based. This is obviously not true, but still α_2 is the value that minimizes both position error variance and mean. As discussed, the IAR estimate is influenced by several random variables, both from current and past time instants. It is possible that with this complex dependency relationships, the specific influence of ρ_j^s on the random variable $\hat{I}_{jl}^s$ tends to approach negligible values, that are not observed with the limited granularity of the above experimental optimization.

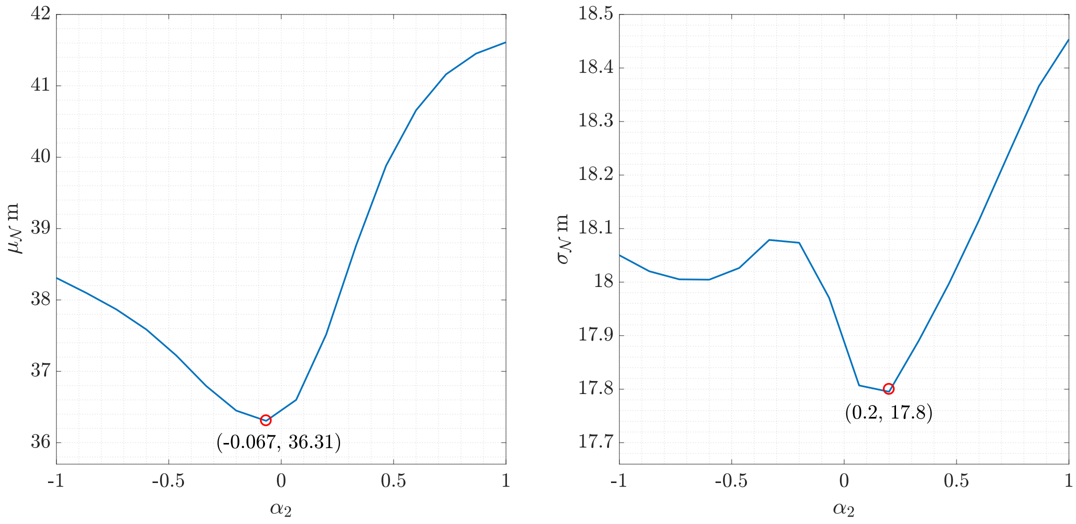

(a) Network mean position error

(b) Network STD position error

Figure 4.11: Network position error versus α_2. The position error norm e_p of each GNSS-denid agent is collected after 10 seconds of outage. Statistical properties (mean and STD) of e_p are evaluated and averaged over the $|\mathcal{D}_k|$ agents in the network. Coefficient α_1 is fixed at its optimal value.

The optimal weight matrix retrieved has been added to the network simulation as a general parameter. The resulting positioning error is compared to the curves of Figure 4.2.

The optimized $\mathbf{W}_{UB}$ is clearly able to improve the positioning performance of the preliminary implementation. The enhancement of performance is present for both version of the predictive stage as well as for both μ_{e_p} and σ_{e_p}. However, for the selected trajectory, this kind of network-wise tuning of parameters is not sufficiently accurate to attain the position error levels of a non-cooperative, EKF-based, PVT. The weighting of the upper bounds through a constant coefficient is a heuristic solution that represents a valuable fine-tuning approach to the refinement of the measurement model of the IAR method, but the algorithm still needs some refinements as long as an analytical approximation of the true measurement covariance matrix is not available.

4.3.2 Error Covariance Matrix Heuristic

From preliminary results an important drawback of a coarse measurement model was observed: the biased position estimate produced during an outage period, when additional ranges were integrated, is propagated over the subsequent epochs for a considerable time. The erroneous behavior is particularly visible when compared to non-cooperative positioning. In this last case the estimate is much less anchored to past estimations after an outage.

In the EKF routine, the Kalman gain $\mathbf{K}_k$ acts as a blending factor [20], that “balances”

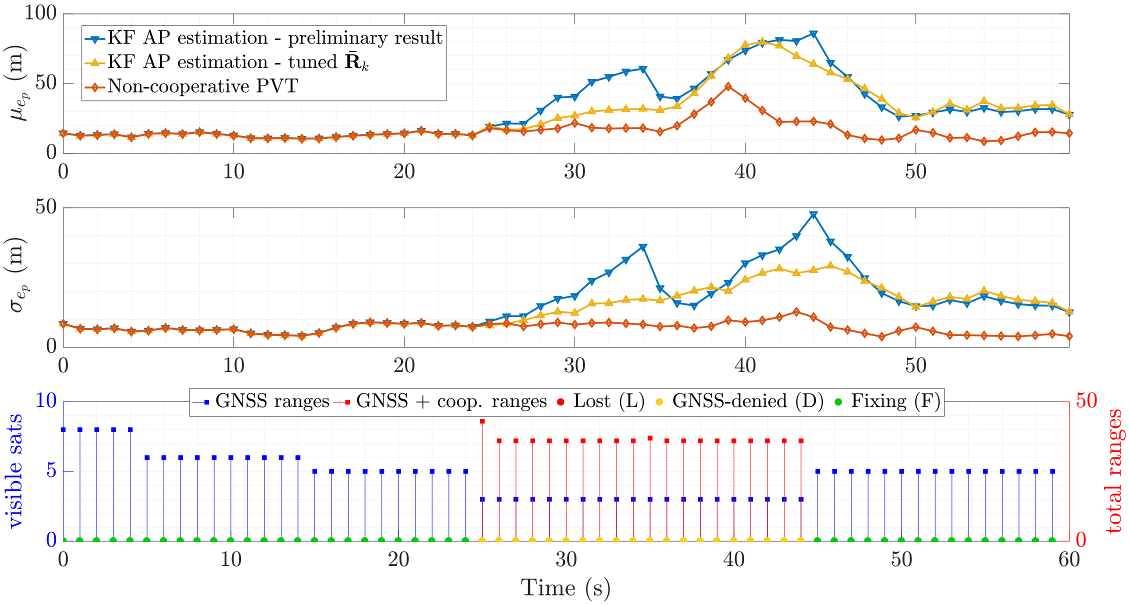

Figure 4.12: Position error statistic. Average and STD of position error norm resulting from IAR algorithm with KF predictive stage are shown along with visibility states progression.

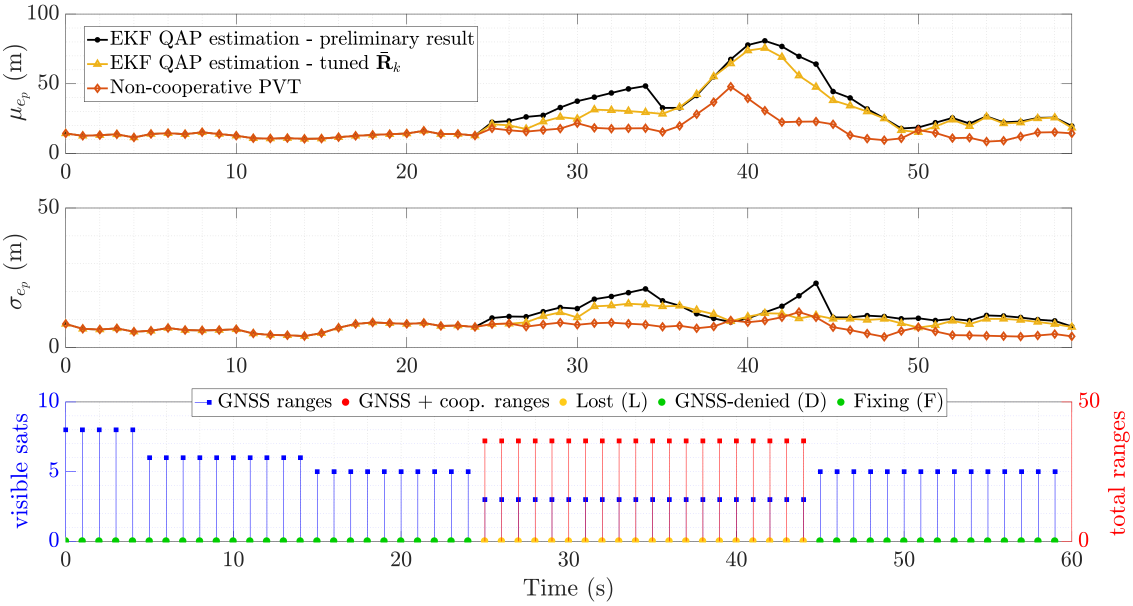

Figure 4.13: Position error statistic. Average and STD of position error norm resulting from IAR algorithm with EKF predictive stage are shown along with visibility states progression.

the importance given to current measurements w.r.t. the a priori estimate, to output an updated state estimate that is optimal. The Kalman gain is optimal in the sense that minimizes the individual terms along the major diagonal of the error covariance matrix $\mathbf{P}_k$ [20]. Recalling basic Kalman filter's theory [20], the error covariance matrix associated to state $\hat{\mathbf{x}}_{A,k}$ is

$$\mathbf{P}_k = \mathbf{E}[(\mathbf{x}_{A,k} - \hat{\mathbf{x}}_{A,k})(\mathbf{x}_{A,k} - \hat{\mathbf{x}}_{A,k})^\top] \, . \tag{4.7}$$

The confidence in state estimate is regulated by the error covariance matrix $\mathbf{P}_k$ that contains the information about the state error. On the basis of its projection $\mathbf{P}_k^-$ and of the measurement covariance matrix $\bar{\mathbf{R}}_k$, the Kalman gain regulates the filter's use of the a priori state and the current measurements (Section 2.1). Therefore, although the two covariance matrices $\bar{\mathbf{R}}_k$ and $\mathbf{P}_k$ are not independent (2.17), the error covariance matrix $\mathbf{P}_k$ have an indirect role in the importance given to cooperative ranges.

When additional ranges are integrated, the output state estimate is based on many observations and the error covariance matrix is updated accordingly: if the additional ranges are far from the model expectations, an erroneous confidence on this state estimate may be promoted through the matrix $\mathbf{P}_k$. This is the main reason that causes cooperatively-obtained positions to negatively influence the position error even when the regular GNSS visibility (F state) has been recovered (Figures 4.2, 4.5 and 4.5).

This misleading behavior is well described by Figure 4.14, where the evolution of the matrix $\mathbf{P}_k$ is represented, as observed along the path analyzed in the second case-study (Sec. 4.2.2). In order to synthesize the configuration of (4.7) in a single value, the square root of the trace of the matrix is taken at each time instant k and showed in the graph.

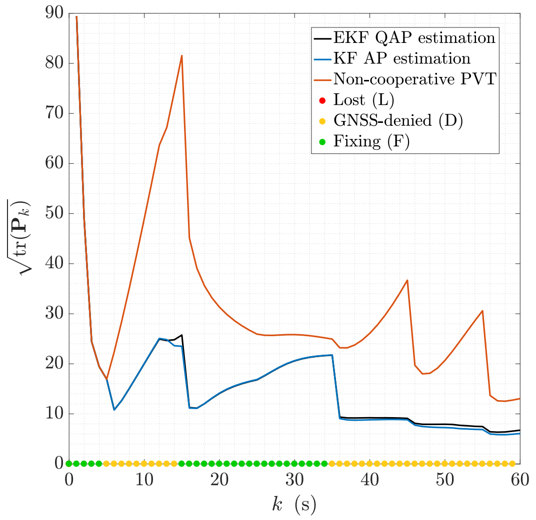

Figure 4.14: Time evolution of $\sqrt{\mathrm{tr}(\mathbf{P}_k)}$. Different a priori estimation techniques are compared to the non-cooperative case.

By looking at the curve relative the non-cooperative case, several spikes can be observed (besides the initial transient) in correspondence to the time windows where the GNSS service is partially denied (D state). A peak of $\sqrt{\mathrm{tr}(\mathbf{P}_k)}$ means that the Kalman filter associates high variances to the elements of the state $\hat{\mathbf{x}}_{A,k}$. As a consequence, the state $\hat{\mathbf{x}}_{A,k}$ will be cautiously considered when computing the next state estimate $\hat{\mathbf{x}}_{A,k+1}$. In the case of the two curves related to cooperative PVT, these peaks are heavily smoothed. This means that more trust will be granted to state $\hat{\mathbf{x}}_{A,k}$ when the next state will be estimated. However if this $\sqrt{\text{tr}(\mathbf{P}_k)}$ reduction does not correspond to a real increase in the reliability of $\hat{\mathbf{x}}_{A,k}$, the next filter output will be misled.

A heuristic solution to this issue is to force the error covariance matrix to account only for legacy GNSS measurements, without considered the additional ranges, even if the latter are still integrated in the PVT computation. This is a less elegant solution with respect to act directly on the measurement model by refining the measurement noise covariance matrix $\bar{\mathbf{R}}_k$. In fact, this countermeasure would be unnecessary if the measurement model included a sufficiently good approximation of the true measurement noise covariance matrix. In fact, $\bar{\mathbf{R}}_k$ is involved in $\mathbf{P}_k$ determination, thus a proper refinement of $\bar{\mathbf{R}}_k$ will produce also a less erroneous error covariance matrix. However, since non-modeled characteristics are at the origin of EKF sub-optimality, this heuristic may be a valuable solution to stem the effects of the residual lack of modeling.

The scenario analyzed in the first case-study (Sec. 4.2.1) is here proposed again to show the evolution of an estimated trajectory resulting from the application of this countermeasure. The benefits of this solution are clearly visible. The estimation is able to provide a

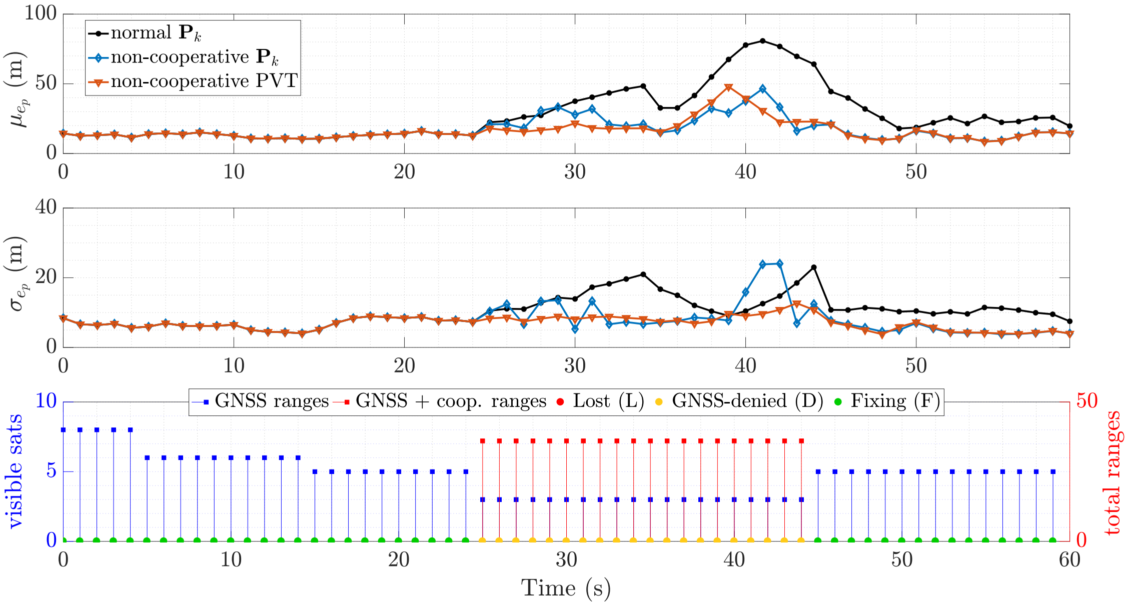

Figure 4.15: Position error statistic. Position errors obtained through IAR positioning that employs a $\mathbf{P}_k$ matrix propagated as in the non-cooperative case are compared to plain IAR positioning and non-cooperative positioning error curves. IAR positioning outcomes use EKF QAP estimation.

better positioning after an outage event, giving a position estimate that is comparable to the one provided by a non-cooperative PVT, both on average and w.r.t standard deviation.

The same outcome is illustrated by the trajectory plots of Figure 4.16.

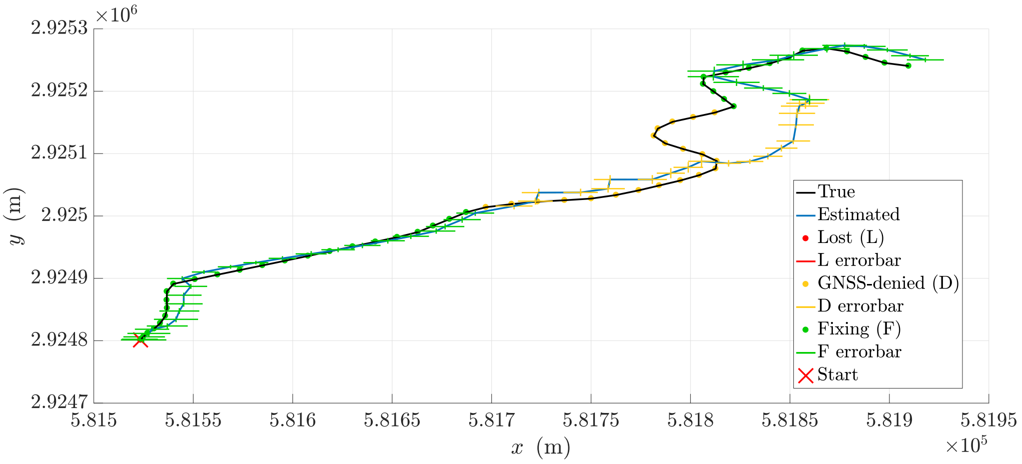

(a) $\mathbf{P}_k$ normal

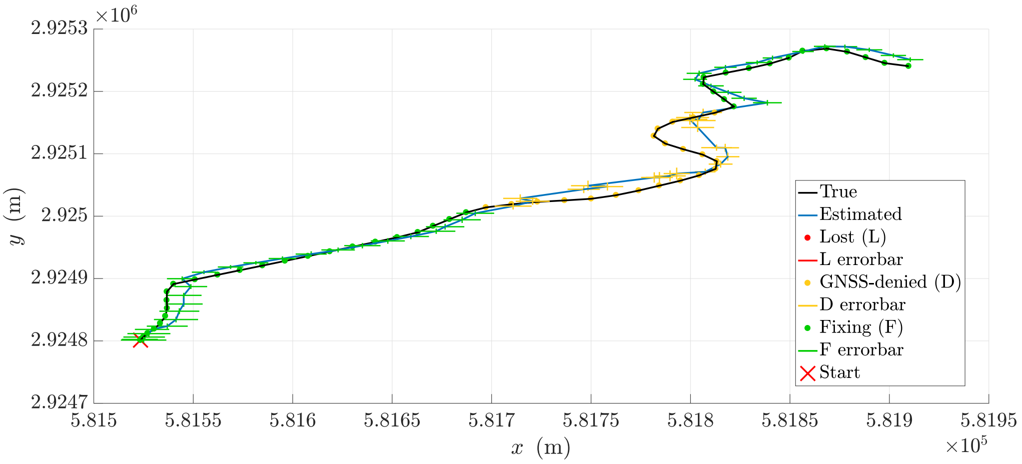

(b) $\mathbf{P}_k$ updated as in non-cooperative PVT

Figure 4.16: Simulated trajectories w.r.t. $\mathbf{P}_k$ update methods. Agent's path observed for 60 seconds. Visibility states are highlighted. The IAR cooperative algorithm is implemented using the EKF quasi-a-priori estimation

The propagation of bias (and variance) is now massively reduced and the estimated trajectory is closer to its true value during the outage period. This improvement is generally experienced by the entire network, as described in Figure 4.17, reported here to observe the general validity of this method. Despite this, the plain GNSS solution still provides more accurate state estimations both in general (Figure 4.17) and w.r.t. the considered path realization (Figure 4.15).

The two countermeasures to measurement model sub-optimality discussed so far are simultaneously exploited to assess possible further performance improvements. The results of these experiments are shown in Figures 4.19 and 4.18, where they are compared to the single techniques for the algorithm's improvement applied in isolation. Positioning

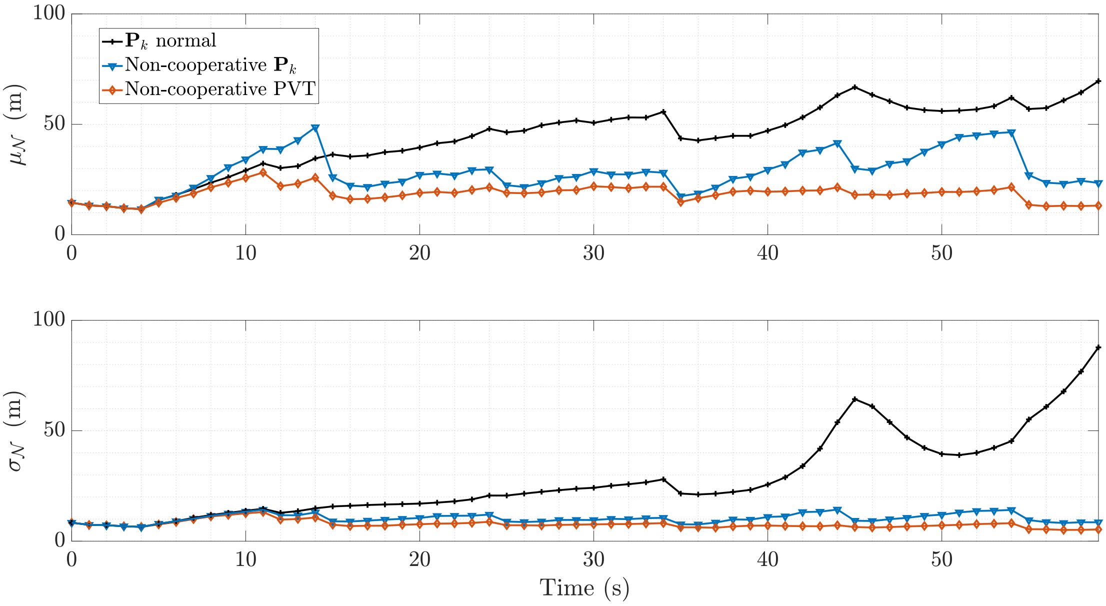

Figure 4.17: Network position error statistic. Network-wise average norm of the position error. $\mathbf{P}_k$ matrix propagation management techniques are compared. EKF QAP estimation employed.

errors are generally reduced and it is possible to recognize the combined effect of the two techniques: a generally reduced error thanks to the model's refinement and curves that are able to recover from the performance worsening caused by the outage period. However the adjustments are less effective when KF is employed in IAR's predictive stage, confirming this version of the algorithm as the less performant in terms of estimated position error.

The combined use of the two techniques is illustrated also by the two trajectories drawn in Figure 4.20, reported here as a reference for the improvements achieved so far.

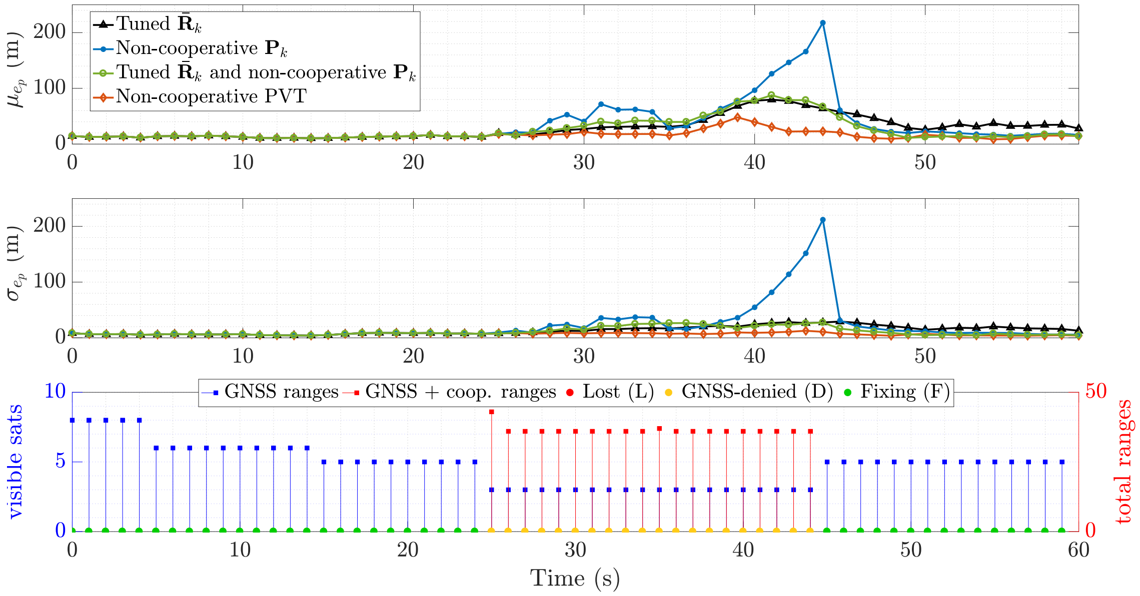

Figure 4.18: Position error statistic. Position errors obtained through non-cooperative $\mathbf{P}_k$ matrix propagation and $\bar{\mathbf{R}}_k$ matrix refinement compared. IAR positioning outcomes use KF AP estimation.

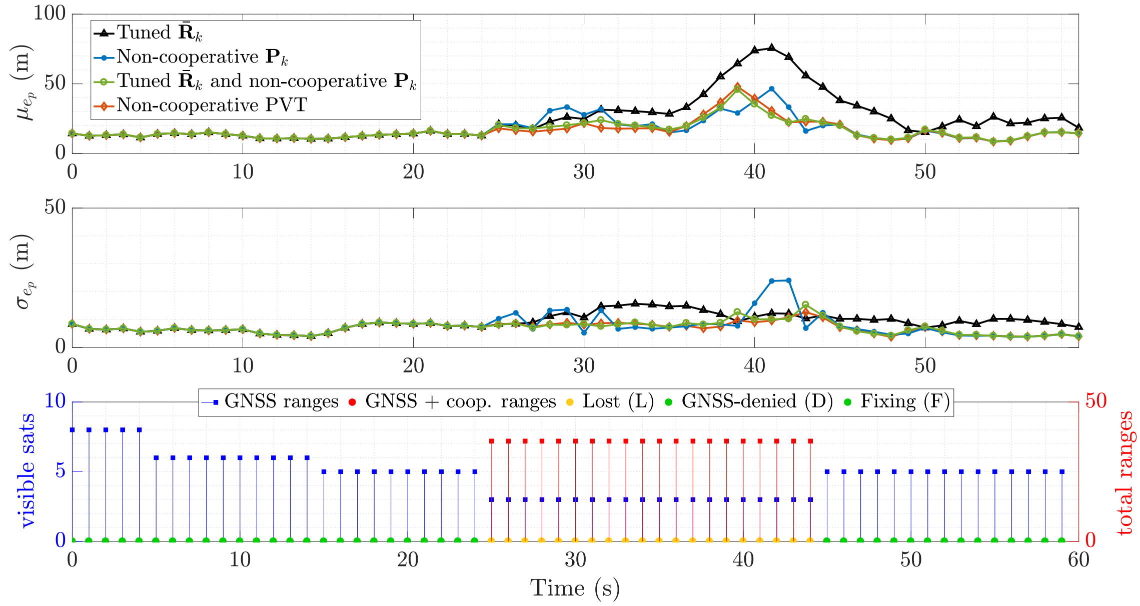

Figure 4.19: Position error statistic. Position errors obtained through non-cooperative $\mathbf{P}_k$ matrix propagation and $\bar{\mathbf{R}}_k$ matrix refinement compared. IAR positioning outcomes use EKF QAP estimation.

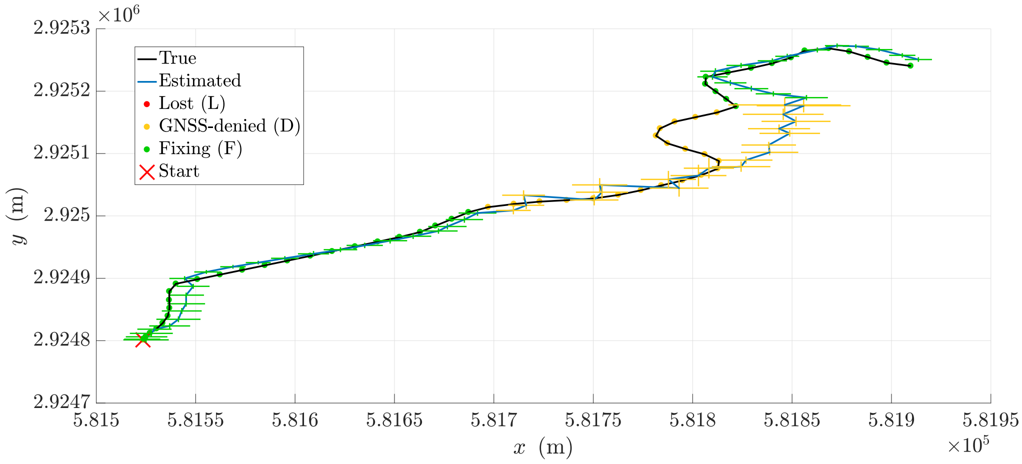

(a) KF AP estimation

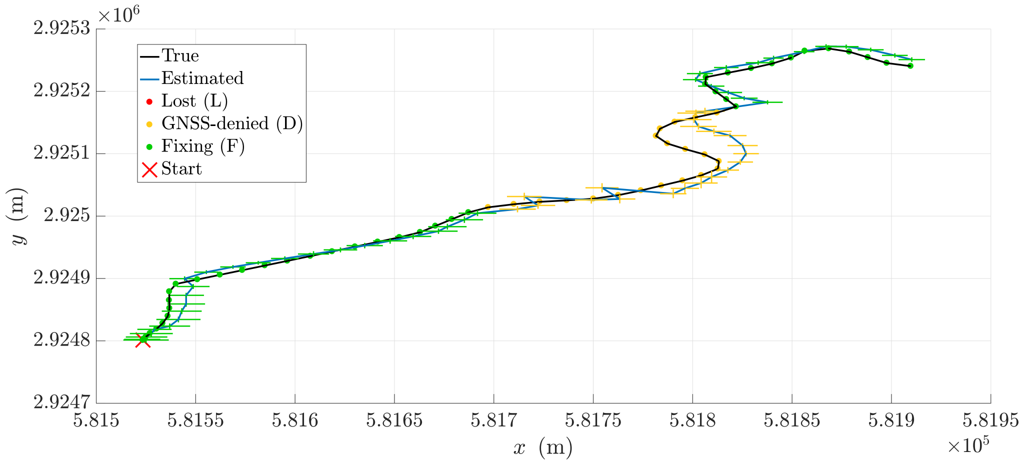

(b) EKF QAP estimation

Figure 4.20: Simulated trajectories. Agent's path observed for 60 seconds. Positions estimated using the refined $\bar{\mathbf{R}}_k$ matrix model and non-cooperative $\mathbf{P}_k$ matrix propagation.

4.3.3 IAR Selective Filters

The previous sections were devoted to the management of the additional measurements integrated in the PVT routine performed by the aided agent. By means of a model refinement and an error covariance matrix propagation strategy, the cooperative ranges are integrated in the positioning algorithm in order to efficiently take advantage of the information carried by these additional measures. However, several issues still affect the inter-agent ranges (bias, non-modeled effects) and, despite the tuning effort made so far, the policy of integrating as many observations as possible may not be a successful approach for these kind of measurements. In particular, non-modeled effects arisen from a sub-optimal measurement characterization in the EKF, are as more harmful as the number of IAR contributions included in the PVT increases. Therefore, a selection strategy applied on the retrievable cooperative ranges may be wiser than an unconditional IAR inclusion. Moreover in a crowded hot-spot, several IARs are available for a networked GNSS receiver, thus a selective approach may be even more effective.

The problem of which measurements should feed the PVT computation has not been addressed yet and a decision rule is needed in order to select a valuable set of contributions. An obvious criterion is minimizing the difference between the inter-agent range estimate $\hat{I}^s_{jl}$ and its true value I^s_{jl}, i.e. minimizing the IAR error. However, this decision rule requires a knowledge at the aided agent j of the real euclidean distance from the aiding agents, in which case the whole IAR retrieval process would be pointless. Hence, a decision rule that can be performed exploiting the information available for agent j is needed. To this aim, three selection strategies of the cooperatively-obtained measurements are presented in the current section. An aggregation policy of the set of IAR is discussed as well.

The effectiveness of these management techniques, from now on referred to as *IAR filters*, is evaluated from a network perspective. The refined Kalman measurement model, derived in previous sections, acts on each single range integration, whereas IAR filters work on an aggregated set of measurements. As a consequence, a study focused on a single trajectory would provide a poor statistic in this sense. In fact, although it is characterized by several realizations of the measurement noise (Section 3.1.2), many characteristics of a specific I^s_{jl} retrieval, that will be exploited for discrimination (such as the geometry of the agents and satellite involved), are repeated across the realizations of a specific path. For these reasons it is convenient to assess the influence of IAR filtering policies on positioning errors through an aggregated network metric. In particular, the usual statistical characteristics of position error norm (μ_{e_p} and σ_{e_p}) of each agent are averaged among all the agents in the network at each fixing epoch and the resulting metrics $\mu_{\mathcal{N}}$ and $\sigma_{\mathcal{N}}$ are observed.

Minimum Variance Criterion

The IAR approximated variance formula (4.4) was already recalled in this chapter when dealing with the optimization of $\bar{\mathbf{R}}_k$. In that context (4.4) was considered an excessive approximation for achieving a fine-tuning of the measurement model. Within the assessment of a selection strategy, however, this can be a valuable starting point for a qualitative skimming of the worst measurements.

Cooperative ranges that exhibits the lowest IAR variances according to (4.4) are chosen for the EKF tight integration. The quantity of additional ranges selected in this way allows the agent to reach a total of exactly 4 measurements, at each fixing epoch. This is done to support EKF convergence[1], while being strictly selective on the quantity of measurements integrated and clearly observe the effects of filtering.

The results from the application of this decision rule are reported in Figure 4.21 and compared with the average network performances of a non-selective integration of cooperative ranges. As foreseen, the selective policy has produced improved results. Moreover, the overall variance is reduced, in coherence with the criterion applied, even if (4.4) is a strong approximation.

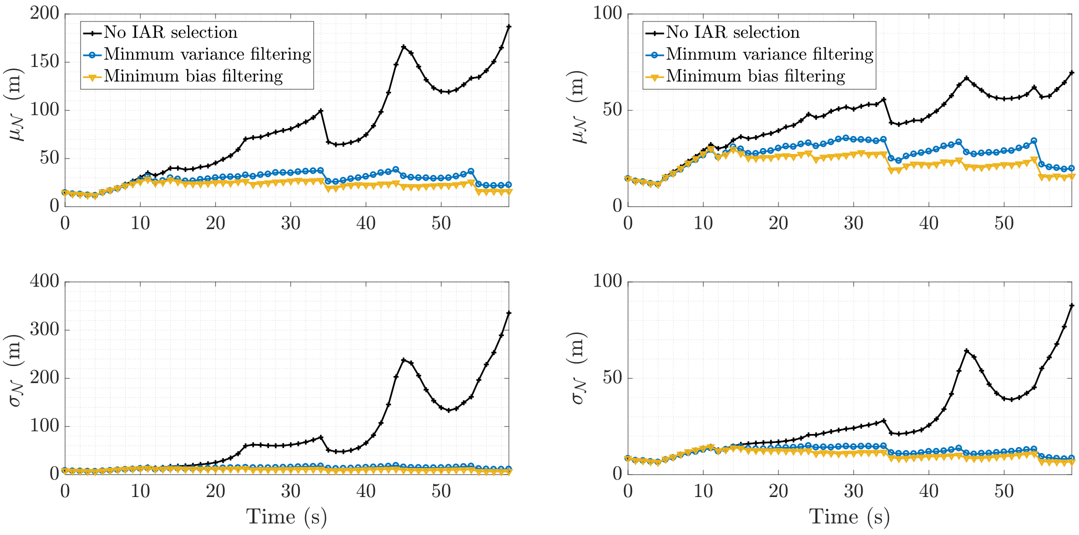

(a) KF AP estimation (b) EKF QAP estimation

Figure 4.21: Network position error statistic with minimum variance and bias filtering. $\mu_{\mathcal{N}}$ and $\sigma_{\mathcal{N}}$ are the network averages of μ_{e_p} and σ_{e_p} respectively.

A compact way to look at the average performances of the network is by observing the *empirical cumulative distribution function* (empirical CDF). Empirical CDFs based on the same datasets used for the plots in Figure 4.21 are drawn in Figure 4.22. From Figure 4.22 it is possible to confirm the strong reduction of positioning error when the filter is on. In the 90% of the cases[2], the positioning error changes from values around 100 m to values around 60 m, in the right panel. For what concern the KF AP estimation (left panel) the reduction is even more effective: the 90% of position errors go from 120 m to 60 m, reducing the performance gap between the two a priori estimation techniques.

---

[1] With at least 4 measurements the solution of the trilateration equations is guaranteed.

[2] The empirical CDF is based on a dataset that contains the position error norm e_p of all the agents in the network for the entire observation time and for all the simulated realizations of the process.

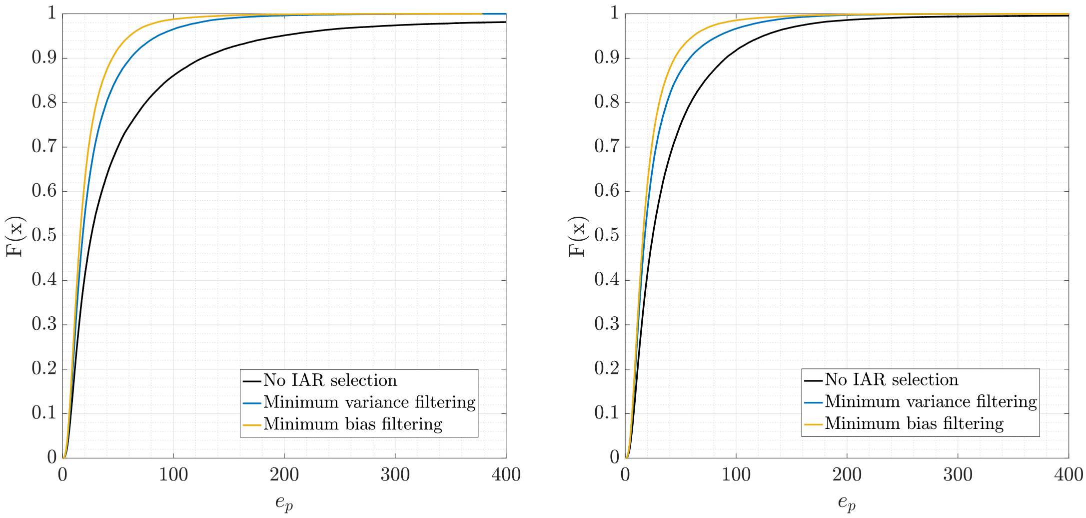

(a) KF AP estimation (b) EKF QAP estimation

Figure 4.22: Empirical cumulative distribution function of average network position error with minimum variance and bias filtering.

Minimum Bias Criterion

The results obtained in [12] can be exploited here to derive another filtering criterion. In this work from Minetto an interesting empirical result is illustrated: the average IAR error μ_{e_I} (i.e. the bias related to the IAR estimator $\hat{I}^{s}_{jl}$) tends to be minimum in accordance to the geometries where the variance is maximum. The variance exhibited by the IAR under these geometrical conditions is coherent with (4.4) and is empirically demonstrated in [12].

As a consequence, another possible decision rule to retrieve a selected set of cooperative ranges may favor the minimization of bias, by selecting the triplets (agent j, agent l and satellite s) that maximize (4.4). Again, the number of additional measurements selected in this way is reduced to the essentials. The outcomes of this selection strategy are summarized in Figures 4.21 and 4.22 too.

As expected, a reduction of the network mean position error $\mu_{\mathcal{N}}$ is visible (Figure 4.21), since the IAR integrated are the ones that minimize the estimated IAR bias. However, more surprisingly, the position error reduction is observed also on $\sigma_{\mathcal{N}}$ curve, but it should be remembered that this is a qualitative evaluation based on an approximated formula, some unpredicted effects may arise. In the end an overall improvement is assessed with this selective criterion and positioning errors are below 50 m for the 90% of cases (Figure 4.22).

Multiple IAR Averaging

It was already mentioned (Section 1.2) that between a given couple of cooperating agents, more than one IAR can be obtained by the aided agent if more than one satellite is shared with the aiding peer. These *multiple IARs* represent an estimate (computed under different conditions) of the same euclidean distance. This multiplicity foster the aggregation of these measurements by averaging them, in order to build a more robust estimation of the euclidean distance.

This technique is applied to the network considered in previous sections and the aggregated results are summarized in Figures 4.23 and 4.24.

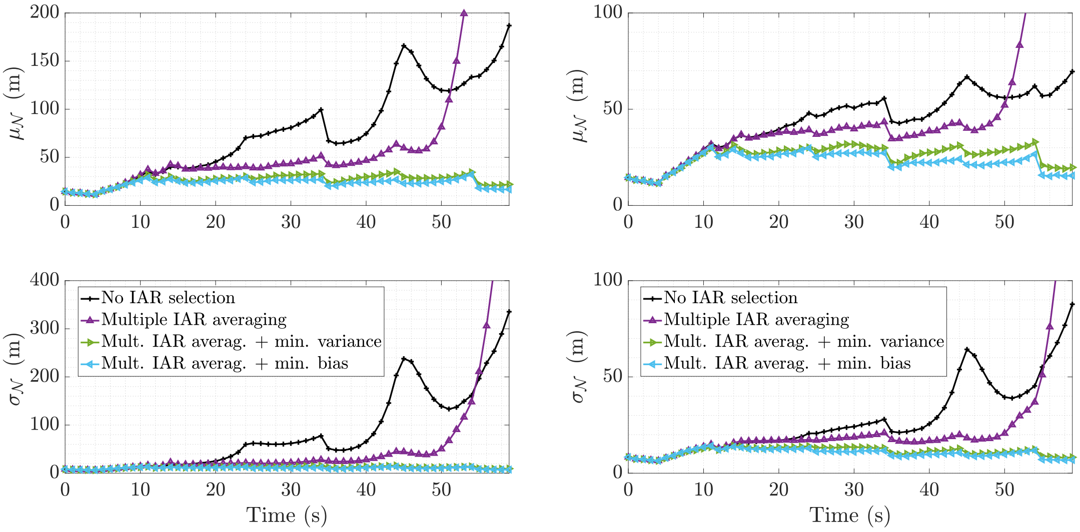

(a) KF AP estimation (b) EKF QAP estimation

Figure 4.23: Network position error statistic with composite selective filtering. $\mu_{\mathcal{N}}$ and $\sigma_{\mathcal{N}}$ are the network averages of μ_{e_p} and σ_{e_p} respectively.

The advantages w.r.t. to the unfiltered integration are limited, especially if compared to the improvements achieved with the other selection criteria previously tested (Figures 4.21 and 4.22). It should be noticed however that this aggregation technique average the set of $\hat{I}^s_{jl}$ retrieved by a collaborating couple, providing one (averaged) contribution for each aiding agent integrated in the hybrid PVT. As a result, no discrimination is applied on the choice of the aiding agent. Therefore with this implementation, the problems related to the inter-agent ranges abundance (Sec. 4.2.3) are not overcome anymore. Hence, an additional technique is needed to further reduce the number of integrated cooperative measurements through a wise selection of collaborating agents.

A good idea is to merge the discussed methods in one composite selective strategy: the averaging of multiple IARs is applied in order to choose a single $\hat{I}^s_{jl}$ for each cooperating peers' couple, then the best aiding agents are selected either by using the minimum variance criterion or the minimum bias criterion[3]. Essentially the multiple IAR filter acts on satellites shared by a given couple of agents, while one of the two already discussed filters

---

[3] Tho choose the best aiding agent, a satellite s must be chosen for the computation of (4.4). Since the resulting IAR is the outcome of averaging, the satellite can be chosen arbitrarily among the shared

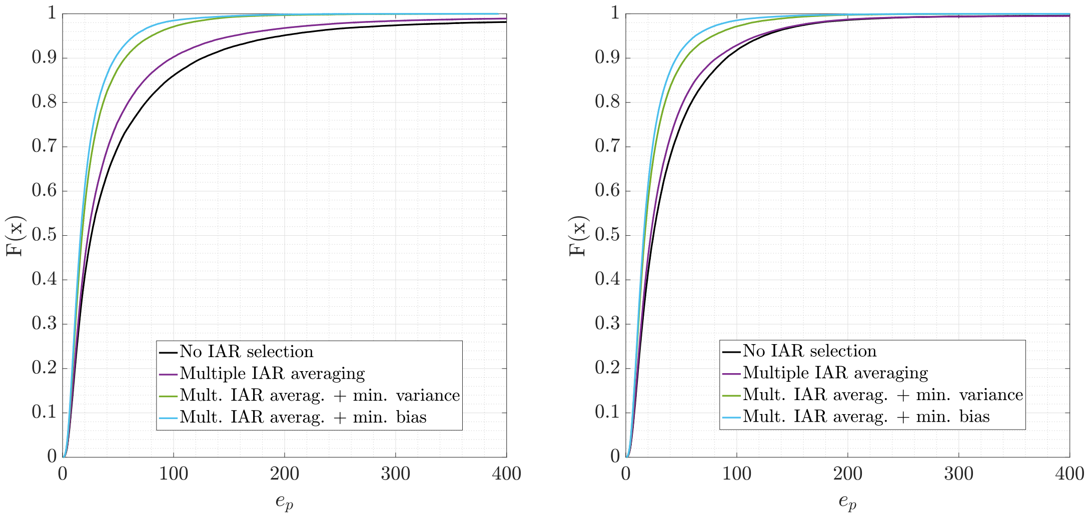

(a) KF AP estimation

(b) EKF QAP estimation

Figure 4.24: Empirical cumulative distribution function of average network position error with minimum variance and bias filtering.

(minimum variance or minimum bias) acts on the peer couples in order to choose the best aiding agent for a given aided user.

The composite IAR filtering techniques give high positioning performances that are summarized, along with the plain multiple IAR averaging method, in Figures 4.23 and 4.24. A significant improvement can be easily inferred by looking at the empirical cumulative distribution function of the EKF QAP estimation version (Figure 4.24b): from a value of 80 m (90% probability) with the plain multiple IAR averaging aggregation, the position error e_p is reduced up to less than 50 m (90% probability), when the combined filtering with the minimum bias criterion is applied. Similar results are obtained with the KF AP estimation version of the algorithm, although even bigger enhancement are observed (Figure 4.24a).

Minimum aiding agent's position error criterion

The effects of an unreliable estimated position of an aiding peer on the IAR error were already illustrated in Section 2.4.3, discussing the impact of non-accurate estimation of the steering vector $\mathbf{h}_B^s$ involved in IAR computation. It was shown that a wrongful estimation of the aiding agent's position will increase the IAR error. It is then straightforward to provide here a filtering policy based on the reliability of the estimated position of the generic aiding agent l. Notice that, since this criterion can be applied only on an agent's

---

ones. To this purpose, the satellite that gives the best result of (4.4) is chosen for the discrimination among aiding agents.

position basis, an additional decision rule is necessary to obtain a single $\hat{I}^s_{jl}$ for each couple of collaborating peers. To this purpose, the averaging of multiple IAR is employed.

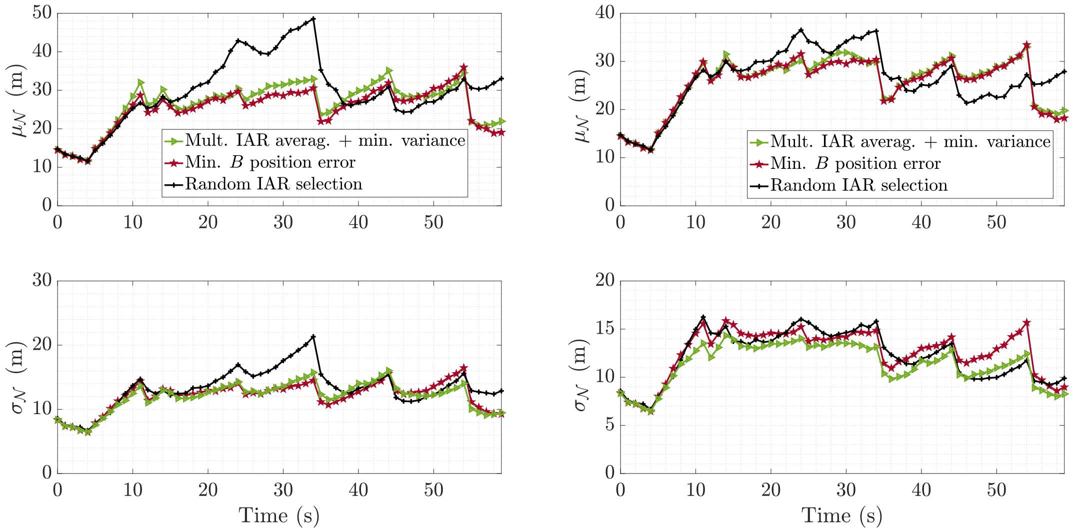

(a) KF AP estimation (b) EKF QAP estimation

Figure 4.25: Network position error statistic with filtering based on aiding agent position error. $\mu_{\mathcal{N}}$ and $\sigma_{\mathcal{N}}$ are the network averages of μ_{e_p} and σ_{e_p} respectively. “Random IAR selection” refers to a random selection of IAR to be integrated in the PVT.

The benefits derived from this technique are illustrated by Figures 4.25 and 4.26. The behavior is very similar to the results provided by the application of the combined minimum variance criterion, but generally slightly better. Actually this does not hold for the curves related to $\sigma_{\mathcal{N}}$ (Figure 4.25), where the minimum variance criterion is still more effective.

At this point, after observing the analogies among the outcomes produced by the IAR filtering methods, one may think that the benefits obtained by the system may be due to the bare reduction of cooperative ranges integrated in the PVT. As repeatedly underlined in fact, a reduction of the number of IAR in the measurements set of the positioning algorithm, implies a reduction of non-modeled effects and consequently of EKF sub-optimality.

The advantages of a bare reduction of measurements are indeed visible in Figure 4.26, where the results of a random IAR selection are shown and compared to the unfiltered case. However the same picture highlights the advantages of a wise discrimination policy of cooperative contributions, since the described criteria overcome the improvements derived from a random IAR selection (visible also in Figure 4.25).

Finally, a further comparison among the best performing IAR filters is here provided in order to understand which discrimination criteria generally provide the lowest positioning errors. The best filtering techniques will be then implemented in combination with other algorithm’s improvements, in the next section on final results.

Minimizing the bias according to results in [12] is empirically proven to be the best

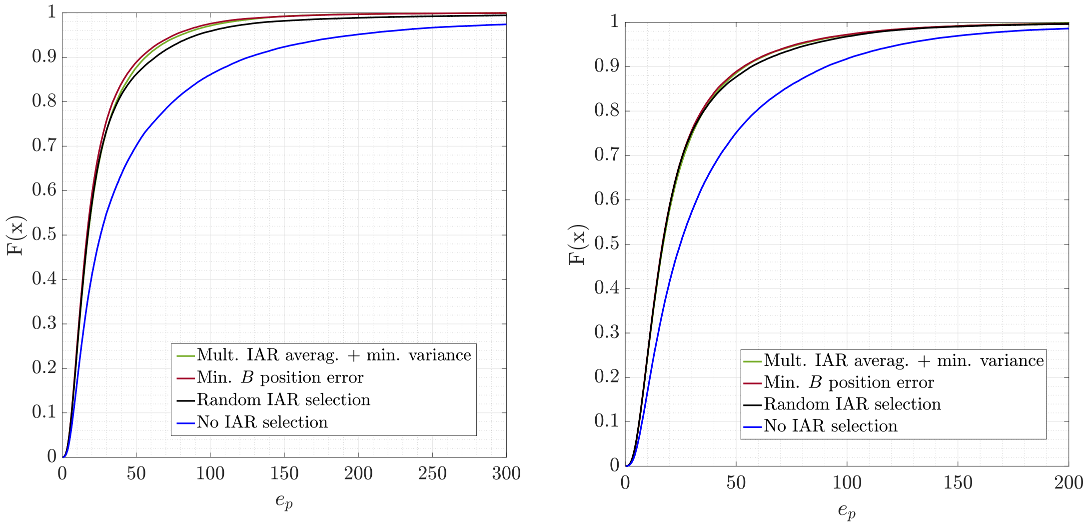

(a) KF AP estimation

(b) EKF QAP estimation

Figure 4.26: Empirical cumulative distribution function of average network position error with filtering based on aiding agent position error. “Random IAR selection” refers to a random selection of IAR to be integrated in the PVT.

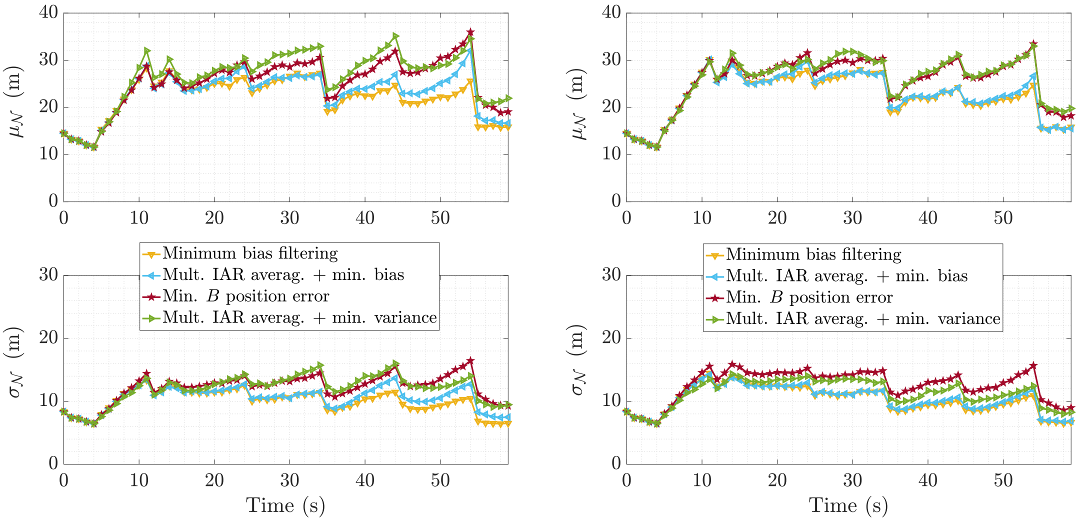

(a) KF AP estimation

(b) EKF QAP estimation

Figure 4.27: Network position error statistic with selective strategies compared. $\mu_{\mathcal{N}}$ and $\sigma_{\mathcal{N}}$ are the network averages of μ_{e_p} and σ_{e_p} respectively.

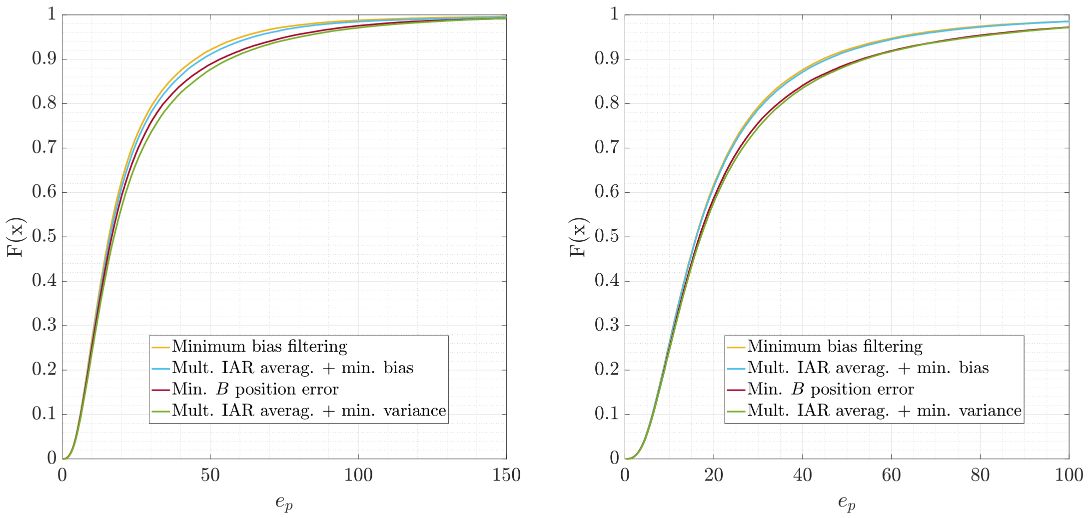

(a) KF AP estimation (b) EKF QAP estimation

Figure 4.28: Empirical cumulative distribution function of average network position error with selective strategies compared.

selective strategy among those discussed in this chapter (Figures 4.27 and 4.28). This method generally provides, w.r.t. a network average, the lowest average position errors μ_{e_p} and also the lowest σ_{e_p}. However, since their performance is very similar, also the same filtering technique combined with multiple IAR averaging will be considered in the next analysis (Sec. 4.4) on joint effects of algorithm's enhancements. In that simulation experiment in fact, the performance obtained from filtering methods may slightly change.

4.4 Final Results: Performance of the Tuned System

As anticipated, the separate efforts made throughout this chapter to improve the IAR algorithm should be observed in a joint experiment, to study their overall effect on e_p. Therefore in this section, the strategies that have been proved to be the most effective are combined in a single simulation experiment and the enhancement of positioning performance is assessed. As a consequence, the empirical CDFs depicted in Figure 4.29 are the results of a selection filter based on a minimum bias criterion, either in combination with multiple IAR averaging or not. Observing the right panel, slightly better performances can be attributed to the EKF QAP estimation version of the IAR algorithm (less than 35 m at 90%). It is known that this algorithm provides generally the best results and this is verified in this context once again.

In both cases, the use of virtual landmarks to preserve the confidentiality among the agents in the network is not advantageous as it was before the tuning of the algorithm (Sec. 4.2.5). However this worsening is not very significant: when confidentiality is granted, the position error increases on average of less than 3 meters in the 90% of cases (Figures 4.29a and 4.29b). In the end, the minimum bias selection strategy is the most successful in presence of any of the two a priori estimation methods, but when confidentiality is demanded, the composite filter that includes aggregation of multiple IAR should be preferred.

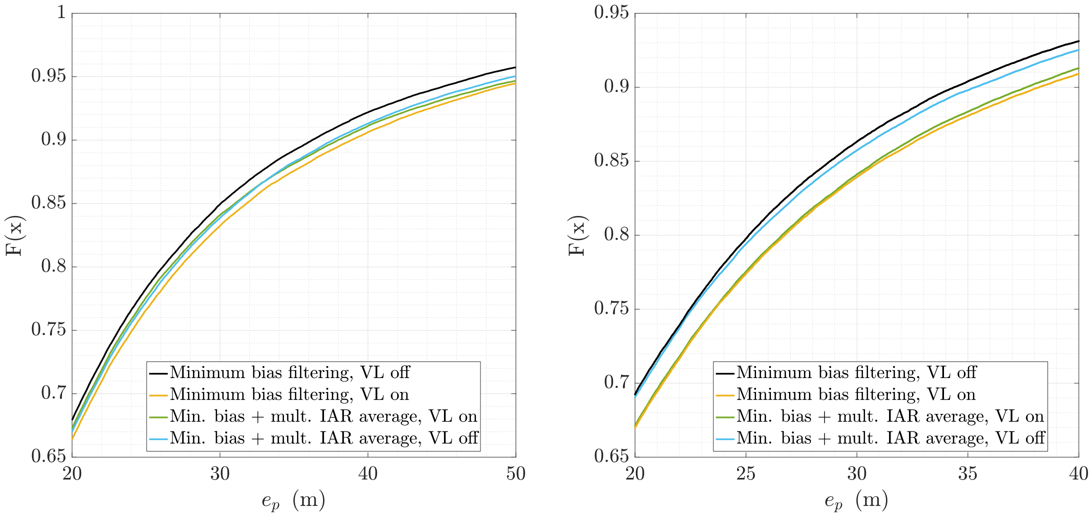

(a) KF AP estimation

(b) EKF QAP estimation

Figure 4.29: Empirical cumulative distribution function of average network position error of tuned algorithm. The CDF are zoomed-in to appreciate the differences. The effects derived form the employment of virtual landmarks are shown. Optimal $\mathbf{W}_{UB}$ and $\mathbf{P}_k$ forcing are applied.

The benefits of algorithm's tuning are illustrated by Figure 4.30, where the enhanced algorithm is tested on the trajectory considered in Section 4.2.1 for a preliminary implementation. With respect to this raw algorithm implementation, huge improvements have been achieved. Using the proposed tuned algorithm, the average position error μ_{e_p} is smaller than in the non-cooperative case, either for the EKF QAP estimation (Figure 4.30b) or the KF AP estimation (Figure 4.30a). Moreover, for this latter case, the resulting standard deviation σ_{e_p} is also lower.

During the outage period the IAR estimation algorithm is able to successfully track even abrupt changes of direction, thanks to the adjustments made on the hybrid PVT routine (Figure 4.31). Moreover, it should be stressed that these adjustments have a general validity and no real-time tuning procedures are required to achieve the results of Figure 4.31. In other words, the configuration of the IAR algorithm resulted from the extensive analysis provided in this chapter is not case-dependent. Thus, this improved algorithm is ready to be implemented on a generic swarm of networked GNSS receivers.

Furthermore, if the proposed collaborative algorithm is compared to a non-cooperative estimation of the same trajectory (Figure 4.32), the latter experiences a more severe drift. Despite the partially-denied GNSS visibility, the IAR method is instead able to limit this drift caused by the lack of positioning data (measurements), proving the effectiveness of

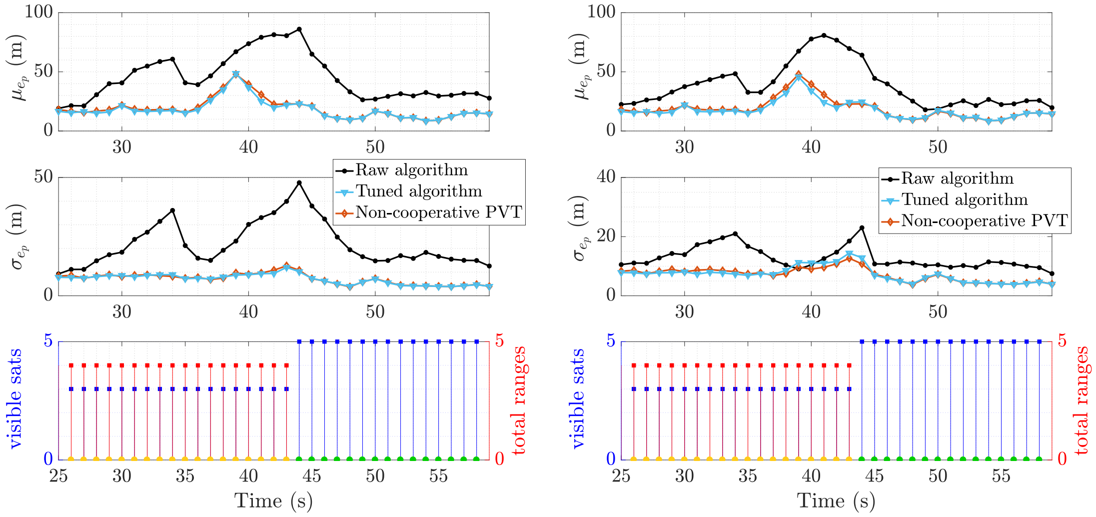

(a) KF a priori estimation

(b) EKF quasi-a-priori estimation

Figure 4.30: Position error statistic of the tuned system. The plots are focused on the outage interval. Optimal $\mathbf{W}_{UB}$ and $\mathbf{P}_k$ forcing are applied. Virtual landmarks are not employed. The minimum bias criterion is imposed on IAR selection and the number of total ranges refers to this method.

the information enhancement carried by the inter-agent range.

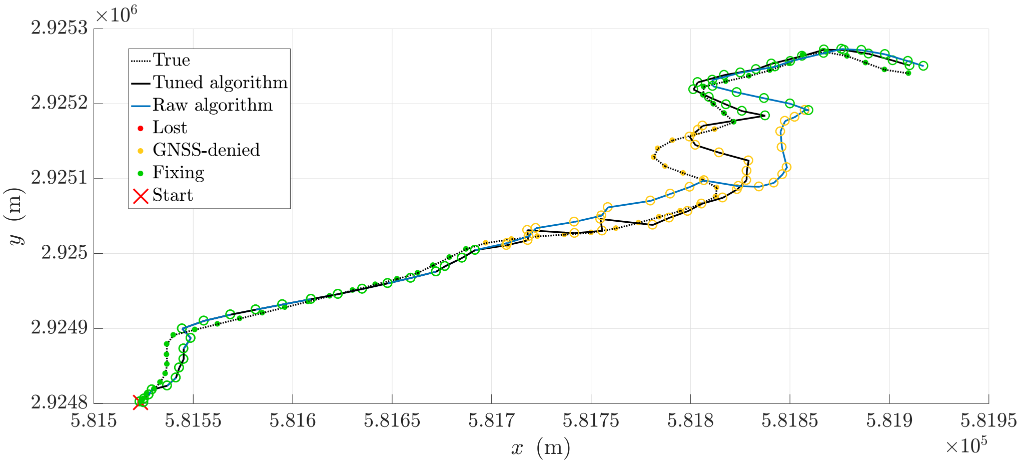

(a) KF a priori estimation

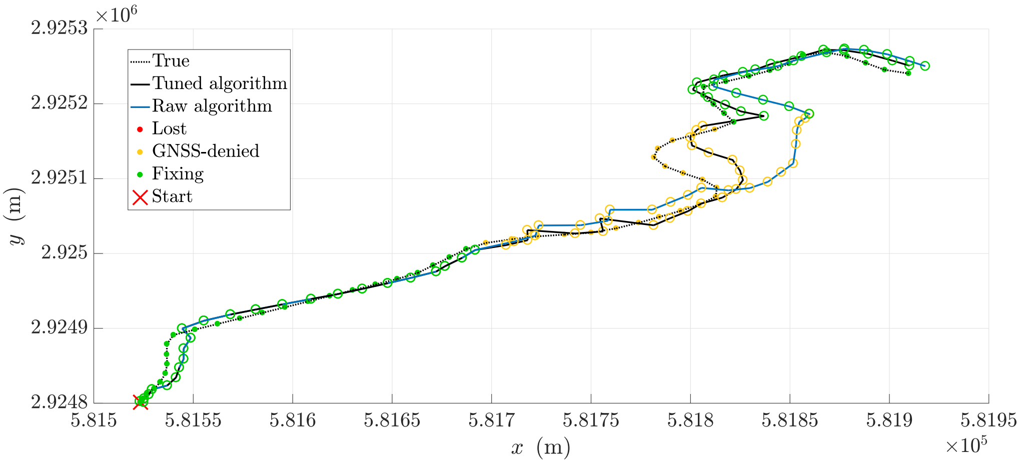

(b) EKF quasi-a-priori estimation

Figure 4.31: Estimated trajectory with tuned IAR positioning algorithm compared to raw algorithm estimation. Optimal $\mathbf{W}_{UB}$ and $\mathbf{P}_k$ forcing are applied. Virtual landmarks are not employed. The minimum bias criterion is imposed on IAR selection.

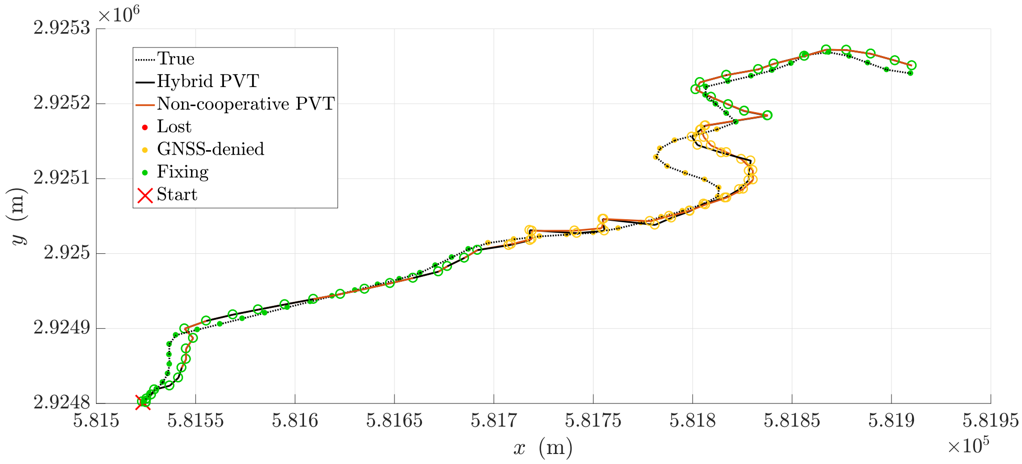

(a) KF a priori estimation

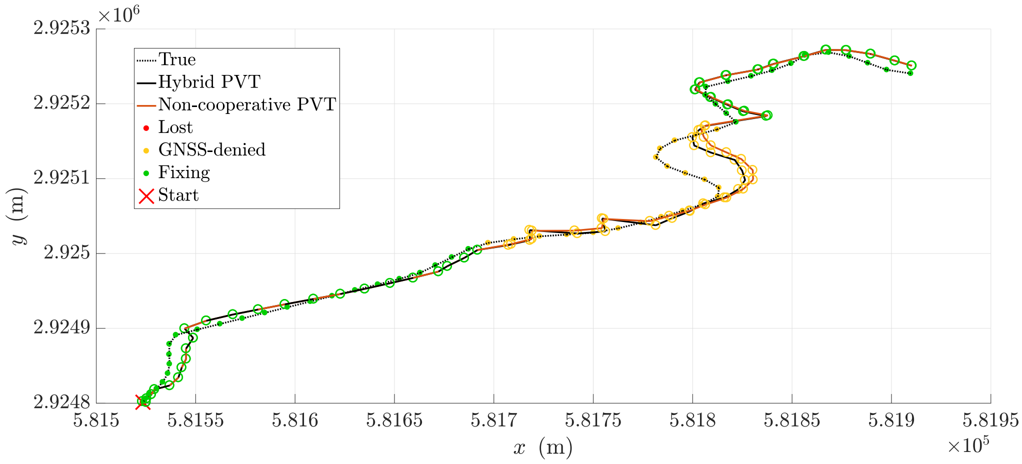

(b) EKF quasi-a-priori estimation

Figure 4.32: Estimated trajectory with tuned IAR positioning algorithm compared to non-cooperative estimation. Optimal $\mathbf{W}_{UB}$ and $\mathbf{P}_k$ forcing are applied. Virtual landmarks are not employed. The minimum bias criterion is imposed on IAR selection.

Chapter 5

Conclusions

In this work, GNSS-users that experience reduced sky visibility conditions are supported by members of a swarm of collaborating agents to improve their location and navigation capabilities. The proposed solution guarantees an improved continuity of localization in condition of poor sky visibility or bad satellites geometry once a proper amount of collaborative information is exchanged among networked agents.

These GNSS positioning units exploit an auxiliary, cooperative, range (IAR) whose estimation and successive integration in the positioning algorithm have been the main targets of this analysis, carried out either focusing on a pair of collaborating agents or by a network perspective.

A measurement model for a GNSS/IAR tightly-coupled integration through an EKF has been designed in order to preserve the optimality of the EKF-based positioning algorithm when cooperative data are involved in the solution. The stability issues relative to the choice of the linearization point has been presented as well as the possibility of a LMS re-initialization of the EKF, possible thanks to the IAR integration, useful to mitigate divergent phenomena.

The IAR estimation procedure has been deeply discussed, inspecting impact factors and estimation issues in a dynamic context, with particular attention to communication delays. It has been shown that a critical point is related to the variables associated to the aided agent, which need to be estimated in a condition of lack of sufficient data. To this purpose two predictive stages has been developed along with correspondent estimation algorithms. After the definition of suitable algorithms, the IAR estimation process has been taken apart in an extensive analysis, where all the impact factors have been isolated and investigated. From the analysis it has been verified that the sole injection of noise in the system is not responsible for instability in the cooperative positioning algorithm. Divergence arises instead with the concurrent presence of feedback between PVT output and IAR estimation, which is unavoidable in the IAR extrapolation scheme and becomes particularly relevant after long time-span of poor GNSS visibility. However, it has been show that even during severe reduction of the GNSS visibility, IAR measurements keep a Gaussian-like distribution, justifying the implementation in a EKF for the positioning.

The effectiveness of the solution adopted for the IAR/GNSS tight integration in the positioning algorithm has been investigated by means of a Monte Carlo simulation. The key aspects of this IAR implementation in a multi-agent environment have been discussed and simulation results have been reported. The simulation environment has been exploited to test the limits and performance of the IAR integration model and to retrieve a statistical characterization of positioning outcomes and IAR estimates thanks to the high number of realizations of the experiments.

In this context several scenarios have been analyzed, investigating different motion dynamics of the receivers, either constrained (urban environment) or random, and different environmental conditions (such as sky visibility and measurement noise) and network constraints (i.e. communication delays). A technique to preserve confidentiality in the network has also been tested and consistent improvements have been observed thanks to numerical errors reduction.

Through experimental results, it has been shown that the proper modeling of system dynamics and measurements integration in the EKF is of primary importance in the context of the IAR paradigm, due to the widespread effects that non-modeled effects have in the hybrid positioning routine. In particular a specific measurement model is fundamental to accomplish an efficient integration of the additional cooperative measurements. To this purpose, some parameters of this model have been configured after an empirical optimization procedure. It has to be remarked that the optimization criteria have been based on aggregated network metrics, hence optimized parameters have general validity and can be adopted in the IAR algorithm.

The importance of a fine IAR measurement model is proportional to the number of additional ranges integrated. Therefore, contextually to a model refinement, a wise selection policy has been imposed on the collaborative range contributions retrieved from the swarm of cooperating agents. Selective strategies and aggregation policies have been therefore widely tested. From these results it has been confirmed that the reduction of IAR contributions mitigates the effects of model sub-optimality, but a valuable selective criterion is necessary to target a significant improvement of the positioning performance.

Despite of the challenging tuning of the proposed navigation algorithm, good benefits have been obtained from this collaborative positioning solution that led to an improved GNSS/IAR tight integration in the positioning algorithm. The enhanced algorithm has been eventually tested and compared to an EKF-based non-cooperative PVT solution: the robustness of the IAR method to GNSS visibility limitations has been verified. Despite the limited sky visibility, the IAR method is able to limit the performance deterioration caused by the lack of positioning data (measurements), proving the effectiveness of the information enhancement carried by the inter-agent range.

A valuable measurement model of the inter-agent range has been proved as an essential feature for the IAR integration algorithm to ultimately obtain a reliable position estimation. With this in mind, a further research could be oriented to a finer definition of the hybrid observation matrix $\bar{\mathbf{H}}$ and the measurement covariance matrix $\bar{\mathbf{R}}_k$. In particular, an adaptive real-time optimization on $\bar{\mathbf{R}}_k$ or the derivation of closed form equations for IAR covariances that overcome the use of upper bounds, would lead to a measurement covariance matrix that will better describe the IAR measurement from a statistical point of view, significantly reducing the EKF sub-optimality.

Bibliography

[1] Antonio Fernandez, Mariano Wis, F Dovis, K Ali, PF Silva, P Friess, I Colomina, E Pares, and Joachim Lindenberger. Gnss/ins/lidar integration in urban environment: Algorithm description and results from atenea test campaign. In *Satellite Navigation Technologies and European Workshop on GNSS Signals and Signal Processing,(NAVITEC), 2012 6th ESA Workshop on*, pages 1–8. IEEE, 2012.

[2] Z. M. Kassas and T. E. Humphreys. Observability analysis of collaborative opportunistic navigation with pseudorange measurements. *IEEE Transactions on Intelligent Transportation Systems*, 15(1):260–273, Feb 2014.

[3] Fabian de Ponte Müller. Survey on ranging sensors and cooperative techniques for relative positioning of vehicles. *Sensors*, 17(2):271, 2017.

[4] Zengke Li, Ren Wang, Jingxiang Gao, and Jian Wang. An approach to improve the positioning performance of gps/ins/uwb integrated system with two-step filter. *Remote Sensing*, 10(1):19, 2017.

[5] Jian Wang, Yang Gao, Zengke Li, Xiaolin Meng, and Craig M Hancock. A tightly-coupled gps/ins/uwb cooperative positioning sensors system supported by v2i communication. *Sensors*, 16(7):944, 2016.

[6] As' ad Salkham, Raymond Cunningham, Anurag Garg, and Vinny Cahill. A collaborative reinforcement learning approach to urban traffic control optimization. In *Proceedings of the 2008 IEEE/WIC/ACM International Conference on Web Intelligence and Intelligent Agent Technology-Volume 02*, pages 560–566. IEEE Computer Society, 2008.

[7] Elliott D Kaplan and Christopher Hegarty. *Understanding GPS/GNSS: Principles and Applications.* Artech House, 2017.

[8] Kai Liu, Hock Beng Lim, Emilio Frazzoli, Houling Ji, and Victor CS Lee. Improving positioning accuracy using gps pseudorange measurements for cooperative vehicular localization. *IEEE Transactions on Vehicular Technology*, 63(6):2544–2556, 2014.

[9] Fabian de Ponte Muller, Estefania Munoz Diaz, Bernhard Kloiber, and Thomas Strang. Bayesian cooperative relative vehicle positioning using pseudorange differences. In *Position, Location and Navigation Symposium-PLANS 2014, 2014 IEEE/ION*, pages 434–444. IEEE, 2014.

[10] D. Yang, F. Zhao, K. Liu, H. B. Lim, E. Frazzoli, and D. Rus. A gps pseudorange based cooperative vehicular distance measurement technique. In *2012 IEEE 75th Vehicular Technology Conference (VTC Spring)*, pages 1–5, May 2012.

[11] Alex Minetto, Calogero Cristodaro, and Fabio Dovis. A collaborative method for positioning based on gnss inter agent range estimation. *2017 25th European Signal*

Processing Conference (EUSIPCO), 2017.

[12] Alex Minetto and Fabio Dovis. A theoretical framework for collaborative estimation of distances among gnss users. *Proceedings of IEEE/ION PLANS 2018*, pages 1492 – 1501, 2018.

[13] Alex Minetto, Calogero Cristodaro, and Fabio Dovis. A collaborative method for gnss-based inter-agent range estimation and hybrid positioning algorithm in harsh environment. *Proceedings of the 30th International Technical Meeting of The Satellite Division of the Institute of Navigation (ION GNSS+ 2017)*, pages 3784–3795, 2017.

[14] Elliott D. Kaplan and Christopher J. Hegarty. *Understanding GPS: principles and applications.* Artech House, 2006.

[15] Joseph L Leva. An alternative closed-form solution to the gps pseudo-range equations. *IEEE Transactions on Aerospace and Electronic Systems*, 32(4):1430–1439, 1996.

[16] Stephen Bancroft. An algebraic solution of the gps equations. *IEEE Transactions on Aerospace and Electronic Systems*, (1):56–59, 1985.

[17] Mr Warren Hundley, Stephen Rowson, and Mr Glenn Courtney. Flight evaluation of a basic c/a code differential gps for category i precision approach. In *International Technical Meeting of the Satellite Division of the Institute of Navigation*, 1992.

[18] Gianluca Falco, Marco Pini, and Gianluca Marucco. Loose and tight gnss/ins integrations: Comparison of performance assessed in real urban scenarios. *Sensors*, 17(2):255, 2017.

[19] R. E. Kalman. A new approach to linear filtering and prediction problems. *Journal of Basic Engineering*, 82(1):35–45, 1960.

[20] Robert Grover Brown and Patrick Y. C. Hwang. *Introduction to random signals and applied Kalman filtering: with MATLAB exercises.* John Wiley & Sons, Inc., 2012.

[21] K. Reif, S. Gunther, E. Yaz, and R. Unbehauen. Relaxation of initial error and noise bounds for stability of gps/ins attitude estimation. *IEEE Transactions on Automatic Control*, 44(4):714–728, 1999.

[22] Matthew Rhudy, Yu Gu, and Marcello Napolitano. Stochastic stability of the discrete-time extended kalman filter. *AIAA Guidance, Navigation, and Control Conference. Minneapolis, Minnesota*, 2012.

[23] ITU-R. Framework and overall objectives of the future development of imt for 2020 and beyond. Technical report, International Telecommunication Union, Febrauary 2015.

[24] M. Agiwal, A. Roy, and N. Saxena. Next generation 5g wireless networks: A comprehensive survey. *IEEE Communications Surveys Tutorials*, 18(3):1617–1655, thirdquarter 2016.

[25] Mark Petovello. Differences between least squares and kalman filtering gnss filtering options. *Inside GNSS*, 2013.

[26] Daniel Krajzewicz, Jakob Erdmann, Michael Behrisch, and Laura Bieker. Recent development and applications of sumo-simulation of urban mobility. *International Journal On Advances in Systems and Measurements*, 5(3&4), 2012.

[27] Lina He, Hairui Zhou, and Gongyuan Zhang. Improving extended kalman filter algorithm in satellite autonomous navigation. *Proceedings of the Institution of Mechanical Engineers, Part G: Journal of Aerospace Engineering*, 231(4):743–759, 2017.

[28] Arthur Gelb. *Applied optimal estimation.* MIT press, 1974.